SURFACE NANOPATTERNING OF FUNCTIONAL POLYMERS BY PARALLEL SCANNING PROBE LITHOGRAPHY

XIE Zhuang
Ph.D

The Hong Kong Polytechnic University
2015

The Hong Kong Polytechnic University

Institute of Textiles and Clothing

Surface Nanopatterning of Functional Polymers by Parallel Scanning Probe Lithography

XIE Zhuang

A Thesis Submitted in Partial Fulfillment of the
Requirements for the Degree of Doctor of Philosophy

August 2014

Certificate Of Originality

I hereby declare that this thesis is my own work and that, to the best of my knowledge and belief, it reproduces no material previously published or written, nor material that has been accepted for the award of any other degree or diploma, except where due acknowledgement has been made in the text.

(Signed)

Zhuang Xie

August 2014

To My Parents for Their Endless Support

ABSTRACT

Engineering surface with patterned functional polymers is a crucial issue in a wide range of research fields. The recently developed parallel scanning probe arrays have emerged as promising candidates for desktop nanofabrication with high resolution and high throughput. Yet, there are only a few literature reports on the large-area patterning of functional polymer nanostructures via parallel SPL, with lack of fundamental understandings and practical applications. Moreover, it still remains some inherent limitations in current parallel SPL techniques regarding the resolution, uniformity and versatility. This thesis describes several approaches to tackle the challenges in the two aspects. The statement of challenges and objectives of this research is presented in the beginning, followed by a comprehensive literature review on nanopatterning techniques and a general introduction of methodologies. Next, Chapter 4 introduces the studies on ink transport in direct writing of polymers and applications of liquid polymer matrix. Chapter 5 states a molecular printing approach towards high-throughput fabrication of 3D polymer brushes. Chapter 6 describes the development of an apertureless polymer pen array to deliver both optical energy and materials. Chapter 7 addresses the uniformity challenge in polymer pen lithography through engineering the tip structure and new materials. Finally, Chapter 8 provides conclusions and future outlooks.

First, direct printing of polymer ink materials was studied by dip-pen nanolithography (DPN) and polymer pen lithography (PPL). Two typical polymer inks were investigated, including polyelectrolytes and hygroscopic polymers. For polyelectrolytes, the ink transport was found to be tuned from molecular diffusion to liquid deposition mechanism by adding additives or using polymer pens. Moreover, a catalytic printing was developed for generating metal structures on flexible substrates by employing the hygroscopic polymer ink as delivery matrix and surface-grafted polymer as receiving matrix for catalysts.

Second, by combining PPL with surface-initiated polymerization, for the first time we demonstrated the high-throughput generation of 2D and 3D complex polymer brush nanostructures over square-centimeter areas. The control on the 3D structures of polymer brush patterns was achieved by rational design of PPL parameters. Furthermore, the large-area patterned polymer brushes were explored as etching resists for micro/nanofabrication, as well as robust and versatile platforms for bioimmobilization.

In addition to material printing, an apertureless polymer pen array was developed to enable serial writing with light at the sub-wavelength scale. This was achieved by combining the self-light-focusing polymer pyramids with an opaque coating on the flat backing regions. The elastomeric pens also show the capability of force-tuned illumination and simultaneous delivery of materials and optical energy.

Furthermore, a novel dual-elastomer tip array was designed and fabricated to improve the resolution and the large-area uniformity in PPL. The ultrasharp tip with hard-apex, soft-base layered structure was verified to reduce tip deformation upon contact with the substrate by both experimental and mechanical simulation results, leading to decreased feature size and minimized size variation over large areas.

In conclusions, large-area, high-throughput nanopatterning of functional polymers by parallel SPL is achieved through approaches of direct printing, surface-initiated growth and photochemical modification. Meanwhile, the development of apertureless cantilever-free pen array and dual-elastomer tip array will extend the patterning capability of SPL and lower the barrier for desktop nanofabrication. Given the broad applications of functional polymers and lithographic techniques, the work presented here is expected to have great impact on physical, chemical, material, biological and engineering fields.

LIST OF PUBLICATIONS

Related Journal Publications

1. Yu Zhou,† **Zhuang Xie**,† Keith A. Brown, Daniel J. Park, Xiaozhu Zhou, Pengcheng Chen, Michael Hirtz, Qing-Yuan Lin, Vinayak P. Dravid, George C. Schatz, Zijian Zheng and Chad A. Mirkin, "Apertureless Cantilever-free Pen Arrays for Scanning Photochemical Printing", *Small*, accepted. († equal contribution)
2. **Zhuang Xie**, Chaojian Chen, Xuechang Zhou, Tingting Gao, Danqing Liu, Qian Miao, Zijian Zheng, "Massively Parallel Patterning of Complex 2D and 3D Functional Polymer Brushes by Polymer Pen Lithography", *ACS Appl. Mater. Interfaces* **2014**, *6*, 11955-11964.
3. **Zhuang Xie**,† Youde Shen,† Xuechang Zhou,† Yong Yang, Qing Tang, Qian Miao, Jing Su, Hongkai Wu, and Zijian Zheng, "Polymer Pen Lithography Using Dual-Elastomer Tip Arrays", *Small* **2012,** *8*, 2664-2669. († equal contribution)
4. **Zhuang Xie**, Xuechang Zhou, Xiaoming Tao, Zijian Zheng, "Polymer Nanostructures Made by Scanning Probe Lithography: Recent Progress in Material Applications", *Macromol. Rapid Commun.* **2012**, *33*, 359-373.
5. Ruisheng Guo, You Yu, **Zhuang Xie**, Xuqing Liu, Xuechang Zhou, Yufan Gao, Zhilu Liu, Feng Zhou, Yong Yang, and Zijian Zheng, "Matrix-Assisted Catalytic Printing for the Fabrication of Multi-Scale, Flexible, Foldable, and Stretchable Metal Conductors", *Adv. Mater.***2013,** *25*, 3343–3350.

Other Journal Publications

List of Publications

1. Chaojian Chen, Xuechang Zhou, **Zhuang Xie**, Tingting Gao, and Zijian Zheng, “Construction of Three-Dimensional Polymer Brushes by Dip-Pen Nanodisplacement Lithography: Understanding Molecular Nanodisplacement for High-Speed Patterning”, *Small,* accepted.

2. Xiaolong Wang, Casey Yan, Hong Hu, Xuechang Zhou, Ruisheng Guo, Xuqing Liu, **Zhuang Xie**, Zhifeng Huang and Zijian Zheng, “Aqueous and Air-Compatible Fabrication of High-Performance Conductive Textiles”, *Chem. Asian J.* **2014**, *9*, 2170-2177

3. You Yu, Jifang Zeng, Chaojian Chen, **Zhuang Xie**, Ruisheng Guo, Zhilu Liu, Xuechang Zhou, Yong Yang and Zijian Zheng, “Three-dimensional Compressible and Stretchable Conductive Composites”, *Adv. Mater*. **2014**, *26*, 810-815.

4. Liyong Niu, Mingjian Li, Xiaoming Tao, **Zhuang Xie**, Xuechang Zhou, Arun P. A. Raju, Robert J. Young, and Zijian Zheng, “Salt-assisted Direct Exfoliation of Graphite Into High-quality, Large-size, Few-layer Graphene Sheets”, *Nanoscale* **2013**, *5*, 7202-7208.

5. Tiansheng Gan, Xuechang Zhou, Chunfeng Ma, Xuqing Liu, **Zhuang Xie**, Guangzhao Zhang, and Zijian Zheng, “Liquid-Mediated Three-Dimensional Scanning Probe Nanosculpting”, *Small*, **2013**, *9*, 2851–2856.

6. Xinlei Ma, **Zhuang Xie**, Zhilu Liu, Xuqing Liu, Tingbing Cao and Zijian Zheng, “Polymer Brush Electrets”, *Adv. Funct. Mater.* **2013,** *23*, 3239-3246.

7. Xuechang Zhou, Zhilu Liu, **Zhuang Xie**, Xuqing Liu and Zijian Zheng, “High-Resolution, Large-Area, Serial Fabrication of 3D Polymer Brush Structures by Parallel Dip-Pen Nanodisplacement Lithography”, *Small* **2012,** *8,* 3568-3572.

8. Xuechang Zhou, Xuqing Liu, **Zhuang Xie**, Zijian Zheng, “3D-patterned Polymer Brush Surfaces”, *Nanoscale* **2011**, *3*, 4929-4939.

List of Publications

9. Xuechang Zhou, Xiaolong Wang, Youde Shen, **Zhuang Xie**, Zijian Zheng, "Fabrication of Arbitrary Three-Dimensional Polymer Structures by Rational Control of the Spacing between Nanobrushes", *Angew. Chem. Int. Ed.* **2011,** *50*, 6506-6510.

Patents

1. Z. J. Zheng, Y. D. Shen, X. C. Zhou, **Z. Xie** "Composite Tip Array for Polymer Pen Lithography" US Patent, Application No. 13/467,552
2. C. A. Mirkin, Y. Zhou, Z. J. Zheng, **Z. Xie**, K. A. Brown, "Apertureless Cantilever-Free Pen Arrays for Scanning Optical Lithography and Photochemical Printing" US Patent, submitted.

Conference Presentations

1. **Zhuang Xie**, Chaojian Chen, Xuechang Zhou, Tingting Gao, Zijian Zheng, "Massively Parallel Patterning of Complex Polymer Brush Nanostructures by Polymer Pen Lithography (PPL)", ***2014 Materials Research Society Spring Meeting and Exhibit***, 21-25 April, 2014, San Francisco, California, USA.
2. **Zhuang Xie**, Zijian Zheng, "Patterning Surface by Polymer Pen Lithography (PPL)", ***The 68th IUVSTA Workshop "Multifunctional Surface Engineering for Advanced Energy Applications"*** 9-13 December, 2012. City University of Hong Kong, Hong Kong SAR.
3. **Zhuang Xie**, Xuechang Zhou, Zijian Zheng, "Large-Area, Arbitrary Patterned Polymer Structures Fabricated by Polymer Pen Lithography", ***2012 Mainland, Taiwan and Hong Kong Symposium on Liquid Crystalline Polymers and Ordered Supermolecular Structures,*** 26-29 August, 2012, Xiangtan University, Xiangtan, Hunan, China.

List of Publications

4. **Zhuang Xie,** Xuechang Zhou, Zijian Zheng, "Study of Conjugated Polymer Nanostructures Obtained by Dip-Pen Nanolithography", ***Fiber Society 2011 Spring Conference***, 22-25 May, 2011, The Hong Kong Polytechnic University, Hong Kong SAR.

ACKNOWLEDGEMENTS

First of all, I would like to express my most sincere thanks to my chief supervisor, Prof. Zijian Zheng for bring me into the fascinating Nano world and guiding me to explore the cutting-edge research. His 4-years guidance, professional training, insightful suggestions, and encouragements, have led me to complete this fruitful research and become a qualified PhD. I learned much from him including developing the scientific insight, scrupulously proving the hypothesis, and expressing opinions. His high-quality requirements in academic research have always been great inspirations for me.

I would also like to express my gratitude to my co-supervisors, Prof. Xiaoming Tao, who provides me enormous support for my research project. Besides, her guidance in critical thinking and encouraging feedback brought great help to me.

I am very grateful to my colleagues in Prof. Zheng’s group who accompany me throughout my PhD study, special thanks to Dr. Xuechang Zhou, Dr. Xinlei Ma, Dr. Xiaolong Wang, Dr. Zhilu Liu, Dr. You Yu, Dr. Ruisheng Guo, Dr. Tingting Gao, Youde Shen, Xuqing Liu, Liyong Niu, Chaojian Chen and Lina Chen. I would also like to thank all my colleagues for their precious friendship.

I would like to express my sincere thanks to Prof. Chad A. Mirkin in Department of Chemistry, Northwestern University to allow me to work in the world-class lab as a visiting student. I must thank my collaborators, Dr. Xing Liao, Dr. Keith A. Brown, Dr. Xiaozhu Zhou, Yu Zhou, Pengcheng Chen, Shu He, Daniel Park for their kind help and discussions.

I also gratefully acknowledge financial support from The Hong Kong Polytechnic University (A-PK21), the General Research Fund of Hong Kong (Project PolyU5041/11P), National Natural Science Foundation of China (Project 51273167) and Research Student Attachment Programme of HKPolyU.

Finally I wish to express my deepest gratitude to my dear parents for their endless love and support.

TABLE OF CONTENTS

ABSTRACT……………………………………………………………………..I
LIST OF PUBLICATIONS……………………………………………..III
ACKNOWLEDGMENTS……………………………………………......VII
TABLE OF CONTENTS…………………………………………….…...VIII
LIST OF TABLES AND FIGURES…………………………………...XII
LIST OF ABBREVIATIONS…………………………………….......XX

CHAPTER 1 INTRODUCTION 1
1.1 Background and Challenges.. 1
1.2 Research Objectives 3
1.3 Research Originality.. 3
1.4 Outlines of the Thesis.. 4
CHAPTER 2 LITERATURE REVIEW 6
2.1 Nanopatterning Techniques for Functional Polymers 6
2.1.1 Conventional Lithography 8
2.1.2 Unconventional Nanofabrication 10
2.2 Patterning Functional Polymers by Scanning Probe Lithography 16
2.2.1 Dip-Pen Nanolithography 17
2.2.2 Template-Assisted Patterning.. 24
2.2.3 Energy-Based Modification 26
2.2.4 Parallel Scanning Probe Arrays for SPL 31
2.3 Conclusions and Summary of Research Gaps 35
CHAPTER 3 METHODOLOGY 37
3.1 Materials.. 37
3.1.1 Writing pens 37
3.1.2 Substrates 39
3.1.3 Chemicals.. 39
3.2 Surface Modification of Substrates... 41

Table of Contents

3.3 Fabrication of Polymer Pen Arrays 43

3.4 Lithography Process 45

3.4.1 DPN 46

3.4.2 PPL 47

3.4.3 BPL 50

3.5 Characterization 51

3.5.1 Atomic Force Microscopy (AFM) 51

3.5.2 Field Emission Scanning Electron Microscopy (FESEM)........... 52

3.5.3 Optical Microscopy 53

3.5.4 Attentuated Total Reflectance Fourier Transform Infrared Spectroscopy (ATR-FTIR) 53

CHAPTER 4 DIRECT PRINTING OF POLYMER MATERIALS 55

4.1 Introduction 55

4.2 DPN and PPL of Cationic Polythiophene PNT 56

4.2.1 DPN of PNT on Various Substrates 56

4.2.2 DPN of PNT Assisted with Additives 60

4.2.3 PPL of PNT 64

4.2.3 Summary 67

4.3 DPN of Liquid Matrix for Matrix-Assisted Catalytic Printing 67

4.3.1 Experimental 68

4.3.2 Results and Discussions 69

4.3.3 Summary 72

4.4. Conclusions and Future Outlooks 73

CHAPTER 5 PATTERNING MOLECULAR TEMPLATES FOR FABRICATION OF 3D POLYMER BRUSHES 74

5.1 Introduction 74

5.2 Experimental 76

5.2.1 Materials 76

5.2.2 Polymer Pen Lithography (PPL) 77

5.2.3 SI-ATRP of PGMA Brushes 77

Table of Contents

5.2.4 Au Etching and PDMS Stamp Fabrication....78

5.2.5 Immobilization of Biomolecules on Brush Patterns 78

5.2.6 Characterization 79

5.3 Results and Discussions 79

5.3.1 Patterning of 2D and 3D Polymer Brush Arrays....79

5.3.2. PGMA Brushes as Resist for Micro/nanofabrication....86

5.3.3. PGMA Brush Templates for Biomolecular Immobilization 89

5.4. Conclusions and Future Outlooks 95

CHAPTER 6 SCANNING OPTICAL LITHOGRAPHY BY APERTURELESS POLYMER PEN ARRAYS 96

6.1. Introduction....96

6.2. Experimental 98

6.2.1. Fabrication of Apertureless Pen Arrays....98

6.2.2. Lithography Procedure....98

6.2.3. Photochemical Printing 99

6.2.4. Simulations....100

6.3. Results and Discussions 100

6.3.1. Principle and Preparation of Apertureless Pen Arrays 100

6.3.2. Scanning Optical Lithography on Photoresist 102

6.3.3. Generation of Gradient Au patterns 108

6.3.4. Photochemical Printing by Apertureless Pen Array.... 111

6.4. Conclusions and Future Outlooks 112

CHAPTER 7 DEVELOPMENT OF DUAL-ELASTOMER TIP ARRAY FOR SCANNING PROBE LITHOGRAPHY 114

7.1. Introduction.... 114

7.2. Experimental 116

7.2.1 Pretreatment of Glass Substrate 116

7.2.2 Fabrication of Dual-Elastomer Tip Arrays.... 117

7.2.3 Polymer Pen Lithography (PPL).... 117

7.2.4 Finite-Element (FE) Simulations 118

Table of Contents

7.3. Results and Discussions 119

7.3.1 Preparation and Characterization of Dual-Elastomer Tip Arrays 119

7.3.2 Printing Small Molecules by Dual-Elastomer Tip Arrays........... 121

7.3.3 Printing Polymer Ink by Dual-Elastomer Tip Arrays.................. 123

7.3.4 Mechanical Simulations on Dual-Elastomer Tip Structure......... 126

7.3.5 Comparison with Other Tip Structures 129

7.4. Conclusions and Future Outlooks 130

CHAPTER 8 CONCLUSIONS AND SUGGESTIONS FOR FUTURE WORK... 131

8.1. Conclusions 131

8.2. Suggestions for Future Work... 133

REFERENCES 135

LIST OF TABLES AND FIGURES

Table 2.1. Current capabilities of conventional and unconventional nanopatterning techniques.

Table 3.1. Parameters of the1-D cantilever arrays.

Figure 1.1. Research framework and thesis outline.

Figure 2.1. (A) Photolithography for fabricating Si chips and the image of the as-made chips on a 12″ wafer. (Courtesy: Intel Corporation) (B) Patterning polymer brush resist by EBL. An AFM image shows the fabricated patterns with 50-nm feature size and 100-nm pitch.

Figure 2.2. Nanoimprint lithography. (A) Schematic of NIL process. (B) Large-area grating patterns on glass produced by roll-to-roll NIL. (C) Chain alignment of conjugated polymers induced by NIL.

Figure 2.3. Contact printing. (A) Schematic of microcontact printing (μCP). (B) Hard stamp with 70 nm line/space patterns for nanocontact printing (left) and the resulted polystyrene nanobeads (～96 nm) deposited on printed polyelectrolytes patterns (right). (C) Chemically patterned flat stamp for printing sub-100 nm features.

Figure 2.4. Moulding by capillary force. (A) MIMIC in nanochannels to fabricate 50-nm line patterns. (B) Fabrication of organic electronic device by LCW. (C) Procedures for LB-nTM.

Figure 2.5. Block copolymer self-assembly. (A) Schematic of nanopatterning by self-assembly of block copolymers. (B) Scanning electron microscope (SEM) image of the as-made 15-nm PEDOT:PSS nanowire arrays from block copolymer templates and their gas sensing property to ethanol.

Figure 2.6. Dip-pen Nanolithography (DPN). (A) Schematic of meniscus-mediated transport of molecular and liquid ink by DPN. (Courtesy: Nanoink, Inc.) (B) Memory device fabricated by DPN-deposited ferroelectric polymer nanostructures.[92]

Figure 2.7. PEG resists fabricated by DPN for multifunctional applications. (A) Schematic illustration of the fabrication and application of the PEG resists. (B) AFM topography image of the patterned PEG features. (C) Optical and SEM images of the fabricated photomask from PEG resists. (D) Optical microscope image of DPN-generated PEG arrays on PDMS and SEM image of Au dot arrays obtained from microcontact printing with the chemically patterned flat PDMS stamp. (E) Optical microscope image of an array of photoresist patterns fabricated with PEG phase-shift lenses and an AFM image shows the letter “N”

consisting of well-shaped features.

Figure 2.8. Polymer carrier matrixes for DPN. (A) Schematic illustration of matrix-assisted DPN. (B) DPN patterning of C_{60} assisted by PEG matrix and the demonstration of phototransistor fabrication. (C) Fluorescent images of patterns of two proteins generated with the aid of agarose matrix, showing similar feature sizes. (D) Scanning probe block copolymer lithography using PEO-*b*-P2VP micelles loaded with $HAuCl_4$ as inks. An SEM image shows the nanoparticle formed within the patterned polymer matrix. (E) SEM image of an array of Au nanoparticles; the insert shows a high-resolution TEM image of a sub-10-nm single-crystalline Au nanoparticle.

Figure 2.9. Thermal DPN. (A) Schematic of deposition of thermoplastic polymer encapsulating nanoparticles from a heated probe and AFM images of the as-made polymer nanowire and nanoparticle line after plasma treatment. (B) Controlled deposition of conjugated polymer PDDT. (C) Aligned domains of molten block copolymers deposited from scanning probe.

Figure 2.10. 3D polymer brushes grown from patterned initiators. (A) Schematic of dip-pen nanodisplacement lithography (DNL) for controlling the height of polymer brushes. (B&C) Lateral force microscope image of the patterned initiator footprints by DNL (B) and AFM image of the as-grown polymer brushes (C). (D) AFM image of polymer brushes with controlled height by varying feature distance. (E) Fabrication of arbitrary 3D patterned by feature-density method.

Figure 2.11. Scanning near-field optical lithography (SNOL). (A) Schematic of SNOL and the optical intensity distribution on the surface. (B) AFM image of PPV patterns fabricated by SNOL. (C) Nanoscale protein patterns through SNOL-induced photodegradation of OEG layer.

Figure 2.12. Patterning by mechanical force. (A) Schematic of organic transistor with channel defined by scratching of PEDOT:PSS electrodes. (B) AFM image of the scratched PEDOT:PSS electrode pair. (C) Disordered regions in the lamellar domains of the baroplastic block copolymer created by applying force. (D) Writing and local erasing of nanoscale features at room temperature on the baroplastic block copolymer thin film.

Figure 2.13. Thermochemical nanolithography. (A) Probe-based nanolithography on self-amplified depolymerization (SAD) polymer resist. (B) Thermochemical nanopatterning on an organic semiconductor precusor. Fluorescence microscope image of the patterned PPV nanowires is shown.

Figure 2.14. Parallel patterning by cantilever array. (A) 2D cantilever array for massively parallel DPN patterning. (B) Optical microscope image of photonic structures consisting of lipid nanopatterns by 1D-array DPN. (C) Parallel thermochemical nanopatterning using an array of five thermal cantilevers and corresponding five fluorescence images of PPV Mona Lisa patterns obtained

with the array.

Figure 2.15. Cantilever-free scanning probe arrays. (A) Timeline of development of cantilever-free SPL techniques. (B) Image of polymer pen array over 3-inch wafer areas. (C) Fluorescence image of protein arrays patterned by PPL, with feature size showing time and force dependence. (D) Multiscaled electrode array fabricated by tuning contact force. (E) SEM image of hard Si tip arrays on soft elastomeric support. (F) SEM image of Au patterns composed of sub-50-nm features. Scale bar: 270 nm. (G) Patterned polymer arrays by thermal DPN from graphene-coated Si tip.

Figure 2.16. Beam pen lithography (BPL). (A) Schematic of BPL principle. (B) SEM image of the BPL pen array with 100-nm aperture. (C) Large-area complex nanostructures generated by active BPL.

Figure 3.1. Schematic illustrations of parallel dip-pen nanolithography (DPN) (A), polymer pen lithography (PPL) (B) and apertureless beam pen lithography (BPL) (C).

Figure 3.2. 1-D cantilever arrays used for DPN. (A) E-type with square-shaped cantilevers and 18 tips; (B) M-type with triangle-shaped cantilevers and 12 tips. (C) Schematics of printing of molecular ink (left) and liquid ink (right). (Copyright: Nanoink, Inc.)

Figure 3.3. 2-D polymer pen arrays for PPL and BPL.

Figure 3.4. Chemical structures of the materials used in the experiments.

Figure 3.5. Formation of thiol and silane SAMs on the substrates.

Figure 3.6. Schematic of the major fabrication steps for polymer pen arrays.

Figure 3.7. (A) Digital photograph of a Si master and the magnified optical image of the fabricated microwells in the Si master. (B) Optical microscope image of the replicated polymer pen arrays and SEM image of a single polymer tip.

Figure 3.8. Park XE-100 AFM encased in a humidity-controlled glove box.

Figure 3.9. Optical images of the inked 18-cantilever tip array before (A) and after (B-C) contacting with the MHA-coated Au substrate, where the 18 tips are partially aligned (B) or fully-aligned (C) as confirmed by monitoring the differences of optical reflections of the cantilevers.

Figure 3.10. PPL process. (A) Polymer pen arrays mounted on AFM scanning head. (B) Z scanner attached to the AFM and aligned to substrate. (C) Schematic of optical leveling of the polymer pen array to a substrate. (D) Optical microscope image of large-area Au dot arrays after PPL patterning of MHA and Au etching; and (E) the magnified images of Au dot arrays.

Figure 3.11. Block diagram of the BPL apparatus and the operational cycle.

List of Tables and Figures

Figure 3.12. (A) Principle of AFM. (B) Van der Waals force as a function of tip-sample distance.

Figure 4.1. (A) Chemical structure of PNT. (B) Lateral force microscope (LFM) image of PNT nanolines written on Au, with writing speed of 0.01, 0.02, 0.04, 0.06 μm/s from left to right. (C) LFM image of PNT nanodot array on Au with dwell time from 49 s to 300 s. (D) Plot of dot diameter with square root of dwell time ($t^{1/2}$) with linear fitting.

Figure 4.2. (A&B) LFM images of PNT nanolines written by E-type tip array on SiO_2(A) and HMDS-SiO_2(B). (C&D) Tapping-mode AFM images of PNT nanolines (C) and nanodots (D) written by M-type tip array on HMDS-SiO_2.

Figure 4.3. (A) Fluorescence microscope images of dot arrays by DPN patterning of PNT/glycerol (1:5 w/w). (B) Tapping-mode AFM topography image of the array shown in (A). (C) Fluorescence microscope images of parallel dot arrays generated from PNT/glycerol (5:1 w/w) ink. (D) Intensity count of dots with varied dwell time, as indicated in (C). (E) Tapping-mode AFM topography image of one array shown in (C).

Figure 4.4. (A) Fluorescence microscope images of dot arrays by DPN patterning of PNT/PEG2000 (10:1 w/w). (B) Magnified fluorescence image of one array shown in (A). (C) Tapping-mode AFM topography image of the array shown in (B).

Figure 4.5. (A) Dark-field and (B) fluorescence microscope images of PNT dot arrays patterned by PPL. (C&D) Tapping-mode AFM images of dot array printed by one tip with varied dwell time (C) and contact force (D). (E&F) Plots of height, feature size and dot volume versus dwell time (E) and z-piezo extension (F). (G) Magnified tapping-mode AFM topography and phase images of one array, showing dot with feature size of 140 nm and halos around the dots in the phase image.

Figure 4.6. Schematic illustration of matrix-assisted catalytic scanning probe printing.

Figure 4.7. (A) Optical microscope image of the printed polymer matrixes with catalysts on the PMETAC-grafted PET by DPN. (B) Corresponding Cu patterns obtained after ELD.

Figure 4.8. (A) SEM image of Cu dot arrays produced by varying dwell time in printing of catalytic ink. The dwell time is 1, 4, 16 s for the arrays from left to right. A linear function is also shown between the feature size and square root of dwell time. (B) Optical microscope image of Cu dot arrays with size of 1-2 μm. (C) SEM image of one Cu dot array with average feature size of 1.67±0.33 μm. (D) Optical and SEM images of submicrometer Cu dot array.

List of Tables and Figures

Figure 5.1. Schematic illustration of the large-area, arbitrary patterning of PGMA brushes through a combination of PPL and SI-ATRP.

Figure 5.2. (A) Designed patterning parameters for brush arrays in PPL. In the bottom left array, the dwell time (*t*) ranges from 0.1 s to 9 s from bottom to top, and the z-piezo extension (*z*) is set as 0.5 μm; in the bottom right array, *z* increases from 0 to 3 μm from bottom to top (t=0.25 s); in the top array, the feature distance (*d*) varies from 250 to 2500 nm from left to right, with t=0.25 s and z=0.5 μm. (B) Optical microscope image of the patterned PGMA brush arrays over large areas. (C) Image of brush patterns over the whole 6.6 by 4.1 mm^2 area. The figure is obtained by blending 9 optical microscope images using Photoshop. Inset shows a magnified optical microscope image of the pattern arrays.

Figure 5.3. (A) A polymer pen array with ~2×1 cm^2 patterning area and the corresponding 2-cm^2 PGMA brush arrays on Au substrate. (B) ATR-FITR spectra of the patterned PGMA brush arrays.

Figure 5.4. (A) AFM topography of a typical PGMA brush array made with various z-piezo extensions. (B) Plot of the feature size versus z-piezo extension. (C) AFM topography of PGMA brush array made with various dwell times. (D) Plot of the feature size and brush height versus $t^{1/2}$. (E) AFM topography of PGMA brush array made with various feature distances. (F) Statistical results of the brush height at different feature distance, obtained from 4 different arrays.

Figure 5.5. (A) Optical microscope images of the large-area patterned 3D structures of PGMA brushes. The inset shows a magnified polarized optical image of the 3D patterns. (B) The bitmap density maps used to fabricate the 3D structures and the corresponding 3D AFM topography image of the patterned PGMA brushes. (C) Cross-sectional analysis of the topographic profiles of 3D PGMA patterns. The selected cross sectional positions are shown as red lines in the inset of A.

Figure 5.6. PGMA brushes as resists for micro/nanofabrication. (A) Scheme of the fabrication of Au arrays and PDMS stamp. (B) Optical microscope images of the PPL-patterned PGMA brushes, and (C) the resulted Au arrays after etching. (D) SEM image of a typical array of Au patterns shown in C. (E) Optical microscope image of a PDMS stamp fabricated from patterns shown in C as the mold. The inset shows the digital image of the 1×1 cm^2 PDMS stamp. (F, G) AFM topography images of the concave pattern arrays on the PDMS stamp. The profile shows the depth varying from 35 to 70 nm.

Figure 5.7. AFM topography and lateral force images of PGMA brush pattern backfilled with EG_3 SAM.

Figure 5.8. PGMA brushes for DNA immobilization. (A) Scheme of DNA binding and hybridization on PPL-patterned PGMA brushes. (B) Optical microscope image of PGMA brush pattern arrays. (C-D) Fluorescent

microscope images of the patterned PGMA brushes bound with 5’-NH_2, 3’-TET-modified ssDNA (C), and after hybridization with 5’-TAMRA-labeled complementary probes (D). λ_{ex} = 465–495 nm, λ_{obs} = 515–555 nm for green fluorescence and λ_{ex} = 528–553 nm, λ_{obs} = 577-632 nm for orange fluorescence. The scale bars in the insets are 20 µm. (E) AFM topography of the patterned PGMA brushes. (F) Statistical results of fluorescence intensity counts for TET-ssDNA and dsDNA with different brush height, obtained from randomly selected 9 arrays.

Figure 5.9. Control experiments of DNA hybridization. One sample with TET-ssDNA functionalized PGMA brushes was cut into two pieces for the hybridization with probe and control oligonucleotides respectively. After hybridization and washing, the sample with random sequenced control oligonucleotides did not present orange fluorescence, but stronger green fluorescence than the probe oligonucleotides.

Figure 5.10. Protein immobilization on 3D-patterned PGMA brushes. (A) Fluorescent microscope images of the immobilized human IgG/FTIC-labeled anti-human IgG on the 3D-patterned PGMA brushes. (B) Cross-sectional analysis of the fluorescence intensity from one array shown in the inset of A. (C) Statistic results on fluorescence intensity versus FITC-anti-IgG concentration and brush height collected from the fluorescence image of the 3-step pyramid patterns.

Figure 6.1. Principles and fabrication of apertureless cantilever-free pen arrays. (A) Optical microscope image and schematic illustration showing the four light paths present when elastomeric pyramids are illuminated. These suggest that if the light incident on the back layer could be blocked, light at the tip of the pen will dominate the optical interaction with the surface. (B) Schematic of the fabrication of the apertureless BPL pen arrays: (i) evaporation of 5 nm Ti and 200 nm Au on hard polydimethylsiloxane (*h*-PDMS) pen arrays; (ii) spin coating of PMMA that only covers flat region of the pen array; (iii) chemical etching of metal layer followed by removal of PMMA. (C) Scanning electron microscopy (SEM) image of the as-fabricated apertureless pen arrays. (D) Schematic of scanning optical lithography using the apertureless cantilever-free pen arrays.

Figure 6.2. Force dependence in photoresist patterns generated with an apertureless cantilever-free pen array. (A) Dark field optical microscope image of a large region of developed photoresist patterns. Each 7 × 3 array of dots is written by a single pen under same exposure dose but with a z-piezo extension that increases from left to right. (B) Tapping-mode AFM image of a typical dot array showing the change in size and shape with increasing z-piezo extension from left to right. (C) Average size of features written at varying z-piezo extension.

Figure 6.3. Effect of exposure dose on the photoresist patterns generated with an apertureless cantilever-free pen array. (A&B) Dark field optical microscope

images of a large region of developed photoresist patterns by varing exposure dose (A), and one typical array of dots produced with varied exposure time from 1 to 10 s and Z_{ext} of 0, 2, 4 and 6 µm from bottom to top row. (C) Tapping-mode AFM images of the patterned dot arrays shown in (B). Scale bars: 5 µm. (D) Plot of feature size at initial contact with exposure time. (E) Plot of volume of developed photoresist versus z-piezo extension. (F) Plot of fraction of remaining thickness in the center of patterns versus the logarithm of exposure time. (G) Statistic results of maximum depth in photoresist patterns with the exposure time and the z-piezo extension.

Figure 6.4. Near-field intensity profiles generated by FDTD simulations. (A) From top to bottom: intensity profiles at horizontal planes at the top, in the middle and at the bottom of photoresist and at a vertical plane. The tip size is 0.2 µm. (B-C) The same information as (A) for the tip sizes of 1.2 and 3.2 µm. Scale bar: 2 µm.

Figure 6.5. Generation of feature gradients with force-tuned size and shape. (A) Schematic of a tilted lithography experiment using apertureless pen arrays. (B) Representative dark-field optical microscope and SEM images of Au dot arrays generated at the left, middle and right edges of a ~0.5 cm wide pen array. Here, the average sizes were 2.91 ± 0.12 µm, 1.48 ± 0.07 µm and 0.41 ± 0.09 µm from left to right. Scale bars are 100 µm and 5 µm, respectively.

Figure 6.6. (A-B) SEM images of Au patterns arrays fabricated with 40 nm photoresist and 150 nm lift-off resist. By adjusting Z_{ext} and exposure time, we obtained Au features with various shapes (A) and dot arrays with average size of 250±30 nm (B). (C) Au lines patterned by adjusting Z_{ext} to write pixels with different sizes.

Figure 6.7. Simultaneous delivery of optical energy and materials. (A) Schematic of photochemical printing of Rhodamine-modified thiol inks by thiol-ene photochemistry. (B) Fluorescence microscope image (λ_{ex}= 537-562 nm, λ_{em}= 570-640 nm) of the patterned 4 × 3 arrays with illumination times of 1, 2, 3, and 4 min from bottom to top rows by apertureless pens. (C) Fluorescence microscope image of an array patterned by a single pen, showing dots with (right 3 columns) and without (left 1 column) UV illumination. Scale bar: 10 µm. (D) Intensity profiles of the patterned features with different illumination times as well as the control group, indicated by the dotted lines shown in (C).

Figure 7.1. Schematic illustrations of (A) the structures of dual-elastomer tip and traditional homoelastomer tip, and (B) the fabrication process of dual-elastomer tip array.

Figure 7.2. (A) Digital image of the transparent dual-elastomer tip array. (B) Zoom-in optical microscope image of a dual-elastomer tip (upper) and a homoelastomer tip (lower), where a clear boundary can be seen in the dual-elastomer tip. (C)Top-view and (D) cross-sectional SEM images of the

dual-elastomer tip array. Inset is a zoom-in image of the tip. (E) SEM images and EDX analysis of one tip of the dual-elastomer tip array in cross section and top view.

Figure 7.3. (A) Optical microscopes image of large-area Au patterns fabricated with a dual-elastomer tip array. (B) Zoom-in SEM image of one 15×15 array shown in (A), in which *z*-piezo extension was increased from 0 to 7 μm with a stepwise increment of 0.5 μm from bottom to top. (C) Plot of feature size versus *z*-piezo extension in (B), together with the results of control experiment using conventional homoelastomer pen arrays. (D) Plot of the feature sizes made by 50 tips across 4 mm distance.

Figure 7.4. (A&B) Optical microscope images of PEG dot arrays printed by the dual-elastomer tip arrays, in which a 7×6 dot array (pitch=5 μm) was patterned by each tip with gradual increase in z-piezo extension from 0 to 6 μm (dwell time=1 s), and a 10×3 dot array (pitch=4 μm) was patterned with dwell time increasing from 1 s to 10 s (z-piezo extension=2 μm), under 90%RH. (C&D) Tapping mode AFM images of the generated arrays in A. The force dependence of PEG features made by conventional homoelastomer tip is also shown in D as a comparison.

Figure 7.5. (A) Fluorescence microscope image of large-area fluorescent PEG/Rhodamine B dot arrays. The insert is a zoom-in image of a typical 8×8 array. (B) Feature size statistics of the fluorescent dots measured from 12 arrays in E.

Figure 7.6. (A) Schematic illustration of the FE model used for simulating the tip-substrate contact during a PPL process (the conic angle $\theta = 33$ deg; the tip radius $\rho = 100$ nm; the Young's modulus $E_s = 5.5$ MPa and Poisson's ratio $\nu_s = 0.33$ for the soft base; the Young's modulus $E_a = 1.1$ GPa and Poisson's ratio $\nu_a = 0.33$ for the hard apex; and the total height of the tip $h_t = 40$ μm). (B) von-Mises stress contour plot of the deformed dual-elastomer tip with a flattened apex, and (C) comparison of the contact radius as a function of the tip extension for different tip designs.

Figure 7.7. The FE model constructed by using the commercial package ANSYS™, which is meshed with the finest element size concentrated towards the tip apex while the coarsest in the area far away. During the simulation, the silicon substrate is pushed upwards while the tip maintains stationary, which equivalent to press down the AFM tip against a 'stationary' substrate.

LIST OF ABBREVIATIONS

AFM	Atomic Force Microscope
ATR-FTIR	Attentuated Total Reflectance Fourier Transform Infrared Spectroscopy
ATRP	Atomic Transfer Radical Polymerization
BPL	Beam Pen Lithography
DMD	Digital Mirror Device
DMPA	2,2-Dimethoxy-2-phenylacetophenone
DNL	Dip-pen Nanodisplacement Lithography
DPN	Dip-pen Nanolithography
EBL	Electron Beam Lithography
EDX	Energy-dispersive X-ray Spectroscopy
EG_3	11-Mercaptoundecyl tri(ethylene glycol)
ELD	Electroless Deposition
FDTD	Finite-Difference Time-Domain
FE	Finite-Element
HMDS	Hexamethyldisilazane
LFM	Lateral Force Microscopy
μCP	Microcontact Printing
MAPTMS	[3-(methacryloyloxy)propyl]trimethoxysilane
MHA	16-Mercaptohexadecanoic Acid
MUDBr	ω-Mercaptoundecyl Bromoisobutyrate
NIL	Nanoimprint Lithography
ODT	Octadecanethiol
OEG	Oligo (ethylene glycol)
OTS	Octadecyltrichlorosilane
PDDT	Poly(3-dodecylthiophene)
PDMS	Polydimethylsiloxane
PEDOT:PSS	Poly(3,4-ethylenedioxythiophene):Polystyrene sulfonate
PEG	Poly(ethylene glycol)
PEO-*b*-P2VP	Poly(ethylene oxide)-*b*-poly(2-vinylpyridine)
PET	Poly(ethylene terephthalate)
PGMA	Poly(glycidyl methacrylate)
PMETAC	Poly[2-(methacryloyloxy)ethyl-trimethylammonium chloride]
PMMA	Poly(methyl methacrylate)
PPL	Polymer Pen Lithography
PPV	Poly(phenylenevinylene)
RSD	Relative Standard Deviation
SAM	Self-assembled Monolayer
SEM	Scanning Electron Microscopy
SI-ATRP	Surface-initiated Atom Transfer Radical Polymerization
SNOL	Scanning Near-field Optical Lithography
SPL	Scanning Probe Lithography

CHAPTER 1 INTRODUCTION

1.1 Background and Challenges

Surface modification with functional polymers is an essential issue to a broad research fields including surface science, polymer science and engineering, and textile technology. Polymer materials have shown many superior properties on the nanometer length scale to their bulk. Engineering surface with nanoscale manufactured polymer structures has spurred widespread achievements in several important fields: (1) the device fabrication in semiconductor microelectronics, light-emitting displays, microelectromechanic systems, wearable electronics etc.; (2) the generation of masks and templates for nanofabrication; (3) the creation of functional or “smart” surface structures such as photonic crystals and self-cleaning textiles; (4) biological and medical applications including bio-array, cell-material interface, tissue engineering and diagnostics; (5) fundamental understandings in surface science, polymer science and combinatorial synthesis.[1-5]

To develop better understanding on the nanoscale polymer behavior and bring functional polymers into practical device use, large-area, high-throughput nanopatterning of functional polymers is one of the most important yet challenging issues. Patterning is an indispensable tool for fabricating device and realizing function by structure design. The construction of the micro-/nano-sized circuitry by patterning is essential for electronic devices, in which the downscaling of size gives rise to enhancement of performance. Current semiconductor industry is capable of producing Si-based chips with the feature size down to 14 nm and over 1 billion transistors, however, the cost for large area is extremely high and those well-established techniques for silicon-based devices are difficult to be applied to polymers without sacrificing their properties.[1] While solution-based printing techniques affords much reduced cost and easy access to research laboratories, the resolution is limited to micrometer scale. There have been continuous efforts for size miniaturization of polymer structures into nanoscale by low-cost nanopatterning methods, including nanoimprint lithography,[6] soft lithography,[7] block copolymer lithography,[8] and scanning probe lithography.[9] Nevertheless, those methods have intrinsic orthogonal advantages and disadvantages in either the resolution, location registration, material compatibility, large-area fabrication, or throughput. Therefore, there is a great demand for developing a simple, rapid, and flexible strategy that allows one to pattern nanoscale features of functional polymers, which may significantly promote their applications.

Among the state-of-art nanopatterning techniques, scanning-probe-based approaches fulfil the requirements for convenient generation of arbitrary nanopatterns, however, the lack of throughput greatly limits their application in real devices. In addressing such challenges, this study will employ parallel arrays of scanning probes for high-throughput, direct-write manufacturing of functional polymer nanostructures. Particularly, two-dimensional (2-D) elastomeric pyramidal tip arrays will be exploited as recently developed for polymer pen lithography (PPL)[10] and beam pen lithography (BPL)[11]. Combining with the attributes of microcontact printing (μCP)[12] and dip-pen nanolithography (DPN)[13], PPL is capable of large-area, high-throughput writing of soft materials, including small molecules, polymers and biomolecules. And BPL shows the ability to perform mask-free, diffraction-unlimited photopatterning with resolution down to 100 nm. So far, there are only a few literature reports on nanopatterning of functional polymer nanostructures by scanning probe/polymer pen array, and the applications of the large-area patterning have seldom been demonstrated, which is considered as the main research gap to fill in. Furthermore, it is also important to address the fundamental challenges associated with the parallel scanning probe lithography (SPL) techniques through a combination of material and engineering development of the probe array and other innovations.

1.2 Research Objectives

This study is concerned with new technology development aiming at nanopatterning of functional polymers in a large-area, high-throughput way by parallel scanning probe arrays. The research objectives are defined as follows:

1. To develop the chemistry and methodology for patterning functional polymers by parallel pen arrays, including 1-D array DPN, PPL and BPL.
2. To control the size and registration of the nanostructures in the three dimensions.
3. To characterize the structures of the patterned features by spectroscopic and microscopic methods and explore their applications.
4. To develop new cantilever-free pen array by optimizing the material and tip structure of the pen array.

1.3 Research Originality

The originality associated with this research project mainly contains the following two aspects:

First, the study presents the chemistry and methodology development for patterning fluorescent conjugated polyelectrolytes, polymer matrix with catalysts and 3D polymer brush nanostructures based on parallel DPN and PPL. A systematic investigation on the ink transport behaviour of conjugated polyelectrolytes is conducted to generate fluorescent nanoarrays with sub-100 nm feature size. A matrix-assisted catalytic printing technique is developed to fabricate metal nanostructures on flexible substrates through solution processing. The large-area patterning of 3D polymer brushes enables spectroscopic analysis of the patterned nanostructures and practical applications in nanofabrication and biochips. In contrast, such achievement is a daunting task for many low-throughput serial patterning methods.

More importantly, the study has original contribution to the technological development of large-area, high-throughput surface nanopatterning by cantilever-free SPL. Two novel polymer pen arrays are invented for PPL and BPL to extend the patterning capabilities. The apertureless pen array significantly lowers the barrier for high-resolution photopatterning and allows the control on surface chemistry with multiplexed approaches including light, force and material. The dual-elastomer tip array for the first time exploits a multilayered tip structure to tune the tip deformation, which can be fabricated by low-cost moulding method and shows great improvement in the resolution and uniformity for large-area nanopatterning.

1.4 Outlines of the Thesis

The thesis is organized as the following sections:

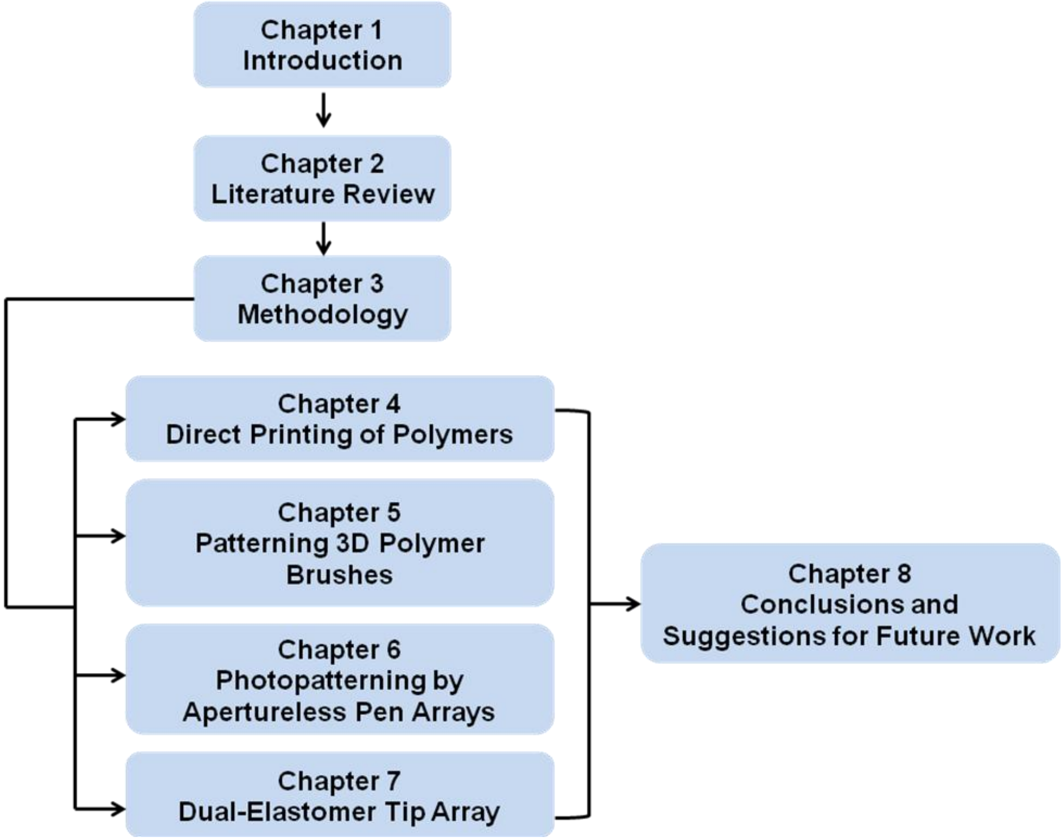

Figure 1.1. Research framework and thesis outline.

Introduction

Chapter 1 introduces the background of nanopatterning of functional polymers and current challenges. Then it states the research objectives and the original contributions of the study.

Chapter 2 first gives a brief introduction to the nanopatterning techniques including conventional and unconventional ones. After that, it comprehensively reviews the scanning probe lithographic approaches to patterning functional polymers developed so far, and the recent development of parallel probe arrays.

Chapter 3 elaborates the research methodology, including materials, preparation of substrates and pen array, lithographic apparatus and characterization techniques.

In Chapter 4, the results of polymer patterns direct printed by parallel DPN and PPL are presented, as well as the use of polymer matrixes for fabricating metal nanostructures by solution processing.

In Chapter 5, the fabrication of complex 3D patterns of functional polymer brushes is demonstrated through combination of polymer pen lithography (PPL) and surface-initiated polymerization. Then the applications of the 3D patterns in micro/nanofabrication and bioimmobilization are discussed.

In Chapter 6, scanning optical lithography and photochemical printing using a novel cantilever-free apertureless pen array are introduced. The principle, fabrication and patterning results of the pen arrays are elaborated.

In Chapter 7, the development of dual-elastomer tip array is reported for improving patterning capability. The fabrication and characterization of the tip array are presented. And the experimental and simulation results on patterning by the dual-elastomer tip array are discussed.

Lastly, the conclusions are summarized in Chapter 8 and some future outlooks will be suggested.

CHAPTER 2 LITERATURE REVIEW

2.1 Nanopatterning Techniques for Functional Polymers

Nanopatterning is the process to define ordered surface structures with minimum dimension in the nanometer scale. The conventional lithographic techniques used in current semiconductor industry for nanoscale fabrication, typically photolithography and scanning beam lithography, have been driven to produce features with either high throughput or high resolution. The state-of-art photolithography has realized patterning of billions of 14-nm structures over a 300 mm (12″) wafer within 1 minute for chip manufacturing. However, it needs other maskless lithographic techniques to define masks, such as electron beam or direct laser writing. On the other hand, scanning beam lithography using focused electrons or ions beam is a serial tool to fabricate arbitrary patterns with resolution below 10 nm, although the patterning area is usually limited within several mm^2 and the writing time is approximately 10-million-fold slower than photolithography.[14] Nevertheless, the direct irradiation by photon or electron is inherently not applicable to many functional polymers since it will induce the degradation of polymers or the deterioration of properties,[1] not to mention the tremendous expenses on instruments and specific environment (eg. cleanroom, mask aligner, e-beam system). Thus a variety of cost-effective unconventional techniques based on mould, stamp, self-assembly or scanning probe have been developed as more simple, flexible and versatile nanofabrication tools for soft materials involved in chemistry and biology to avoid harsh processing conditions.[15-16] Among them, scanning probe lithography (SPL) possesses unique advantages in direct writing, sub-10 nm resolution, nanometer registration, non-destructive manipulation at molecular level, easy operation and relatively low cost. The development of parallel scanning probe arrays has further extend the capability of SPL for large-area (>1 cm^2), high-throughput nanofabrication, enabling it as a competitive nanolithography candidate in both academic and industrial fields. In the following sections, an overview of the above conventional and unconventional nanopatterning techniques will be presented first, with focus on the patterning capability for functional polymers. Next, a comprehensive literature review on strategies for nanopatterning of polymer by SPL will be elaborated, in which special attentions will be given to the recent progress in parallel scanning probe arrays.

Table 2.1

Techniques	Resolution (nm)	Throughput (cm^2/s)	Patterning Area	Remarks
Photolithography	14	>20	12″ wafer	need pre-defined mask and cleanroom; radiation damage to polymer
E-beam Lithography	5	10^{-6} - 10^{-5}	<1 cm^2	arbitrary writing; high cost; low efficiency
Nanoimprint Lithography	10	>4	8″ wafer	need pre-defined mould; low cost; heat or radiation damage to polymer
Soft Lithography	50-100	>100	6″ wafer	need pre-defined soft stamp; non-destructive; low cost; easy operation
Block Copolymer Self-assembly	1-20	>0.1	12″ wafer	need special polymers and processing; difficulty in long-range order control
Scanning Probe Lithography	1-20	10^{-8} (single) >10^{-3} (parallel)	10^{-4} cm^2 (single) >1 cm^2 (parallel)	arbitrary writing; high registration; either non-destructive or destructive; low efficiency by single tip

Table 2.1. Current capabilities of conventional and unconventional nanopatterning techniques.

2.1.1 Conventional Lithography

Photolithography is a parallel replicative patterning method based on the light illumination through a pre-fabricated photomask to the desirable regions of substrate, followed by, if needed, removing the selected area of the film by solvent dissolution, also called as development. The selectively exposed regions of the photoactive monomer, polymer or self-assembled monolayer (SAM) surface can be triggered to undergo crosslinking, decomposition, polymerization and functionalization, leaving positive or negative pattern replicas of the original mask. Photolithography has served as cost-effective, high-throughput patterning method on wafer scale (Figure 2.1A), however, its resolution is limited by the diffraction rules of light. High resolution below 100 nm can be achieved by incorporation with various methods such as short-wavelength irradiation, projection, oil immersion, new photoresist, phase-shift mask and interference lithography etc.[2, 15] Nevertheless, these high-resolution techniques require cleanroom and special materials and set-up, significantly increasing the cost and the fabrication complexity. Also the processing conditions are usually incompatible with most functional polymers. For example, the optical and electronic properties of conjugated polymers will be diminished under photoirradiation. Many bio-related materials will be deactivated upon contact with UV light, photoinitiators and solvents used in the process. Therefore, photolithography is mostly applied to patterning features with size above several micrometers in research use, except for a few examples of submicrometer patterning. For instance, soft phase-shift mask was reported to fabricate nanopatterned light emitting device.[17] And interference lithography was used to create patterned polymer brush gradients.[18]

Electron beam lithography (EBL) is the main choice for serially writing arbitrary nanostructures with resolution as high as a few nanometers. The focused electron beam can induce selective etching or crosslinking of the polymer resists. Poly(methyl methacrylate) (PMMA) serves as the most commonly used positive resist to achieve a 20 nm resolution, while hydrogen silsesquioxane (HSQ) negative resist is capable of forming sub-5 nm features by crosslinking.[19] In recent reports, EBL is also applicable to direct patterning of some functional polymers. For example, a wide variety of responsive polymer brushes can be direct patterned using electron-induced chain scission.[20-22] As shown in the atomic force microscope (AFM) image in Figure 2.1B, 50-nm feature size and 100-nm pitch were fabricated. Functionalized poly(ethylene glycol) (PEG) and poly(ethylene oxide) (PEO) polymer electrolyte can be crosslinked by EBL for binding multiple proteins[23] or gating nanowire transistors[24]. More recently, a silk resist has been developed for water-based, eco- and bio-friendly EBL process.[25] The main drawbacks of EBL are the highly expensive instruments and the slow writing process, which restrain its use in small area or low density. As a result, EBL is most often used to produce mask or mould for other nanofabrication tools, or to generate nanopatterns for lab-scale research.

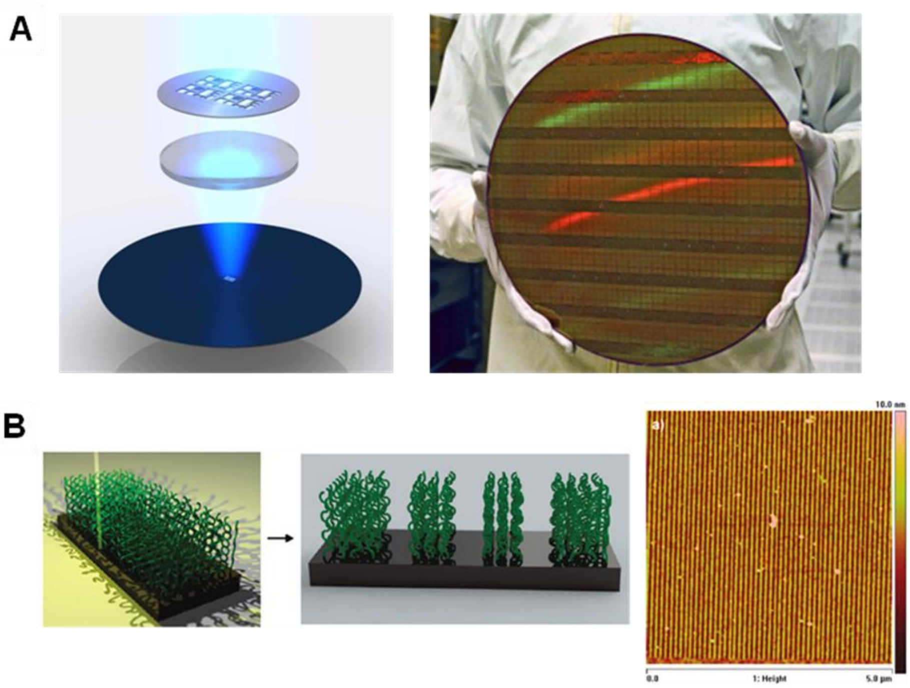

Figure 2.1. (A) Photolithography for fabricating Si chips and the image of the as-made chips on a 12″ wafer. (Courtesy: Intel Corporation) (B) Patterning polymer brush resist by EBL.[20] An AFM image shows the fabricated brush patterns with 50-nm feature size and 100-nm pitch.

2.1.2 Unconventional Nanofabrication

Compared with the energy-based conventional method, unconventional nanofabrication tools can be implemented in a non-destructive fashion and mild conditions through moulding, printing or self-assembly. Some techniques are quite simple and highly efficient for printing organic materials with extremely low cost, which are particularly suitable to pattern those vulnerable molecules in the context of chemistry and biology.

Nanoimprint lithography (NIL)[6] has been considered as a potential technique for commercial use owing to the high resolution, high throughput and low cost. In NIL, a hard mould fabricated by conventional methods (e.g. EBL) is imprinted into a soft resist layer to emboss nanopatterns (Figure 2.2A).[26] Sub-20 nm resolution and a throughput of 300 disks per hour have been claimed for manufacturing hard-disk drives.[27] As the earliest developed approach, thermal NIL has shown wide applications, in which the relatively inexpensive metal mould is employed and roller fabrication of sub-100 nm features is available.[28] In thermal-NIL, a thermoplastic resist is heated and softened above its glass transition temperature (T_g), hence the imprint in some cases requires vacuum or nitrogen environments to prevent material degradation at such high temperature. To avoid these conditions, step-and-flash imprint lithography (SFIL) has been developed for rapid and room temperature NIL, in which a low-viscous, photo-curable monomer solution is moulded and UV-cured through a transparent mould.[29] Alternatively, based on the free volume reduction and plastic deformation of thermoplastic materials upon pressure,[30] NIL has also been performed at room temperature without the need for temperature cycling or irradiation, which is highly desirable for patterning conjugated polymers while maintaining their optical properties.[31-32] Currently, NIL has been extensively exploited in large-area nanofabrication, particularly for the production of high-density periodic nanostructures for light trapping[33-34] or information storage,[35-36] and the high-speed roll-to-roll fabrication on flexible substrates[37-38] (Figure 2.2B). Another unique advantage for NIL is to tune the molecular ordering of functional polymers by nanoscale confinement during patterning. Controlled crystallization and alignment of polymer chains were observed in the nanostructures of electronically active polymers patterned by NIL (Figure 2.2C), showing enhanced electronic properties.[39-42] In addition, high performance solar cell and memory devices consisting of the well-ordered polymer nanostructures have been demonstrated by taking the advantage of NIL.[43-44]

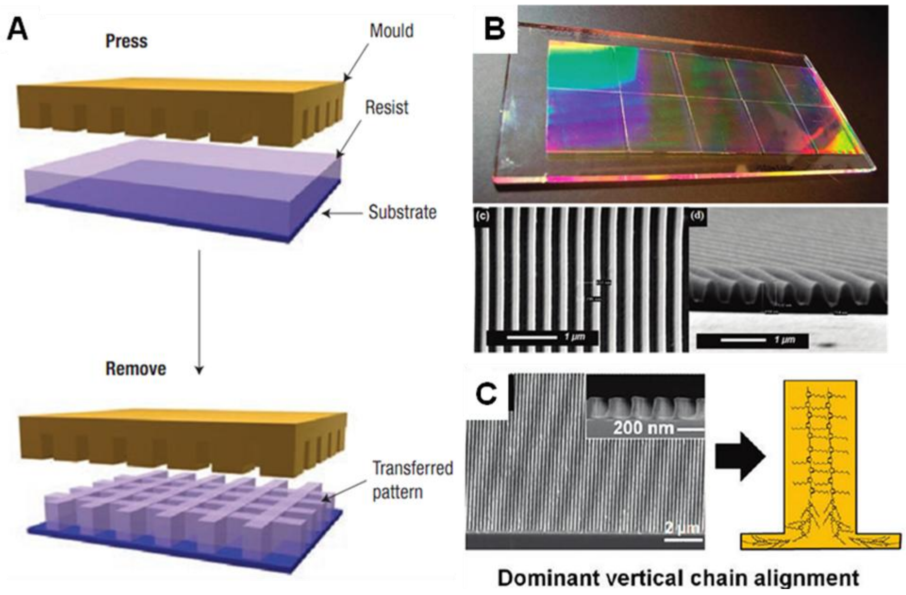

Figure 2.2. Nanoimprint lithography (NIL). (A) Schematic of NIL process.[1] (B) Large-area grating patterns on glass produced by roll-to-roll NIL.[38] (C) Chain alignment of conjugated polymers induced by NIL.[41]

Direct printing of materials with a soft stamp is a more straightforward way to pattern surface, namely microcontact printing (μCP), which is a typical branch of soft lithography[7, 45-46]. The elastomeric stamp, commonly made of polydimethylsiloxane (PDMS), can be easily prepared by replica moulding from a pre-made hard mould. The ink materials are additively printed on the substrate by conformal contact between the ink-coated stamp and the substrate (Figure 2.3A). Patterning by μCP is a simple and universal method for a wide variety of polymer materials without compromising their functions, including polyelectrolytes, polymer brushes, biopolymers and conjugated polymers.[47] The main restriction for μCP is the limited resolution in micrometers resulting from the easy deformation of the soft stamp and the uncontrollable ink diffusion.[48] Improvements in stamp materials and printing methods have been studied to extend the printing to nanoscale. For instance, the use of hard stamps[49-50] or composite stamps with a combination of rigid and soft elastomers[51-52] has allowed nanocontact printing of sub-50 nm features (Figure 2.3B). Stamps with chemically patterned barriers[53-54] or nanostencil masks[55] have shown effectiveness to reduce ink diffusion for printing sub-100 nm features (Figure 2.3C). By utilizing the edge transfer printing, polymer nanostructures with 100-nm size can also be generated through thermal crosslinking[56] or electropolymerization[57]. Yet the low feature density remains to be addressed for these techniques.

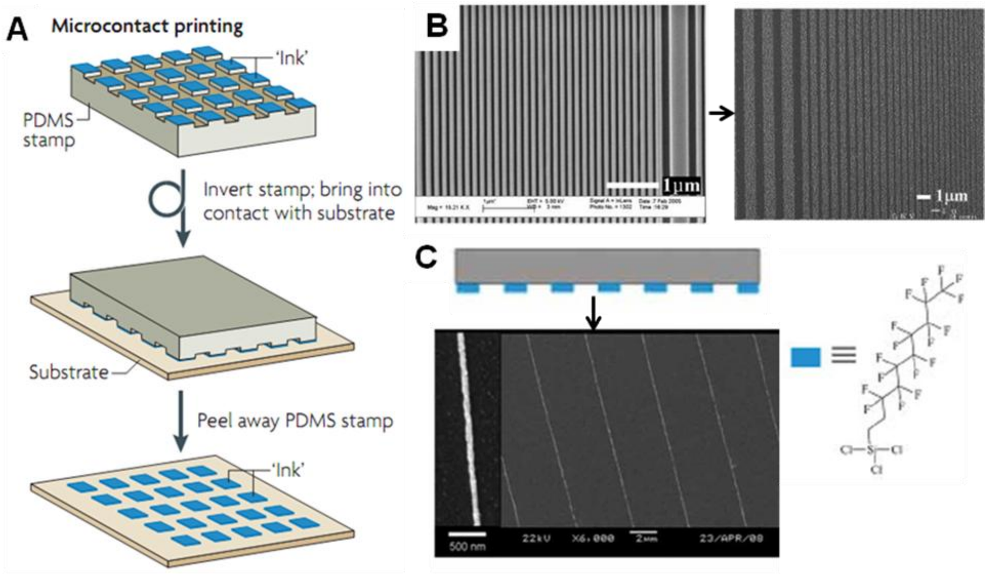

Figure 2.3. Contact printing. (A) Schematic of μCP.[46] (B) Hard stamp with 70 nm line/space patterns for nanocontact printing (left) and the resulted polystyrene nanobeads (~96 nm) deposited on printed polyelectrolytes patterns (right).[49] (C) Chemically patterned flat stamp for printing sub-100 nm features.[53]

The mould or stamp can be also used to define nanopatterns of solution processable materials by capillary force, such as micromoulding in capillaries (MIMIC)[58], lithographically controlled wetting (LCW)[59-60] and liquid-bridge-mediated nanotransfer moulding (LB-nTM)[61]. In MIMIC, a patterned stamp is placed onto a surface to form a network of micro or nanosized channels. Then the channels are filled with liquid solutions by capillary flow with the assistance of vacuum, leaving patterns after solidification and stamp release. Thus MIMIC is appealing for patterning solution processable polymers to sub-100 nm features without damage of any chemical or physical properties (Figure 2.4A).[62-63] The second technique, LCW, employs the meniscus established between the protruding patterns of a stamp and the liquid surface on the substrate to form pattern replicas.[60] The self-organization of functional ink materials under spatial confinement has been demonstrated to fabricate high performance nanowire electronic devices (Figure 2.4B).[64-65] Finally, LB-nTM allows transfer of solid materials trapped in the well of a nanopatterned mould to a surface aided by the capillary bridge formed between the mould and a liquid media layer (Figure 2.4C).[61] Again, the nanoscale confined transfer process enables molecular order of functional materials in the final patterned nanostructures.[66]

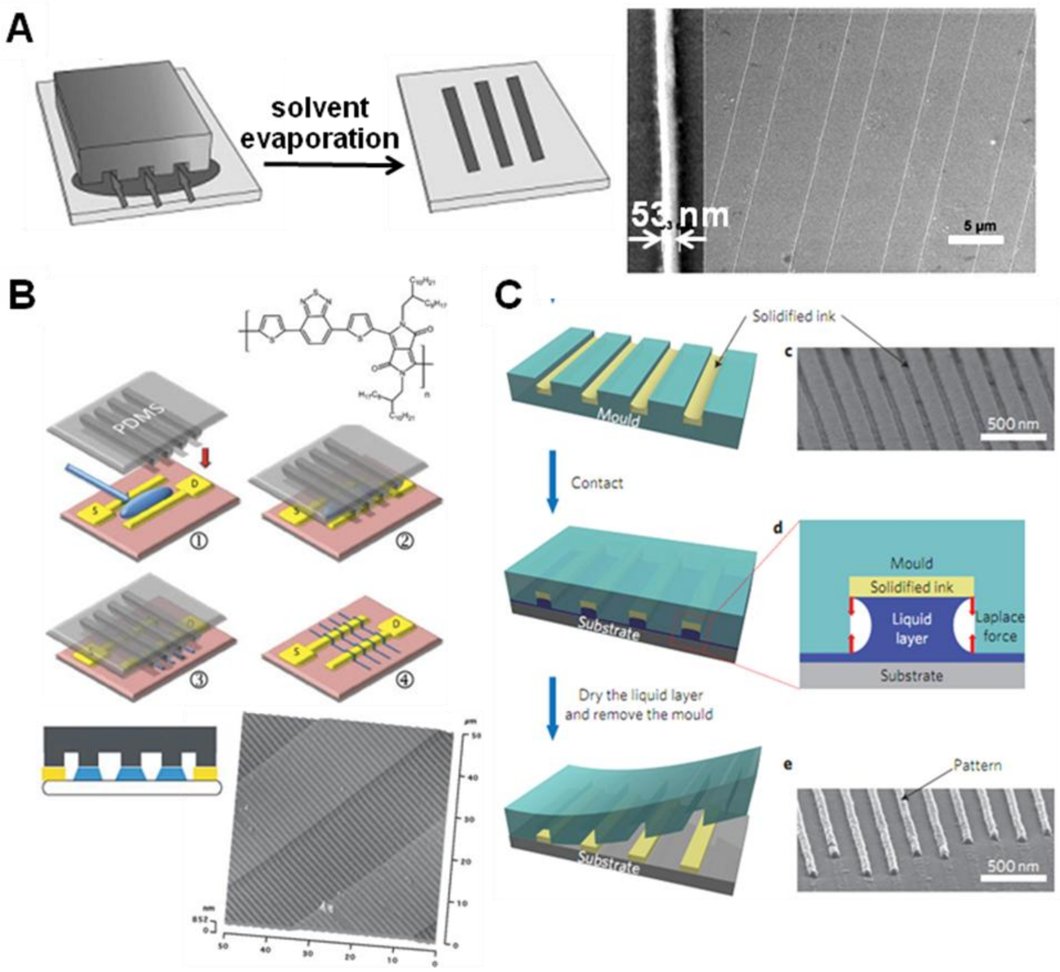

Figure 2.4. Moulding by capillary force. (A) MIMIC in nanochannels to fabricate 50-nm line patterns.[63] (B) Fabrication of nanowire-based organic electronic device by LCW.[65] (C) Procedures for LB-nTM.[61]

Besides mould and stamp, nanopatterning from bottom-up by self-assembly of block copolymers has aroused increasing attentions in fabricating high-density, sub-10 nm nanostructures over large areas. The polymer chain with two immiscible blocks can undergo nanoscale phase separation, resulting in self-organization of various nanoscopic morphologies (e. g. spheres, cylinders or lamellae) depending on the composition and chain architecture.[8] The self-organized nanostructures can generate patterns with feature size and pitch of a few nanometers, which is tunable through chemical synthesis and processing conditions. The as-obtained polymer nanostructures can be used in their own for photonics or information storage, or as templates for patterning other functional polymers and inorganic nanoparticles. Russell and coworkers reported nanoporous templates prepared from polystyrene-block-poly(methyl methacrylate) (PS-b-PMMA) can be used for electrochemical growth of conducting polymers to create individual and well-aligned polymer nanorods with an areal density ~10^{11}/cm^2.[67] Also, etching resists made from the self-assembly of poly(styrene-b-dimethylsiloxane) (PS-b-PDMS) diblock copolymer were employed to form conducting polymer nanowire arrays with 15-nm width over centimeter square area for gas sensing (Figure 2.5).[68] However, the long time to accomplish the self-assembly process, usually hours even days, makes this technique essentially low-throughput. In addition, controlling long-range order remains a challenge for achieving large-area patterns free of defects and other lithographic methods are needed to define pre-patterned regions to direct the self-assembly.[69]

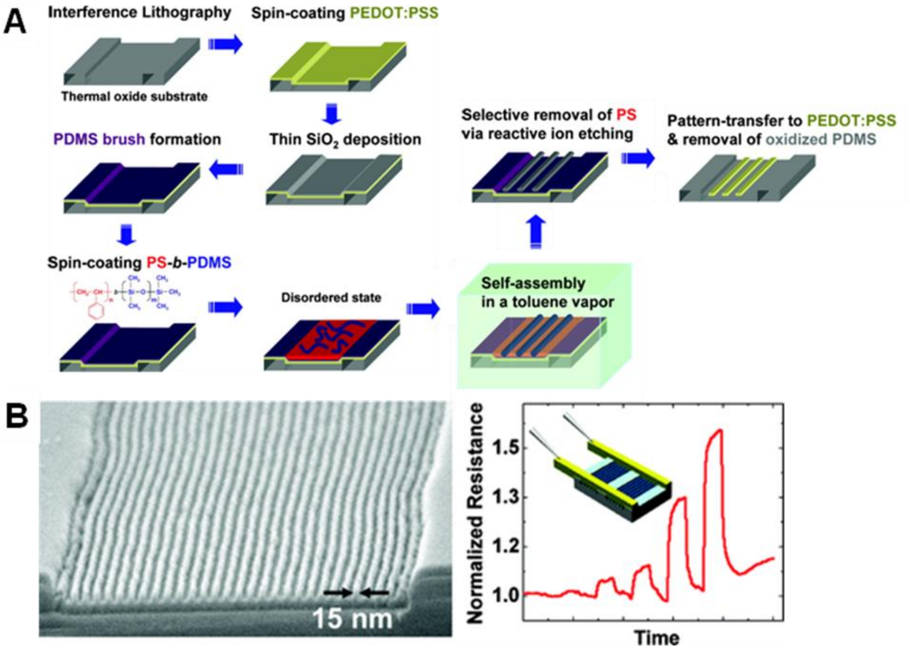

Figure 2.5. Block copolymer self-assembly.[68] (A) Schematic of nanopatterning by self-assembly of block copolymers. (B) Scanning electron microscope (SEM) image of the as-made 15-nm PEDOT:PSS nanowire arrays from block copolymer templates and their gas sensing property to ethanol.

In summary, the above unconventional approaches are inexpensive and applicable to large-area production of nanostructures on flexible and non-planar substrates. However, these techniques require the pre-fabrication of mould, stamp or template by conventional lithographic tools with fixed patterns. It fails to generate arbitrary patterns unless a new mask or mould is re-designed and prepared through tremendous efforts.[70] Secondly, as the patterns are replicated in parallel, the registration ability is poor with respect to patterning multilayered devices, which is unsatisfactory for accurate placement of different components layer-by-layer in device fabrication.

2.2 Patterning Functional Polymers by Scanning Probe Lithography

Scanning probe lithography (SPL) is a series of techniques that utilize a sharp scanning probe or an array of probes for surface patterning purposes in a direct-write fashion. The movement of probe on the surface is controlled with nanoscopic precision by the equipments including scanning tunneling microscope (STM), atomic force microscope (AFM), scanning near-field optical microscope (SNOM), scanning electrochemical microscope (SECM), and so on.[71-72] The tip is a powerful, versatile and easy-accessible tool to realize both precise spatial modification and *in situ* imaging of the structures at the nanometer, even molecule level. There are two categories of patterning strategies by SPL, the delivery of materials ranging from small molecules to macromolecules to nano-objects, or delivery of energy including mechanical, thermal, optical or electrochemical one.[9, 73-77] Thus, a variety of “constructive” or “destructive” approaches can be used for manufacturing functional polymer nanostructures and controlling molecular organization.[78] By virtue of simultaneously manipulation of multiple tips, the recent developed parallel cantilever and cantilever-free probe arrays have paved the road towards large-area, high-throughput desktop nanofabrication tool for SPL.

2.2.1 Dip-Pen Nanolithography

Invented by Mirkin's group in 1999, dip-pen nanolithography (DPN)[13, 74-75] is a direct molecular printing approach using an ink-coated AFM tip to transfer molecules onto a substrate driven by chemical or physical absorption, in which the transport of ink molecules is mediated by the water meniscus condensed between the tip and the substrate from environment (Figure 2.6A). The molecular transfer process include steps of ink dissolution in the meniscus, transport through the meniscus and molecular diffusion and organization on the substrate surface, which is significantly influenced by the environment conditions (temperature, humidity etc.) as well as the nature of both ink and substrate (ink amount, solubility, surface roughness and chemistry etc.). Importantly, for a wide range of molecules, including thiols, silanes, oligonucleotides and conducting polymers, the growth of feature size exhibits similar time-dependant relationship, i.e. a linear function between the dot area and the tip dwell time on the surface, which provides a facile way to control the pattern formation from sub-50 nm to micrometer.[74] Besides the early demonstrated and extensively studied molecular inks in DPN, recent reports have proposed another kind of ink called as liquid ink with different transport mechanism. The liquid inks should be highly viscous to provide good adhesion to the tip and the mobility to flow onto the substrate upon tip contact. Unlike molecular inks, it is not necessary for the condensed water meniscus to be involved in the ink transport, but the capillary force between the liquid ink and the substrate and the rupture of the meniscus bridge dominates the material transfer instead.[79-82] Thus the ink viscosity and the capillary bridge play important roles in determining the feature size of liquid inks in addition to the conventional parameters in molecular diffusion (contact time, humidity, etc.). Also, the liquid ink deposition results in bulk transfer of materials and topographic patterns rather than molecular monolayer. Because liquid ink can be printed more easily regardless of ink-substrate interactions, it has greatly extended the applications of DPN to a wide range of materials such as hydrogels, polyols, block copolymers, polymer precursors etc., and substrates either inorganic or polymer, flat or rough.

Polymers can be printed by DPN through molecular diffusion by choosing proper ink-substrate interactions. Charged conducting polymers, such as sulfonated polyaniline and doped polypyrrole, were transferred on the substrates with opposite charges through electrostatic force, forming molecular monolayer or multilayer patterns with the smallest feature size close to 130 nm.[83] The molecular transfer was also observed in patterning polyelectrolytes[84-85] and dendrimers[86-87] with electrostatic or covalent bonding to the surface. Gas sensor was also made by the deposited conducting polymer nanostructures.[88] Driven by weak Van der Waals interaction, DPN was also explored to fabricate polystyrene,[89] luminescent conjugated polymer[90] and ferroelectric polymer[91-92] nanostructures despite that the ink molecules exhibit very poor water solubility. Remarkably, by precisely placing a nanodot of ferroelectric polymer at the center of a single-walled carbon nanotube channel, DPN was demonstrated to implement the fabrication of a nanoscaled nonvolatile memory device (Figure 2.6B).[92]

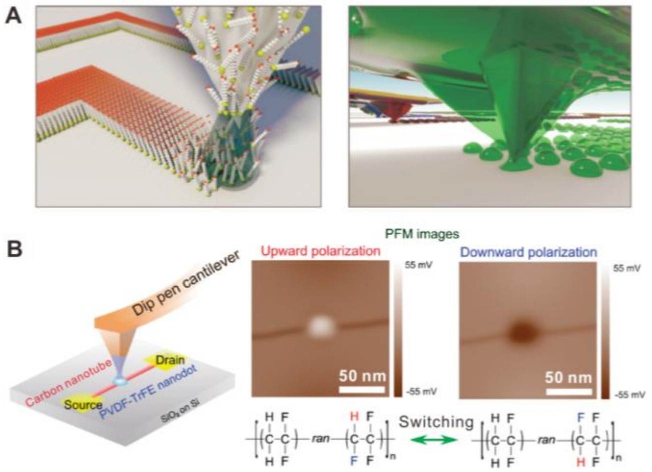

Figure 2.6. Dip-pen Nanolithography (DPN). (A) Schematic of meniscus-mediated transport of molecular and liquid ink by DPN. (Courtesy: Nanoink, Inc.) (B) Memory device fabricated by DPN-deposited ferroelectric polymer nanostructures.[92]

In recent progress, patterning liquid-like polymer inks by DPN has further promoted fruitful applications. As the most representative example, PEG has been exploited as a multifunctional material for various lithographic applications (Figure 2.7A). PEG absorbs a large amount of water at high humidity and becomes viscous liquid. Being “liquid”, the shape of the PEG feature is spherical-cap-like, similar to that of a water drop on a substrate (Figure 2.7B), and the thickness and the contact angle of the PEG spherical caps are related to the surface energy of the substrate. DPN-patterned PEG has served as polymer resist and sacrificial layer to generate both positive and negative nanostructures combined with wet chemical etching.[93] And metal photomasks were fabricated following the steps of DPN patterning of PEG resist, metal evaporation and lift-off process (Figure 2.7C).[94] In another example, Zheng et al. deposited the PEG resist on a flat PDMS surface as resists for plasma treatment.[95] After backfilling of various silane molecules on the unprotected areas and the removal of PEG resist, a topographically flat PDMS stamp with well-defined chemical regions was produced, which could be used for microcontact printing of small molecules, proteins, and polar inks at sub-100 nm (Figure 2.7D). Furthermore, since the DPN-deposited PEG dots on glass are hemispheric and transparent, they possess optical properties that can be employed as nanosized lenses for subwavelength photolithography (Figure 2.7E).[96] The incident light passing through PEG was focused beneath the center of the PEG lens with lower intensity at the edges, thus the PEG lens arrays were used as phase-shift photomasks to generate either well- or ring-shaped photoresist patterns. Besides, dot arrays of PDMS can be generated by DPN printing of precursors followed by thermal curing, which were used as templates for replication of stamp with inverted patterns.[97]

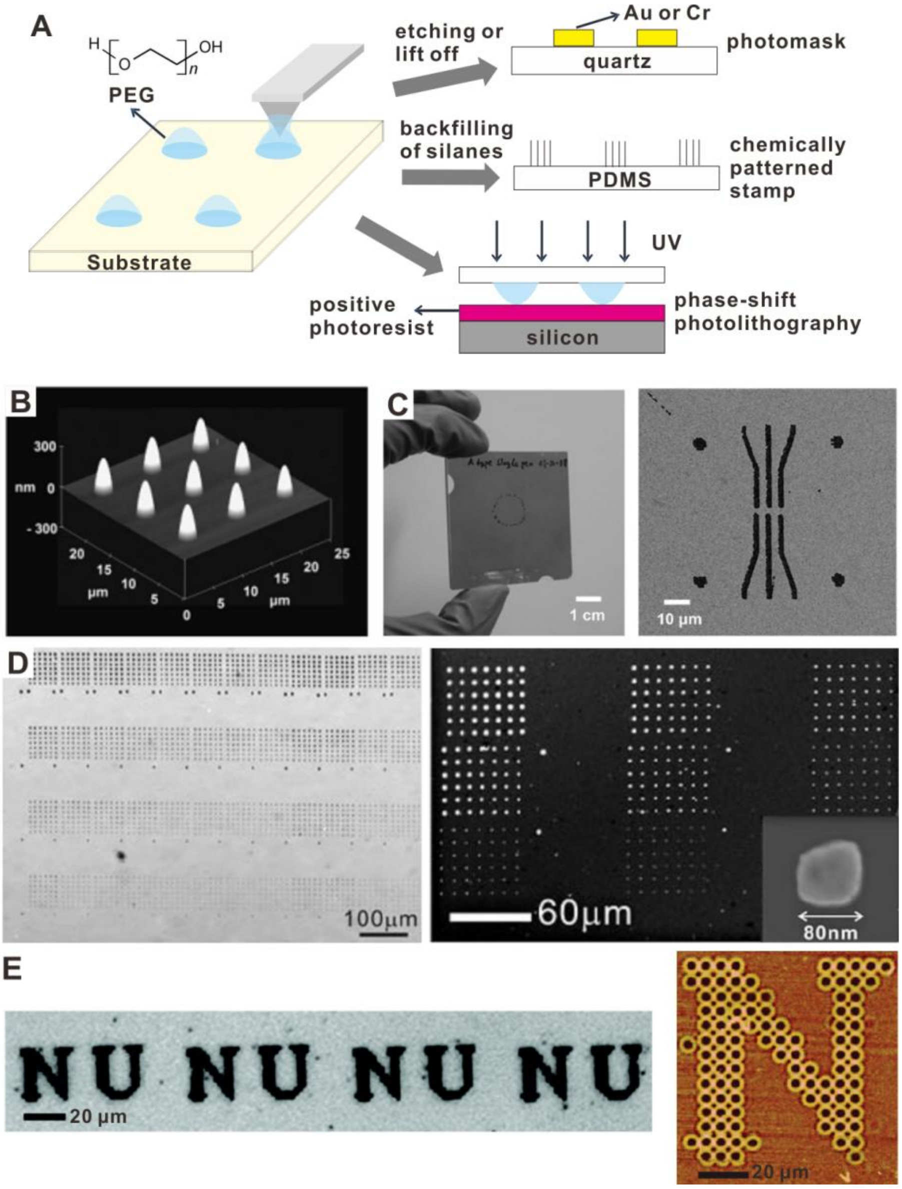

Figure 2.7. PEG resists fabricated by DPN for multifunctional applications. (A) Schematic illustration of the fabrication and application of nanoscale PEG resists. (B) AFM topography image of the patterned PEG features.[94] (C) Optical and SEM images of the fabricated photomask from PEG resists.[94] (D) Optical microscope image of DPN-generated PEG arrays on PDMS and SEM image of Au dot arrays obtained from microcontact printing with the chemically patterned flat PDMS stamp.[95] (E) Optical microscope image of an array of photoresist patterns fabricated with PEG phase-shift lenses and an AFM image shows the letter "N" consisting of well-shaped features.[96]

More importantly, the liquid inks can also function as carrier matrixes to address the challenge for printing large biomolecules and nanomaterials. The innovation was that functional materials (such as biomolecules) or precursors of functional materials (such as inorganic salt for metallization), which are difficult to transfer directly by AFM tip, was mixed with mobile polymers. The mixture was then printed by DPN, in which the polymer matrix can carry the functional materials onto substrates. For example, the hydrogel-like PEG ink loaded with various nanoparticles, C_{60} or biomolecules can be used to pattern nanostructures on different surfaces with similar features regardless of their solubilities and size (Figure 2.8A and B).[98-100] Indeed, the nanomaterials or biomolecules were proved to be active after removing the PEG matrix by means of water rinsing or O_2 plasma. Gas sensing and photodetector devices were fabricated through the matrix-assisted liquid deposition of conducting polymers (Figure 2.8B).[101-104] Other hygroscopic inks, such as agarose hydrogel, block copolymers and glycerol, were also used as matrixes to facilitate the delivery of biomaterials including oligonucleotides, proteins and virus,[105-107] as well as metal salts and nanoparticles.[108-111] Another key advantage of the polymer carrier system is that it can effectively modulate the transport rate of the polymer/functional material mixture for high-speed and uniform printing regardless of the ink materials and substrates, because the transport characteristics of the polymer carrier dominate the system. This is especially important for achieving similar feature size between different inks in multiplex patterning of biological materials. In the case of agarose carrier, identical spot size was exhibited for two proteins (CTß and IgG) printed in the same conditions (Figure 2.8C).[105] Furthermore, Chai et al adopted block copolymers as both delivery matrixes and nanoreactors for site-selective synthesis of nanoparticles (Figure 2.8D).[112] Poly(ethylene oxide)-*b*-poly(2-vinylpyridine) (PEO-*b*-P2VP) was chosen as a preferable candidate since the PEO block promotes the ink transport while the P2VP block is associated with the metal ions as precursors. Unlike the blending situation in the hydrogel-like matrix, the block copolymer forms micelles in the solution, where a small quantity of metal ions is localized inside the P2VP core. The micelles were transported on the substrate and removed by the following plasma reduction or thermal annealing, leaving arrays of single-crystalline metal nanoparticles as small as 4.8 nm (Figure 2.8E). The versatility of block copolymer micelles was further demonstrated to generate a large library of metal, metal oxide and semiconductor nanocrystals,[113-114] which can function as active sites for attachment of single-molecule protein[115]. In addition, water-insoluble liquid ink has also been explored as host matrix, for example, a photo-curable polymer was demonstrated to deliver fluorescent conjugated molecules onto the surface.[116]

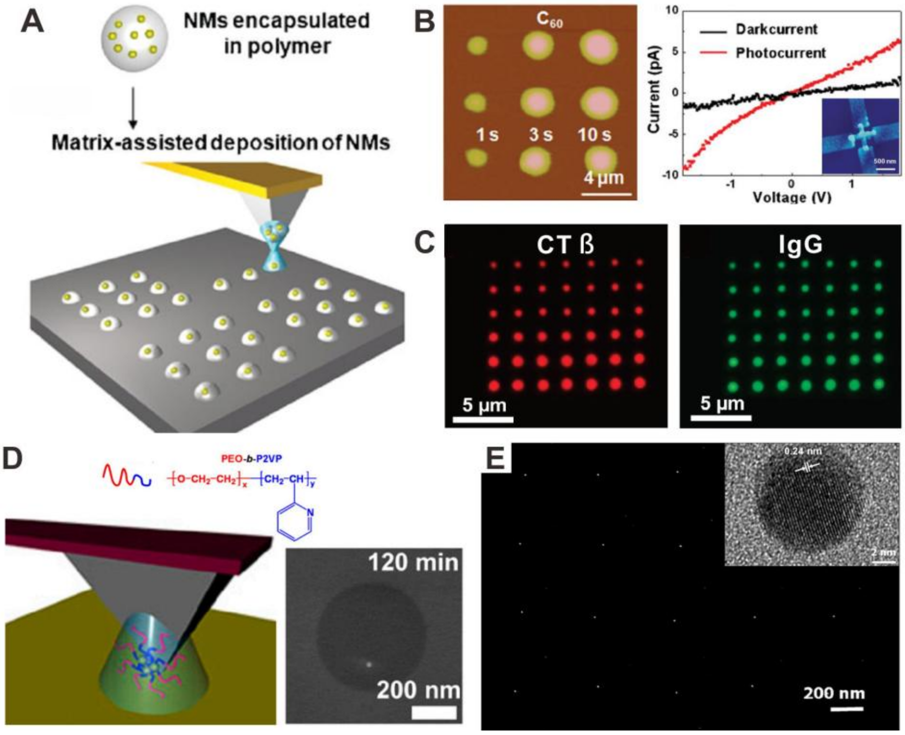

Figure 2.8. Polymer carrier matrixes for DPN. (A) Schematic illustration of matrix-assisted DPN.[98] (B) DPN patterning of C_{60} assisted by PEG matrix and the demonstration of phototransistor fabrication.[98] (C) Fluorescent images of patterns of two proteins generated with the aid of agarose matrix, showing similar feature sizes.[105] (D) Scanning probe block copolymer lithography using PEO-*b*-P2VP micelles loaded with $HAuCl_4$ as inks.[112] An SEM image shows the nanoparticle formed within the patterned polymer matrix.[114] (E) SEM image of an array of Au nanoparticles; the insert shows a high-resolution TEM image of a sub-10-nm single-crystalline Au nanoparticle.[112]

Apart from solution-based ink printing, the polymer melt can be also deposited from a heated probe whose temperature is higher than the melting point of the polymer coating, namely thermal DPN. This method is particularly suitable for patterning thermoplastic polymers with poor water solubility, in which the polymer nanostructures generated from polymer melts show several unique features. First, similar to DPN-generated polymer nanopatterns, the polymer nanostructures made by thermal DPN have functioned as resists to produce graphene nanoribbons[117] and deliver matrixes to encapsulate nanoparticles[118] as well. The molten polymers formed uniform and dense features encapsulating well-dispersed nanoparticles. After plasma removal of the polymers, lines containing aligned single particle could be obtained. Furthermore, it provides a facile way to control the molecular order and study the properties of the nanostructured polymers. Thermal DPN was used to pattern poly(3-dodecylthiophene) (PDDT), where the monolayer-by-monolayer deposition and chain alignment of PDDT could be controlled by the writing speed and tip temperature.[119] The alignment of block copolymer domains in the nanoscale was also observed in deposited nanostructures from heat tip.[120] The conductance of the as-made PDDT was measured by writing the polymer across the electrode pairs.[121] Moreover, nanoscale infrared measurements using atomic force microscopy infrared spectroscopy (AFM-IR) were conducted to identify chemical spectra of the thermally deposited polymer nanostructures.[122]

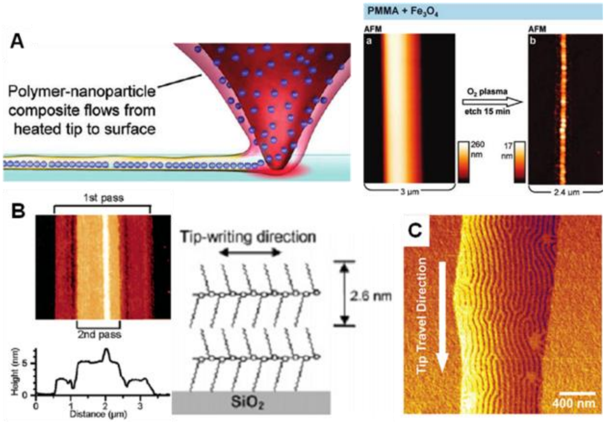

Figure 2.9. Thermal DPN. (A) Schematic of deposition of thermoplastic polymer encapsulating nanoparticles from a heated probe and AFM images of the as-made polymer nanowire and nanoparticle line after plasma treatment.[118] (B) Controlled deposition of conjugated polymer PDDT.[119] (C) Aligned domains of molten block copolymers deposited from scanning probe.[120]

2.2.2 Template-Assisted Patterning

Not only can SPL be used to direct write polymer materials, they can also generate physical or chemical templates to control the growth, assembly and phase separation of polymers in the nanometer spatially confined environment. DPN, nanoshaving and nanografting, AFM local oxidation nanolithography are commonly employed methods to produce the functional templates.[73]

Polymer nanopatterns can be produced by localized growth of polymers on the substrate. For example, the AFM tip was utilized to scratch the substrate surface to define regions with different wetting properties and therefore guide the growth of conducting polymer nanopatterns.[123-124] DPN-printed molecular templates and liquid matrix were also employed to induce photopolymerization[125] and vapor phase polymerization[109] confined in the microenvironment. Moreover, when the polymer chains are controlled to grow from the selectively immobilized initiators on the substrate, nanostructures of polymer brushes can be generated with control on the molecular weight, dimensions, chain configuration, and composition.[126-128] The examples of patterned polymer brushes by SPL include combinations of nanoshaving and atomic transfer radical polymerization (ATRP),[129] AFM anodic oxidation and ring-opening metathesis polymerization (ROMP),[130] nanografting and photopolymerization,[131] as well as DPN and various polymerization reactions,[132-135] respectively. In 2010, Zheng’s group has developed dip-pen nanodisplacement lithography (DNL) for programming patterned nanostructures of polymer brushes (Figure 2.10).[136] In DNL, an AFM tip inked with ATRP initiator molecules ω-mercaptoundecyl bromoisobutyrate (MUDBr) were used to indent or shave an Au surface pre-coated with an inert SAM, during which the original SAM layer were eliminated along with the displacement by MUDBr. Polymer brushes were then grown from the patterned initiators by surface-initiated ATRP and the lateral size and height of nanobrushes were determined by the initiator footprints (Figure 2.10B and C). More importantly, the height and shape of the nanobrushes were discovered as a function of the applied force and the lateral distance between neighboring features. A morphological transition from isolated to bridged to planar structures with decreasing lateral space between initiator footprints was observed, leading to a new concept of “feature density” method for creating arbitrary 3D-patterned polymer brushes (Figure 2.10D and E).[137] This is realized by the DNL-writing of an “initiator bitmap” with defined pixel number and pixel distance on the basis of a white/black bitmap that is converted from a gray-scale image. As a result, the density and positioning information of the bitmap can be transferred to 3D structures of polymer brushes (Figure 2.10E). This feature-density approach also allows parallel writing fashion to fabricate highly uniform 3D patterns by maintaining a high load during patterning.[138]

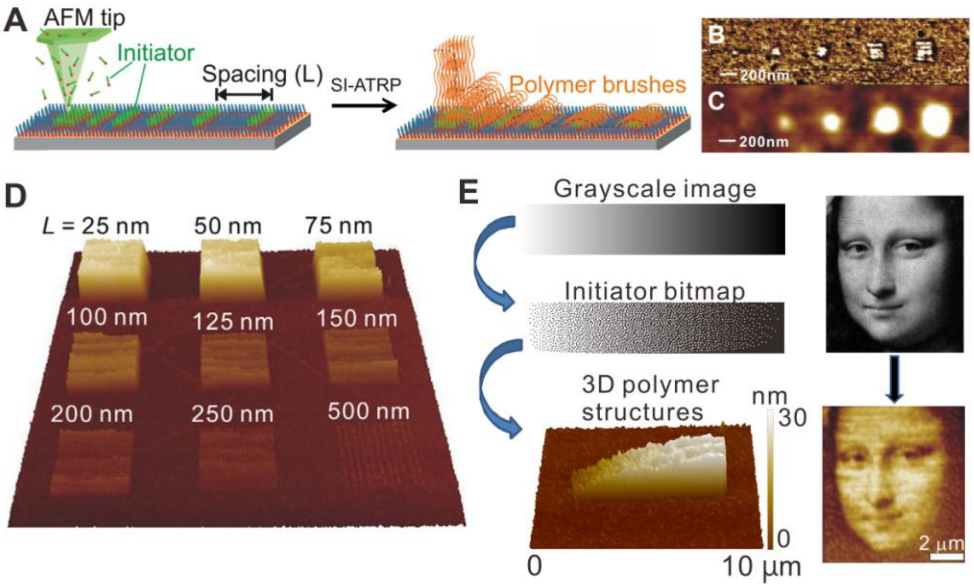

Figure 2.10. 3D polymer brushes grown from patterned initiators.[137] (A) Schematic of dip-pen nanodisplacement lithography (DNL) for controlling the height of polymer brushes. (B) Lateral force microscope image of the patterned initiator footprints by DNL. (C) AFM topography image of the as-grown polymer brushes from initiators in (B). (D) AFM image of polymer brushes with controlled height by varying the distance between initiator features. (E) Generation of arbitrary 3D patterned by feature-density method.

The polymer can be also controlled to self-organize on the SPL-generated nanopatterns. DPN and local AFM charging were used to pattern charged surfaces to direct the layer-by-layer assembly of polyelectrolytes and formation of nanostructures down to 50 nm.[139-140] Ginger's group first reported the patterned phase-separated domains of polymer blends on DPN-generated molecular templates, with a systematic screening performed on surface chemistry and feature size.[141-143] Multiscale and complex patterns were also demonstrated from the directed assembly of polymer blends.[144] In addition, tip-induced oxidation of surface alkyl groups of SAMs can generate well-defined hydrophilic/hydrophobic spaced areas, which served as model surface to investigate the directed phase separation of polymer blend[145] and block copolymers[146] on the nanoscale templates with size in the 100-1000 nm range.

2.2.3 Energy-Based Modification

The employment of external energy applied on the probe has greatly extended the capability of tip-based manufacturing for modification of polymer resists or electronically active polymers. Since SPL allows the maskless formation of patterned polymer resist at ambient conditions, the energy-based SPL shows great promise to become a low-cost desktop nanofabrication tool.

Photoreaction is the most widely used approach in nanofabrication. Scanning near-field optical lithography (SNOL), a probe-based optical lithography by coupling a UV light source to scanning near-field optical microscope (SNOM), has been developed for site-selective photochemical degradation or transformation of photosensitive materials.[147-151] A nanoscopic aperture with sub-50 nm size is opened at the tip end of a SNOM probe, and the distance between the probe and the substrate surface is less than the light wavelength, i.e. operated in the near field (Figure 2.11A). In this way, the resolution can be far beyond the mask-based photolithography since diffraction limit is invalid in the near field, not to mention the capability of arbitrary patterning. For example, SNOL has achieved a resolution of 35 nm on positive photoresists, which is less than 1/10 of the wavelength of the incident light.[152] By selecting proper photochemistry, conjugated polymers such as poly(phenylenevinylene) (PPV) have also been patterned via photo-induced oxidation or conversion using SNOL, with the patterning resolution reported to reach 60 nm recently (Figure 2.11B).[153-154] Furthermore, the UV light was utilized to selectively degrade the protein-resist oligo (ethylene glycol) (OEG) layer for absorption of proteins and oligonucleotides in the nanoscale regions (Figure 2.11C).[155-156]

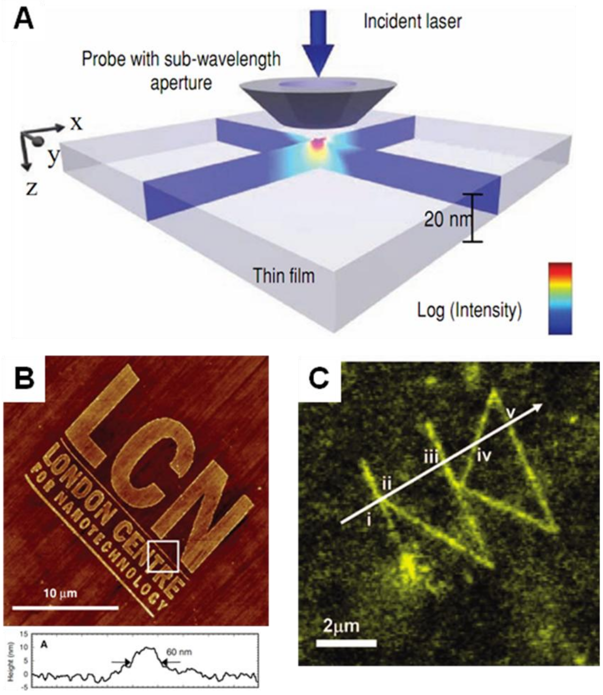

Figure 2.11. Scanning near-field optical lithography (SNOL). (A) Schematic of SNOL and the optical intensity distribution on the surface.[154] (B) AFM image of PPV patterns fabricated by SNOL.[154] (C) Nanoscale protein patterns through SNOL-induced photodegradation of OEG layer.[155]

By applying mechanical force, the sharp tip can directly eliminate the pre-coated polymer layer on the substrates in either static or dynamic mode.[157-160], leaving patterned regions with resolution depending on the tip size (typically less than 10 nm). Nanoscratching on thin film of conducting polymer poly(3,4-ethylenedioxythiophene): polystyrene sulfonate (PEDOT:PSS) has been employed as a simple, one-step approach to generate electrodes with nanoscale channels.[161] Organic transistors were fabricated by evaporating the active semiconducting materials onto the scratched electrode arrays (Figure 2.12A and B). However, the mechanical scratching commonly leads to the formation of pile-up ridges at the edges of the patterns. Although the edge effect brings undesired patterning results, Shim et al explored the use of the ridges as templates to generate features smaller than the tip size.[162] On the other hand, to avoid the debris during patterning, a liquid-phase scratching technique was developed to selectively remove polymer brush thin layer with simultaneous dissolution in the liquid environment.[163] Furthermore, tip indentation on polymer resists can be assisted by heating process, resulting in high rate and prolonged tip lifetime. Such thermomechanical indentation with reversible writing and erasing of the indents paves the way to SPM-based ultrahigh density data storage.[164-165] In previous developments, various polymer resists were synthesized with specifically designed crosslinking units to achieve sub-10 nm nanofeatures and multi-Tb/in^2 data storage.[166-169] The reversible phase change of block copolymers has also introduced new solutions to generate erasable nanopatterns. For instance, on thin film of polystyrene-*b*-poly(ethylene/butylenes)-*b*-polystyrene (PS-*b*-PEB-*b*-PS), the AFM tip in tapping mode worked as a nanohammer to deform the PS hexagonal sphere domains embedded in the PEB matrix into ellipsoidal shapes, in this way, nanopatterns were forged with sub-20 nm line resolution.[170] The written patterns were erased after annealing at 70 ℃, returning to the low interfacial energy state. Meanwhile, indentations on baroplastic polystyrene-*b*-poly(n-pentyl methacrylate) thin film have been conducted at room temperature through the tip-induced microphase transition (Figure 2.12C and D).[171] The lamellar domains of the block copolymer were turned into disordered regions by applying pressure, which could be recovered above the glass transition temperature (T_g) by local force or heat. The writing/erasure of nanopatterns on polymer medium without heating has been considered as an alternative to the existing thermomechanical SPL-based data storage.

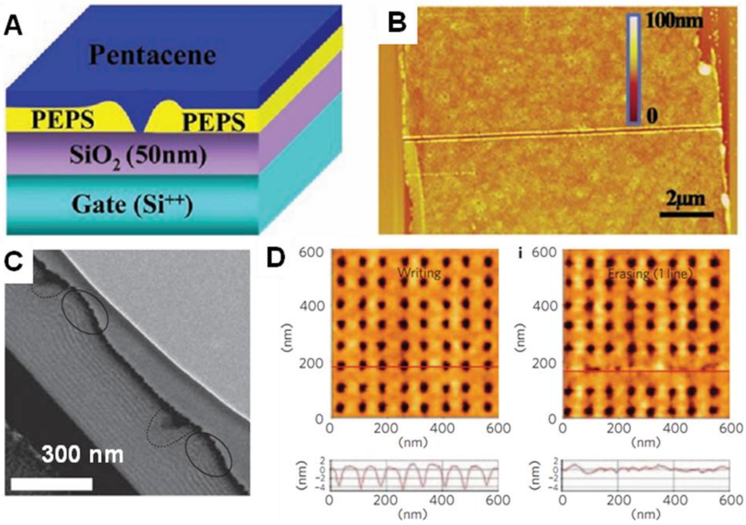

Figure 2.12. Patterning by mechanical force. (A) Schematic of organic transistor with channel defined by scratching of PEDOT:PSS electrodes.[161] (B) AFM image of the scratched PEDOT:PSS electrode pair.[161] (C) Disordered regions in the lamellar domains of the baroplastic block copolymer created by applying force.[171] (D) Writing and local erasing of nanoscale features at room temperature on the baroplastic block copolymer thin film.[171]

Thermochemical nanolithography using the heated probe to initiate surface chemical reactions affords high-resolution, high-speed patterning due to the sharp thermal gradients and rapid conversion at high temperature, although the heating condition requires specific polymer choices. The heat-induced deprotection of side groups on the polymer chains have been demonstrated to change the surface wettability and to function as templates for assembly of other materials.[172-174] Also the approach was demonstrated to generate chemical gradient by carefully controlling the conversion through the temperature.[175] Recently, Knoll and coworkers in IBM reported a novel self-amplified depolymerization (SAD) polymer resist as a fast removable template for 55-nm nanofabrication.[176-178] Notably, the SAD polymer resist has served as an ideal candidate for top-down manufacturing of 3D nanostructures by the heated tip (Figure 2.13A).[179] Since the heat-induced decomposition of the SAD polymers accomplishes within a few μs, the reaction timescale is faster than the mechanical motion of tip and the force required to penetrate the film can be ignored, as a consequence, the depth of the removed region was found to be linear with the applied load. Thus the probe-based 3D nanolithography on SAD polymer resist can be enabled in a single patterning step rather than the multicyclic layer-by-layer removal of materials[180-181]. As a demonstration, a 3D topographic world map with 5×10^5 pixels was written at a pitch of 20 nm by linearly transforming the elevation data into force information (Figure 2.13A). The whole process merely took 143 s, showing potential for high-throughput 3D nanofabrication. Thermochemical nanopatterning was also successfully introduced to conjugated molecules and polymers, which exploited a thermal conversion route from the precursor materials to the conjugated ones (Figure 2.13B).[182-185] Fluorescent PPV nanowires have been produced by scanning the heated probe on the surface of the precursor thin film, with size as small as 28 nm achieved through control on the tip-sample contact region and time. Nevertheless, the high temperature condition requires extra set of heater and protection of organic materials, and the control of thermal process may be not as easy as other techniques.

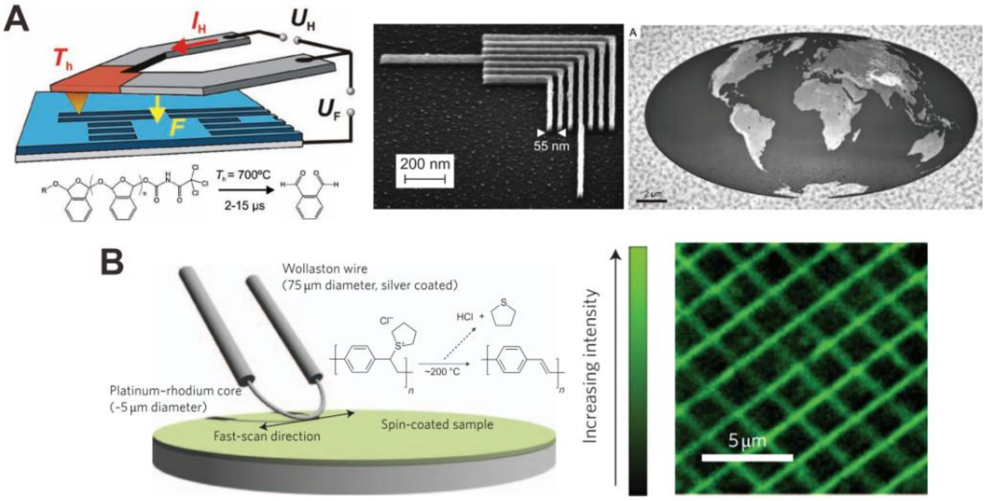

Figure 2.13. Thermochemical nanolithography. (A) Probe-based nanolithography on self-amplified depolymerization (SAD) polymer resist.[178-179] (B) Thermochemical nanopatterning on an organic semiconductor precusor. Fluorescence microscope image of the patterned PPV nanowires is shown.[182]

2.2.4 Parallel Scanning Probe Arrays for SPL

The development of parallel scanning probe tip arrays has brought SPL more competitive in fabrication throughput for both academic and industrial applications.[186-187] The pioneer work was the ‘Millipede’ concept introduced by IBM for ultrahigh density data storage utilizing a 2D AFM cantilever array of thermomechanical probes.[188] Soon, both 1D[189-192] and 2D cantilever arrays[193-194] have been developed as multi-pens to duplicate patterns for parallel DPN, allowing massive nanofabrication at sub-100 nm resolution over centimeter-scale and production of functional macroscopic devices[195-196] (Figure 2.14A and B). Active pen arrays with individual actuation of each pen were also demonstrated to generate multiplexed patterns.[197-199] Besides, Leggett and coworkers reported the development of parallel SNOL using 1D array of SNOM probes, named as “Snomipede”.[200] In Snomipede, a series of light beams are focused and pass through the optical windows on the probes, where each beam can be switched ON or OFF independently. Therefore, the tip array can work in an active style that individual probe of the array is independently operated as writing or non-writing pen, leading to the generation of different patterns from different probe in a parallel writing process. Photoresist nanofeatures down to 70 nm were demonstrated when the Snomipede was operated under water. Recently, themochemical nanolithography with parallel probe array has also been reported to pattern various functional polymer nanostructures.[201] Parallel patterning of complex three-dimensional conjugated polymers has been demonstrated, with the resolution down to sub-50 nm over areas of 500 μm^2 (Figure 2.14C).

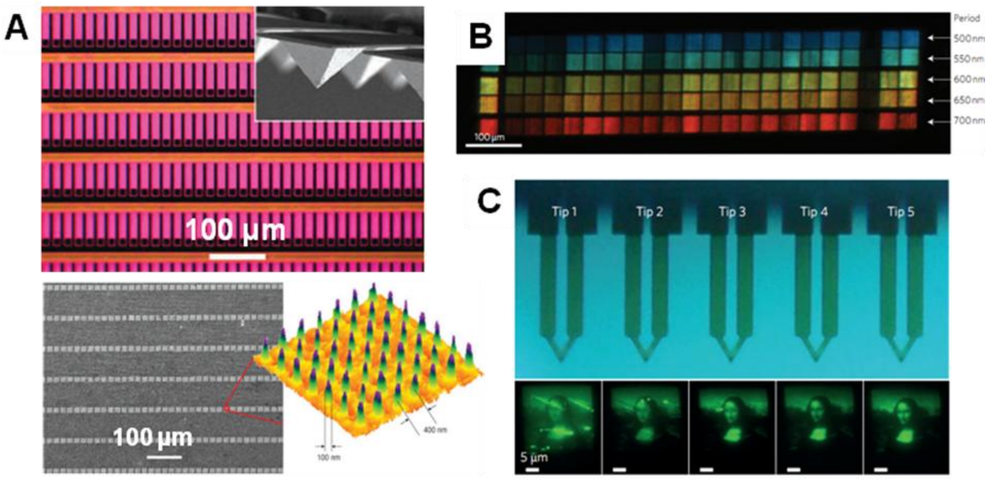

Figure 2.14. Parallel patterning by cantilever array. (A) 2D cantilever array for massively parallel DPN patterning.[193] (B) Optical microscope image of photonic structures consisting of lipid nanopatterns by 1D-array DPN.[195] (C) Parallel thermochemical nanopatterning using an array of five thermal cantilevers and corresponding five fluorescence images of PPV Mona Lisa patterns obtained with the array.[201]

Apart from the extensive use of cantilever-based arrays, a new family of cantilever-free scanning probe array[202] has arisen since the development of polymer pen lithography (PPL)[10] (Figure 2.15A). The polymer pen array consists of a two-dimensional array of elastomeric pyramids with an average tip radius of curvature of 70 ± 10 nm. Because the pen array is made by replica moulding from a silicon master, it is remarkably low-cost and the number of tips in one pen array is highly scalable (Figure 2.15B).[10, 203] The polymer pen array is mounted on the piezoelectric scanner of an AFM to perform massively parallel scanning-probe contact printing. Arbitrary patterns were produced with a speed of ~100 million features per second over 3-inch wafer areas with the smallest feature size reaching 90 nm. Also, PPL has unique time- and force-dependent size flexibility, which allows rapid fabrication across nano- to micro-scale features with the same pen by varying the z-piezo extension (force) (Figure 2.15C and D).[10, 204] The reversible, force-tuned tip deformation also enables patterning gradient features across large area in one writing cycle with size ranging from nano- to micro-scales through intentionally tilting an angle between the pen array and the substrate.[205] Meanwhile, a "force-feedback" leveling technique was developed to achieve highly uniform patterning with a 2% size variation (50 nm) across 1 cm.[206] By taking the inherent advantage of SPL, the polymer pen array can be inked with multiple materials[207-209] or actuated individually[210-211] for multiplexed patterning. Therefore, PPL has become a versatile molecular printing tool for patterning small molecules, polymers, biomolecules etc.,[98, 112, 203, 207-208, 212] and a unique platform to study chemical reactions confined in the nanoreactors.[213-216]

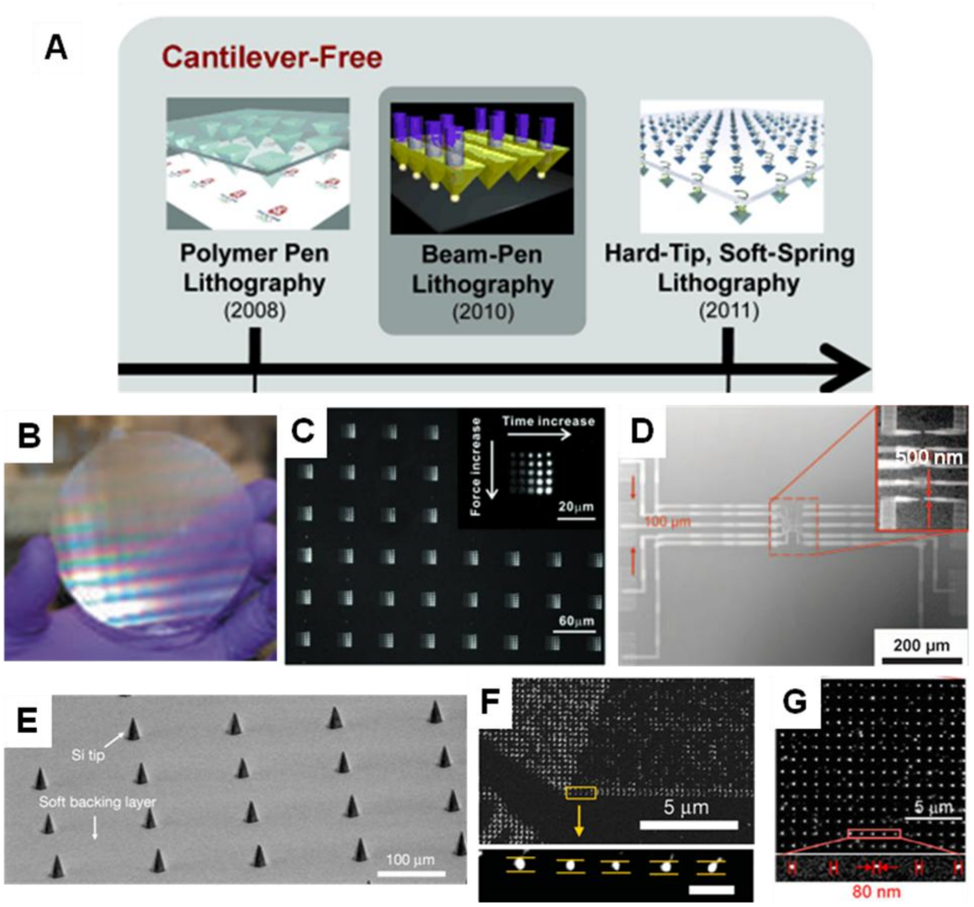

Figure 2.15. Cantilever-free scanning probe arrays. (A) Timeline of development of cantilever-free SPL techniques.[202] (B) Image of polymer pen array over 3-inch wafer areas.[10] (C) Fluorescence image of protein arrays patterned by PPL, with feature size showing time and force dependence.[207] (D) Multiscaled electrode array fabricated by tuning contact force.[10] (E) SEM image of hard Si tip arrays on soft elastomeric support.[217] (F) SEM image of Au patterns composed of sub-50-nm features. Scale bar: 270 nm.[217] (G) Patterned polymer arrays by thermal DPN from graphene-coated Si tip.[218]

To further address the limitations on resolution and uniformity that soft polymer pens suffer from, a hard-tip, soft-spring configuration has been proposed to combine the hard Si tip with the cantilever-free characteristics.[217] Ultrasharp Si tip arrays with a tip size of 22 nm were fabricated with attachment onto an elastomeric backing layer as springs (Figure 2.15E). The Si tip array was employed to conduct parallel DPN at sub-50 nm resolution (Figure 2.15F), while retaining the ability to transfer energy for destructive SPLs. For instance, mechanical indentation, electrochemical desorption and thermal deposition were demonstrated by the Si tip array itself[217] or tips with graphene coating[218] (Figure 2.15G). However, the relatively high cost and complicated fabrication process make it less approachable compared with PPL

On the other hand, a cantilever-free scanning optical lithography technique, namely beam pen lithography (BPL), was developed for mask-free, large-area photopatterning (Figure 2.16).[11] Instead of using microfabrication technique to punch a hole in a silicon-based cantilever in SNOL, BPL forms the pathway to direct light illumination through simply coating the transparent polymer pen array with an opaque metal layer followed by removing the metal layer on the tip end (Figure 2.16A and B). The precise control on aperture size and the distance between the tip and the substrate enable either near- or far-field optical lithography to produce diffraction-unlimited or microsized arbitrary patterns, with the smallest size approaching 100 nm. More recently, by coupling a digital mirror device (DMD) to the BPL system, the light beam through each pen can be controlled to switch and write independent patterns.[219] Applications by exploiting the multiplexed patterning capability have been demonstrated in fabrication of complicated microelectronic components across nano to macro length scales (Figure 2.16C), and device connection in registry with existing nanostructures.

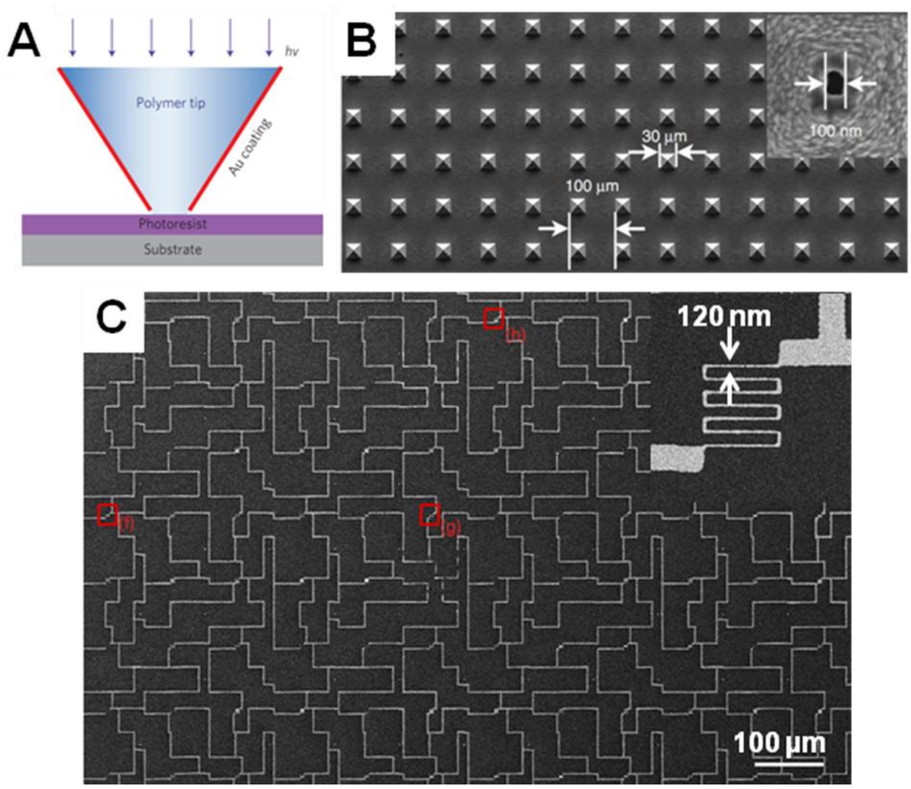

Figure 2.16. Beam pen lithography (BPL). (A) Schematic of BPL principle.[11] (B) SEM image of the BPL pen array with 100-nm aperture.[219] (C) Large-area complex nanostructures generated by active BPL with 96 pens.[219]

2.3 Conclusions and Summary of Research Gaps

From the literature review above, we have shown that SPL is a powerful and low-cost technique with mask-free nanofabrication capability for many functional polymer materials. It can be used to generate mask, mould or templates for other nanopatterning methods. Because SPL typically does not involve complicated fabrication steps, toxic solvents, or strong energy, it is especially suitable for patterning biological materials and some functional polymers that require mild processing conditions. Furthermore, SPL offers unique opportunities to study and control the structures and properties of polymers at the nanometer and even molecule levels. More importantly, the development of parallel SPL techniques using cantilever arrays and cantilever-free tip arrays has made SPL competitive with other lithographic tools with respect to cost, resolution and throughput, although improvements are still required in areas such as patterning efficiency, reliability, and applicability to more systems. The research gaps concerning developing new approaches to pattern functional polymer nanostructures by parallel SPL are summarized in the following:

(1) DPN patterning of polymers is determined by the ink transport and ink-substrate interactions, and control of the DPN process is still challenging. In addition, the applications of the DPN-patterned polymers are still rare.

(2) Although SPL has been reported to create 3D patterns, the throughput is still too low. The large-area, high-throughput 3D patterning by scanning probe arrays has yet been demonstrated, which limits the applications of the 3D patterns.

(3) The polymer pen array has been used for either printing materials or delivering light, thus an approach to combine the two capabilities is desired to extend the applications of polymer pen array.

(4) In an attempt to improve the resolution and uniformity of cantilever-free SPL, the hard-tip, soft-spring lithography shows limitations in tip array fabrication. A simple and low-cost method is thus in demand to fabricate high performance cantilever-free tip array.

CHAPTER 3 METHODOLOGY

In this chapter, the general methodology for the thesis is introduced. The project involves the direct-write patterning of functional polymer materials by 1-D cantilever array, and 2-D polymer pen array (Figure 3.1). Methods for surface modification of substrates and fabrication of polymer pen arrays will be first elaborated. Next, the general procedure for lithography will be described. Finally, the instruments for characterization of the as-made nanostructures will be introduced.

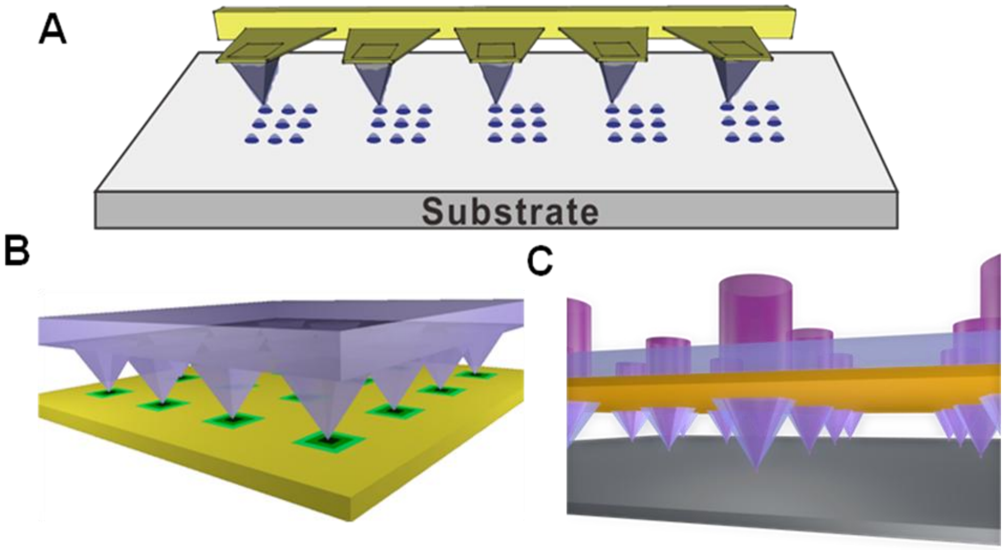

Figure 3.1. Schematic illustrations of parallel dip-pen nanolithography (DPN) (A), polymer pen lithography (PPL) (B) and apertureless beam pen lithography (BPL) (C).

3.1 Materials

3.1.1 Writing pens

1-D cantilever arrays that integrate multiple silicon nitride scanning probes were used to perform parallel dip-pen nanolithography (DPN), including E-type and M-type (Nanoink. Inc.). E-type 1-D array has square-shaped cantilevers with lower spring constant, generally used for contact-mode DPN of molecular inks, while M-type has been designed for high-viscosity liquid inks with high-spring-constant triangular cantilevers. The tips have a nominal tip radius of 15 nm.

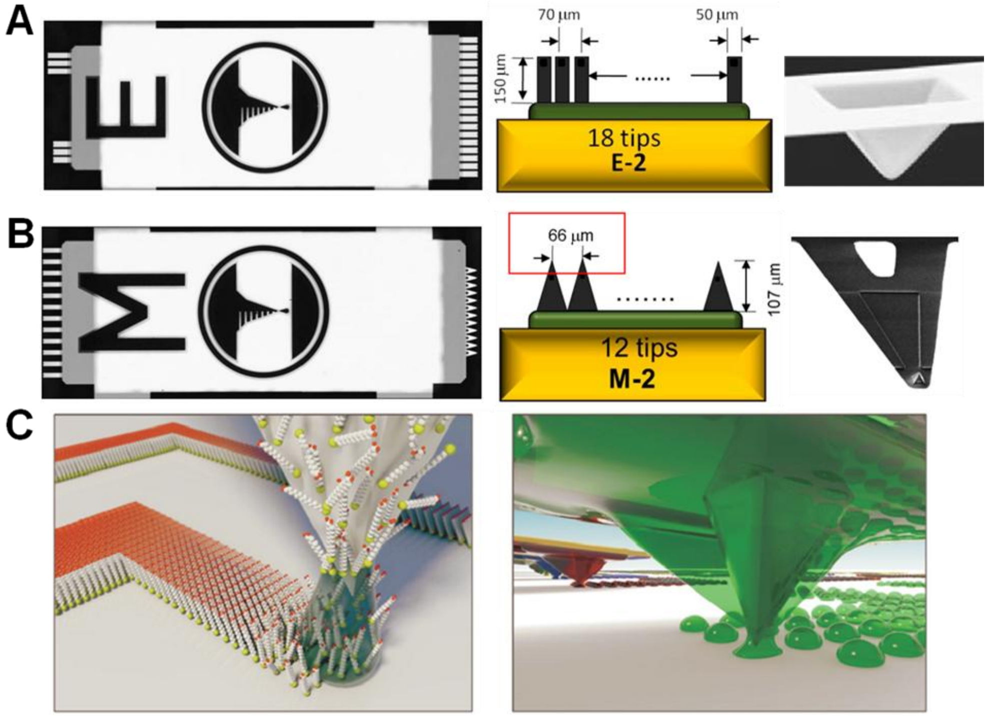

Figure 3.2. 1-D cantilever arrays used for DPN. (A) E-type with square-shaped cantilevers and 18 tips; (B) M-type with triangle-shaped cantilevers and 12 tips. (C) Schematics of printing of molecular ink (left) and liquid ink (right). (Copyright: Nanoink, Inc.)

Table 3.1

Pen	No. of Pens	Pitch (µm)	Spring constant (N/m)
E-2	18	70	0.1
M-2	12	66	2.6

Table 3.1. Parameters of 1-D cantilever arrays.

2-D polymer pen arrays were employed for centimeter-scale patterning by polymer pen lithography (PPL) and beam pen lithography (BPL). The pen array consists of millions of pyramid-shaped elastomeric tips over ~2 × 2 cm^2 area, with a base size of 30-100 µm and a tip-to-tip pitch of 50-500 µm. The commonly used elastomer, hard poly(dimethylsiloxane) (*h*-PDMS, Young's modulus: 8.97 MPa), is prepared by thermal curing from the precursor of vinyl-compound-rich prepolymer (VDT-731, Gelest) and hydrosilane-rich crosslinker (HMS-301). The *h*-PDMS tip can achieve an average tip radius of curvature of 70 nm.[10] Details of fabrication process for polymer pen array are elaborated in Section 3.3. Other polymer materials, such as photocurable elastomers, can be also utilized for fabricating pen arrays.

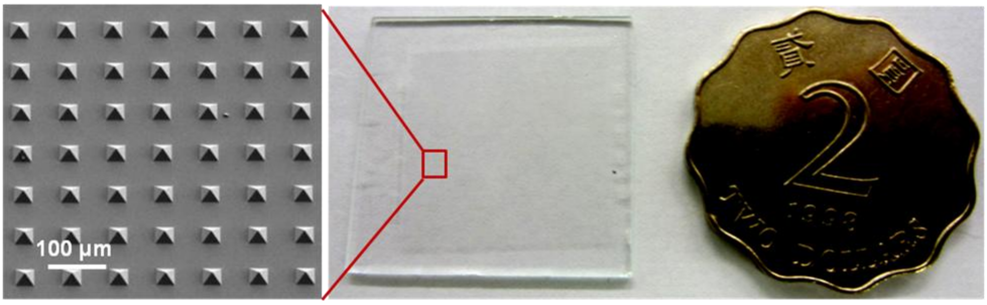

Figure 3.3. 2-D polymer pen arrays for PPL and BPL.

3.1.2 Substrates

N-type single crystalline Si wafers (4", <100>, resistivity 1-10 Ω·cm) with native SiO_2 layer and <1 nm surface roughness were purchased from Semiconductor Wafer, Inc., Taiwan. Silicon wafers with 500 nm SiO_2 on one side were purchased from NOVA ELECTRONIC MATERIALS, LLC., USA. Au substrates were prepared by thermal or electron-beam evaporation of Cr/Au thin films on Si wafers. Poly(ethylene terephthalate) (PET) substrates were supplied by DuPont Teijin Films.

3.1.3 Chemicals

DPN and PPL are capable of printing large libraries of ink molecules. Thiols are model molecular inks for patterning on Au substrates through formation of self-assembled monolayers (SAMs) by Au-S bond. In this thesis, two typical thiol inks were used for printing: 16-mercaptohexadecanoic acid (MHA) and a thiol initiator ω-mercaptoundecyl bromoisobutyrate (MUDBr, synthesized in the laboratory) for surface-initiated atom transfer radical polymerization (SI-ATRP). A second type of ink material is liquid ink, usually high-viscosity liquid or hygroscopic polymers such as poly(ethylene glycol) (PEG). We employed glycerol and PEG with various molecular weight as matrixes to assist the printing of functional materials. In addition, a conjugated polyelectrolyte, cationic poly(thiophene) (PT) derivative PNT (synthesized in the laboratory), was also explored as ink materials because of its good water solubility that facilitates ink transport. For photolithography and BPL, positive-tone photoresist Shipley S1805 (MicroChem Inc.) was utilized.

Substrate surfaces can be modified by SAMs or surface-grafted polymers prior to patterning. Thiol SAMs including MHA, octadecanethiol (ODT) and 11-mercaptoundecyl tri(ethylene glycol) (EG_3) were formed on Au surface. A wide variety of silane coupling agents were adopted for modification of SiO_2 and polymer surfaces to generate rich surface chemistries, e.g. alkyl, alkene, acrylate, fluoro, amine, etc. Polymers were grafted onto the substrates by *in-situ* “grafting from” pre-immobilized reactive sites, providing high-density functional groups such as ionic or epoxy side groups.

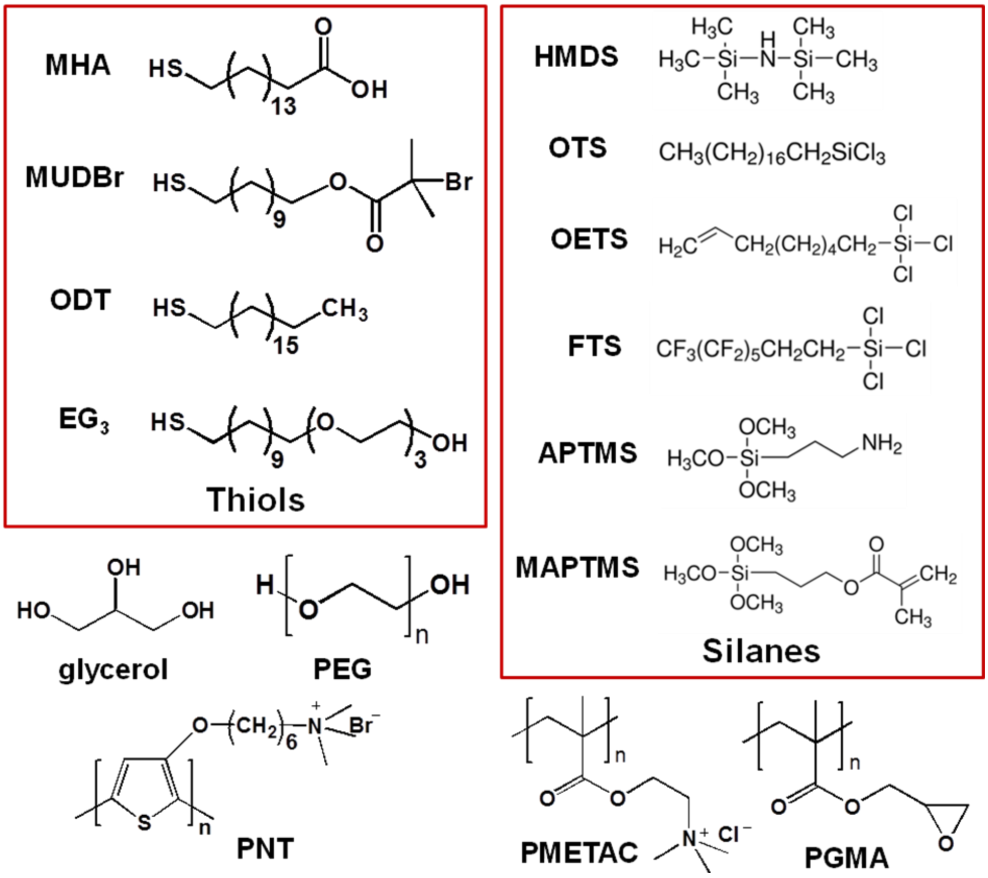

Figure 3.4. Chemical structures of the materials used in the experiments.

3.2 Surface Modification of Substrates

Through the formation of SAM or multi-layers via Au-S or Si-O-Si bonds on the substrates (Figure 3.5), the surface chemistry can be varied with tunable wettability (from hydrophobic to hydrophilic), electrostatic charges (positive or negative) or non-fouling. Furthermore, polymer chains can be grafted onto the substrates by *in-situ* polymerization.

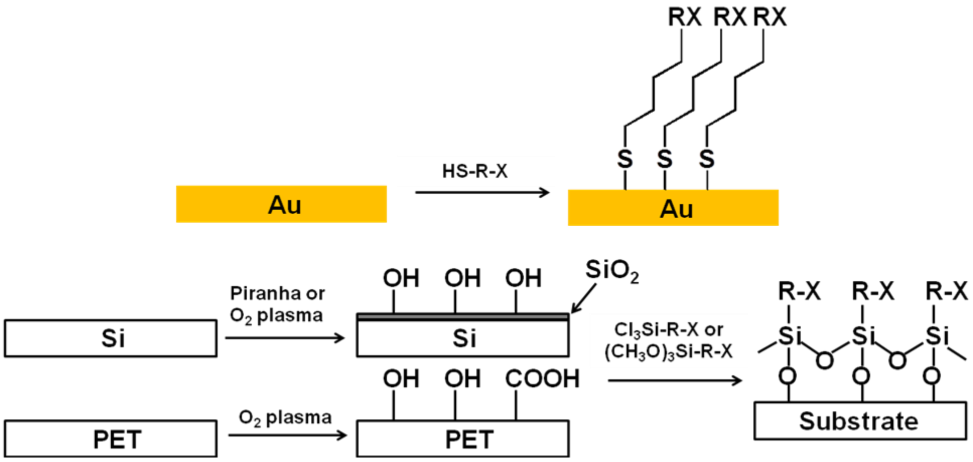

Figure 3.5. Formation of thiol and silane SAMs on the substrates.

Before surface modification, Si wafer was pre-treated with piranha solution (98% H_2SO_4/30% H_2O_2=7/3, v/v) at 80 ℃ for 30 min to generate a hydrophilic and negative charged SiO_2 surface. Alternatively, the Si wafer and PET film were treated with O_2 plasma to render it hydrophilic. Au substrate was sonicated in DI H_2O, acetone and isopropanol sequentially before use.

Vapour phase deposition: The substrate was placed in a closed chamber nearby a container with liquid reagents or solutions (e.g. trichloro-substituted silanes in anhydrous toluene, 1/10 v/v) under vacuum for 2-4 h. Through the evaporation of the molecules, the reaction occurs between the substrate surface and the absorbed molecules.

Solution deposition: The substrate was simply dipped into solutions (5-10 mg/mL) for 0.5-24 h to form SAMs. Thiols were dissolved in pure ethanol solution. For trichloro-substituted silanes, the solvents were chosen as anhydrous toluene or hexane to prevent hydrolysis of silanes. And for trimethoxy-substituted silanes, 95% ethanol solution was used with trace amount of acetic acid (0.5 wt%) added as catalyst. The substrate treated with trimethoxysilanes was further baked at above 100 ℃ for 30 min to obtain cross-linked multi-layers.

Spin coating: Spin coating is a convenient way to form uniform thin films on the surface by spreading the solution and evaporating the solvent under high speed rotation. As in the case of hexamethyldisilazane (HMDS), a 100% solution was spun cast onto a pre-treated Si wafer at 3000 r. p. m for 30s, followed by baking at 100℃ for 5 min to obtain the HMDS-modified substrate.

Surface grafting of polymers: Surface-initiated ATRP and free radical polymerization were employed to graft functional polymers onto the surface. Generally, the substrates modified with reactive sites were immersed into the reactions vessels including monomers and initiators to allow the polymerization proceeding on the surface to form covalent bonding.

3.3 Fabrication of Polymer Pen Arrays

Polymer pen arrays based on *h*-PDMS were fabricated by replica moulding from a Si master.[10, 203] The master with recessed pyramidal microwell patterns was obtained by standard photolithography and isotropic wet etching of single crystalline Si substrate (Figure 3.6).

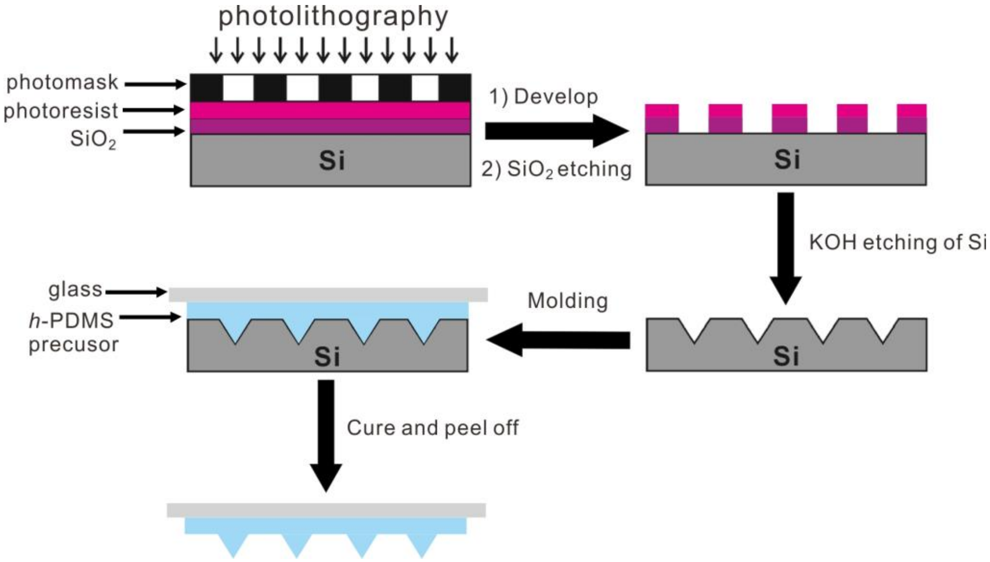

Figure 3.6. Schematic of the major fabrication steps for polymer pen arrays.

Photolithography: In a typical fabrication, a 500 nm thick layer of Shipley S1805 photoresist was spin-coated on a silicon <100> wafer with 500 nm silicon dioxide on one side (NOVA ELECTRONIC MATERIALS, LLC.), followed by soft baking at 115 ˚C for 1 min. Then the resist-coated wafer was exposed to UV light (365 nm, 9 mW/cm^2, 3.6 s) through a chrome photomask using a mask aligner. The exposed photoresist was then developed in Microposit MF-319 developer and washed with DI water.

Wet etching: The substrate was first cleaned by plasma for 1 min, then the exposed SiO_2 layer was etched by immersing in buffered HF solution (Transene Company Inc.) for 5 min. The remained photoresist was washed away with acetone, leaving the underneath SiO_2 patterns. The patterned silicon base was subsequently placed into a KOH etching solution (30% KOH in H_2O : isopropanol = 4:1 v/v) at 75 ˚C for 60 min with vigorous stirring. Due to the anisotropic etching of Si <111> facet, recessed pyramids were formed. A second HF etching was performed to remove the remaining SiO_2.

Surface fluorination: 1H,1H,2H,2H-perfluorooctyltrichlorosilane (Sigma-Aldrich) was used for hydrophobic surface modification of Si master to make the polymer pen array easy to peel off. The silane was dissolved in anhydrous toluene or hexane (1: 10 v/v) and placed in a close chamber near the Si master. The chamber was then kept in vacuum for evaporation of the silane solution and vapour phase reaction for 2-4 h.

Moulding of polymer pen arrays: *h*-PDMS precursor consisting of the vinyl-compound-rich prepolymer (VDT-731, Gelest) and hydrosilane-rich crosslinker (HMS-301) was mixed with a ration of 3.4:1 by weight. The mixture was degassed under vacuum and poured on top of the Si master. A piece of glass slide was placed to cover the precursor as support to ensure uniform pen arrays. The whole was then cured at 80˚C overnight, and the solidified polymer pen array with glass support was carefully separated from the master and cut into pieces for polymer pen lithography experiments.

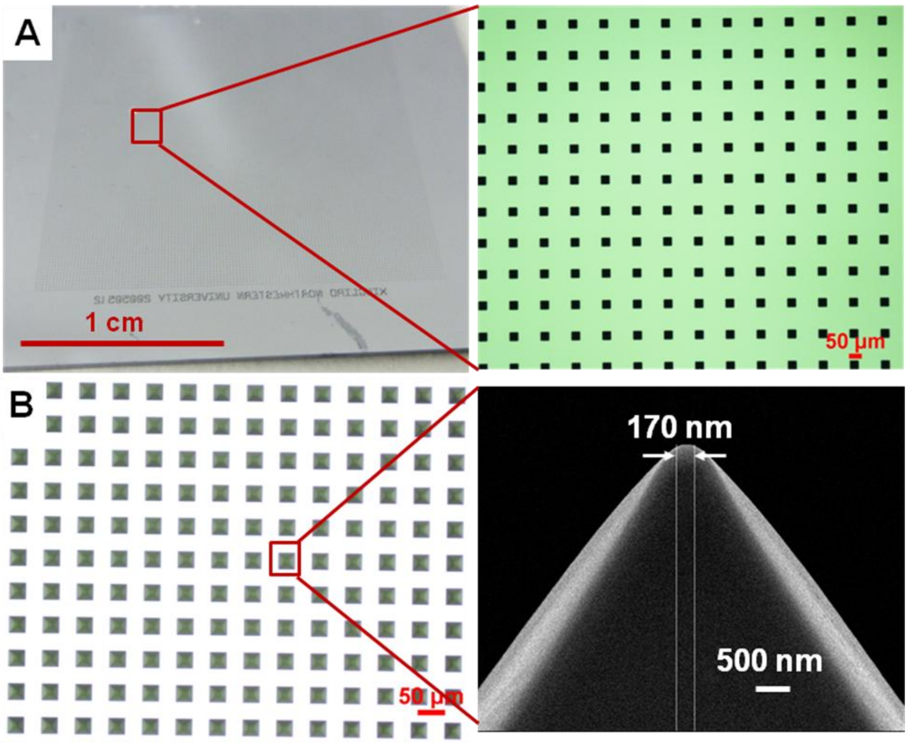

Figure 3.7. (A) Digital photograph of a Si master and the magnified optical image of the fabricated microwells in the Si master. (B) Optical microscope image of the replicated polymer pen arrays and SEM image of a single polymer tip.

3.4 Lithography Process

The main instrument for lithography and imaging of the surface patterns is atomic force microscope (AFM, XE-100, Park Systems), which utilizes a sharp tip to scan the surface at nanometer resolution in all the *x*-*y*-*z* directions. The XE-100 AFM has a unique independent X-Y and Z scanner system that allows the isolation of movements in the *x*-*y* plane and the *z* axis. Under the control of piezoelectric scanner, the tip array moves up and down in the *z* direction, while the sample stage moves in *x* and *y* directions, in which the contact force or z-piezo extension and the *x*-*y* positions are well-controlled with nanometer precision. A built-in tilting stage of XE-100 AFM is used to adjust the sample stage well aligned with either 1-D cantilever array or 2-D polymer pen array. After alignment and approaching with the substrate, the patterning parameters were programmed in the XEP software to perform the lithography, including the pattern design, the applied force or z-piezo extension, dwell time and moving speed, with the whole AFM system encased in a humidity-controlled glove box during patterning (Figure 3.8). The detailed patterning process for DPN, PPL and BPL are included in the followings, respectively.

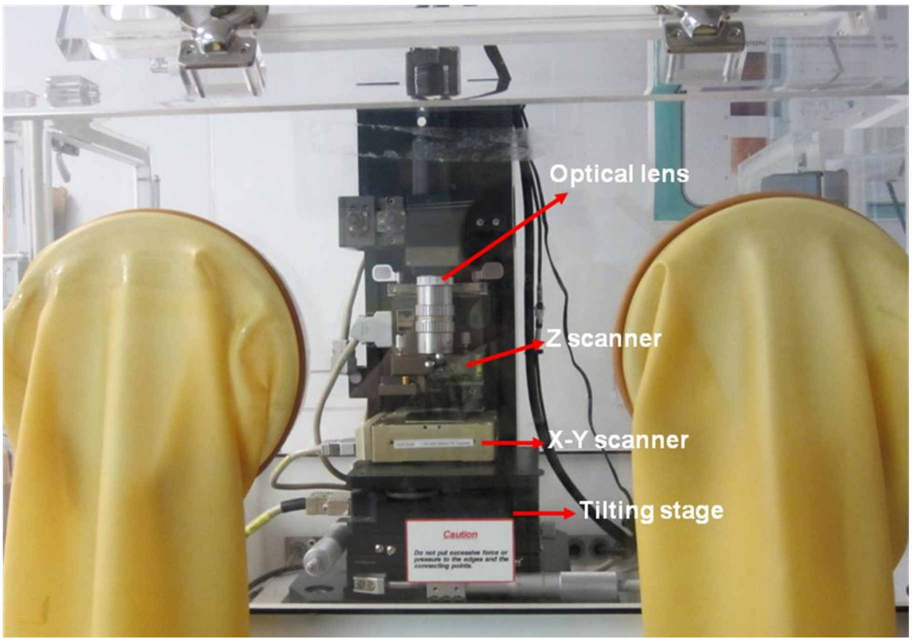

Figure 3.8. Park XE-100 AFM encased in a humidity-controlled glove box.

3.4.1 DPN

1D cantilever array was cleaned with plasma for 1 min (18 W) before use, then the tip array was dipped into the ink solution for 1-5 min and dried in ambient condition. The inked tip array was mounted onto the Z scanner head of AFM (9 μm range) and brought close to the substrate. Since multiple tips are involved in the patterning, it requires an alignment step to ensure all tips are contacted with the substrate simultaneously. The optical microscopy and tilting stage in the AFM system were used to crudely align the plane of the tip array with that of the substrate (Figure 3.9). As the tip at one end of the tip array was moved beyond the contact point with the surface, the bending of the cantilever resulted in strong reflection of light, while other tips maintained weaker reflection, which was used as an indicator for alignment. By adjusting the tilting angle at the *x*-direction, the tips could be well-aligned until all tips showed similar reflection upon contacting. After alignment and setting the approaching state, the tip array was controlled to perform printing with contact force controlled by the laser feedback system. A laser point was positioned on one cantilever (preferably on the central ones) of E-type array to detect the bending degree of cantilever for force feedback in the printing process. However, this laser feedback is ineffective in patterning of liquid inks using M-type array, with the z-piezo extension being monitored instead.

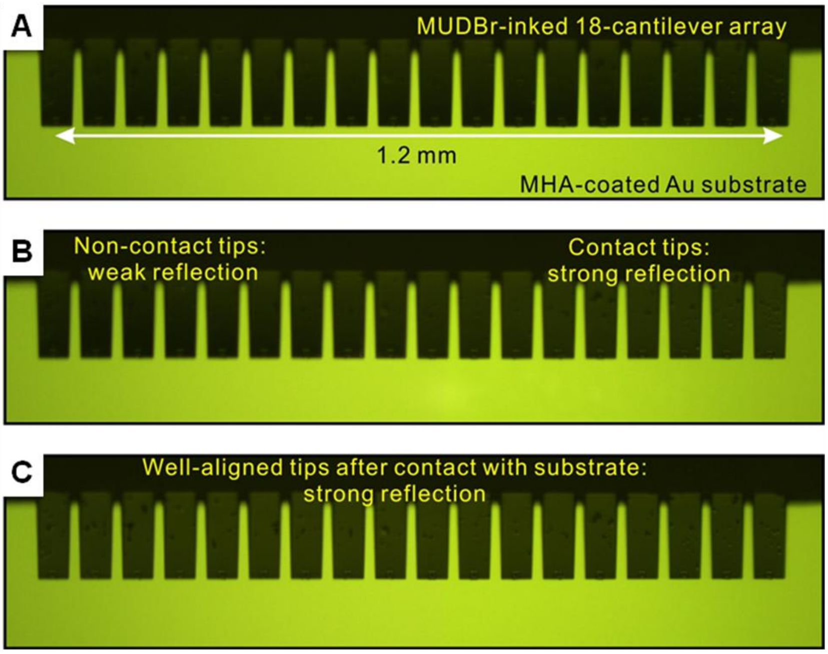

Figure 3.9. Optical images of the inked E-type tip array before (A) and after (B-C) contacting with the MHA-coated Au substrate, where the 18 tips are partially aligned (B) or fully-aligned (C) as confirmed by monitoring the differences of optical reflections of the cantilevers.[138]

3.4.2 PPL

Polymer pen array is first treated with O_2 plasma for 1 min (150 mTorr, 60 W) to render it hydrophilic. Inking was conducted by either drop casting or immersing the pen array in the ink solution, usually suitable for volatile solvents, or spin coating for aqueous or liquid inks. The inked polymer pen array was then mounted onto a 25 μm z-piezo scanner with a 1 × 1 cm^2 aperture for optical leveling. The pen array was then leveled with respect to the substrate plane to enable all tips to contact with the surface uniformly. The relative humidity (RH) in the environmental chamber can be maintained at <10% during the leveling process to avoid undesired material deposition. The pen array was lowered to a few hundred micrometers above the substrate, then the reflected shadows of tips on the substrate were used to measure the relative distance between the pen array and the substrate in the four corner regions. By comparing the distance difference, the substrate stage was tilted in both x and y directions for crude leveling. Next, the tips in the four corners were sequentially brought into contact with the substrate, as verified by the reversible tip deformation, with the z-positions of tips upon contact being compared for precise leveling. The pen array was then withdrawn by a safe distance (~100 μm), and the stage-array misalignment was corrected by changing the tilt angle(s) of the stage. Finally, the variation of tip-substrate distance across 1 cm^2 pen array could be 1-2 μm with ~30 min of leveling time. After leveling, the pen array was programmed to contact with the substrate to write the patterns under controlled humidity. In the case of printing thiols on Au, the printed thiols can be used as resists to Au etching, allowing one to characterize the patterning quality. Au features were generated by immersing the patterned Au substrate in an etching solution consisting of 20 mM thiourea, 30 mM $Fe(NO_3)_3$, 20 mM HCl, 20 mM octanol for 3-5 min (Figure 3.10). After inking, the pen array can be used to write ~1000 patterns or ~3 hrs before the ink is exhausted. For PDMS pen, an overnight ink absorption process under saturated humidity will improve the duration to write patterns for ~12 hrs.

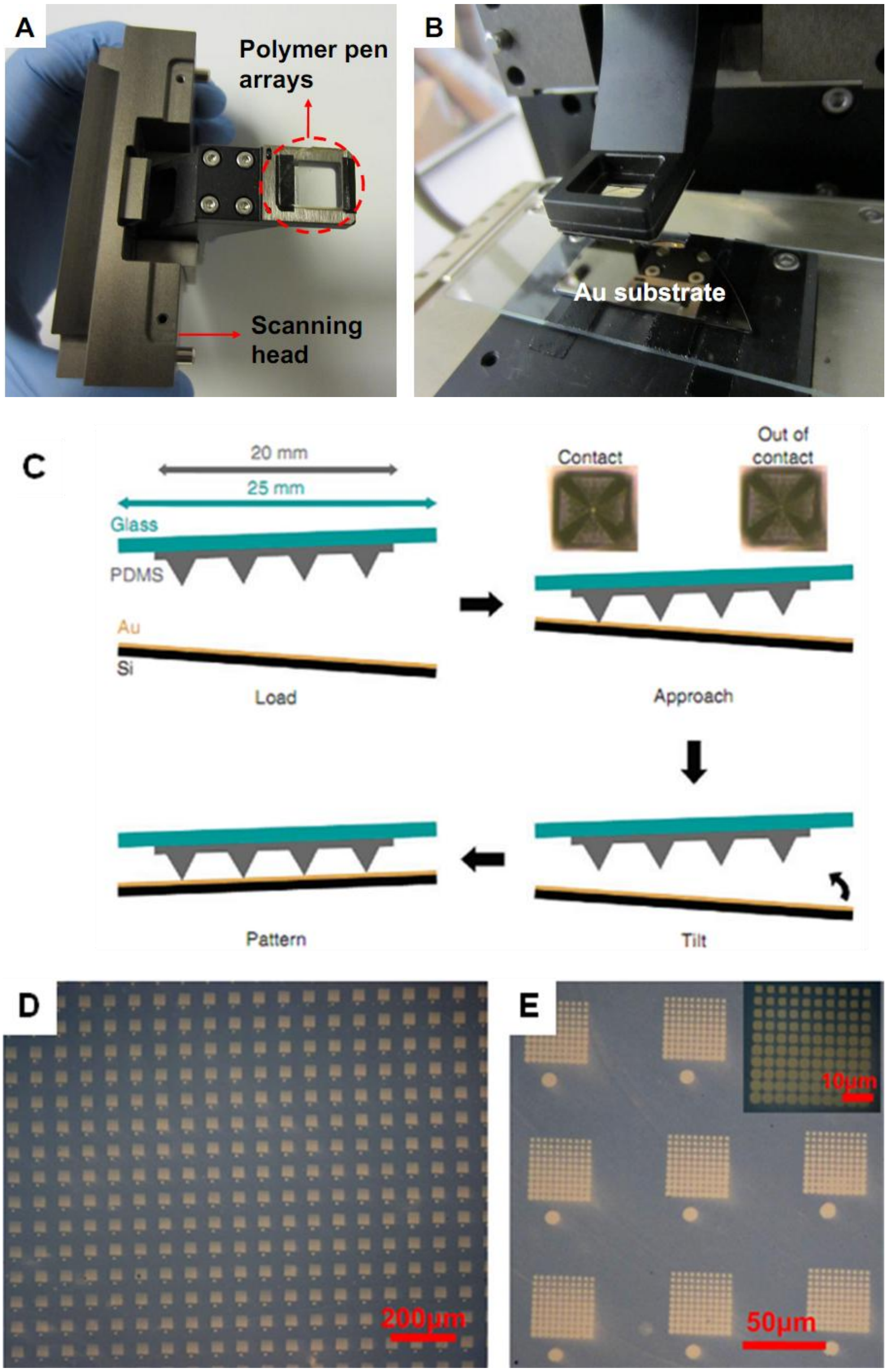

Figure 3.10. PPL process. (A) Polymer pen arrays mounted on AFM scanning head. (B) Z scanner attached to the AFM and aligned to substrate. (C) Schematic of optical leveling of the polymer pen array to a substrate.[203] (D) Optical microscope image of large-area Au dot arrays after PPL patterning of MHA and Au etching; and (E) the magnified images of Au dot arrays.

3.4.3 BPL

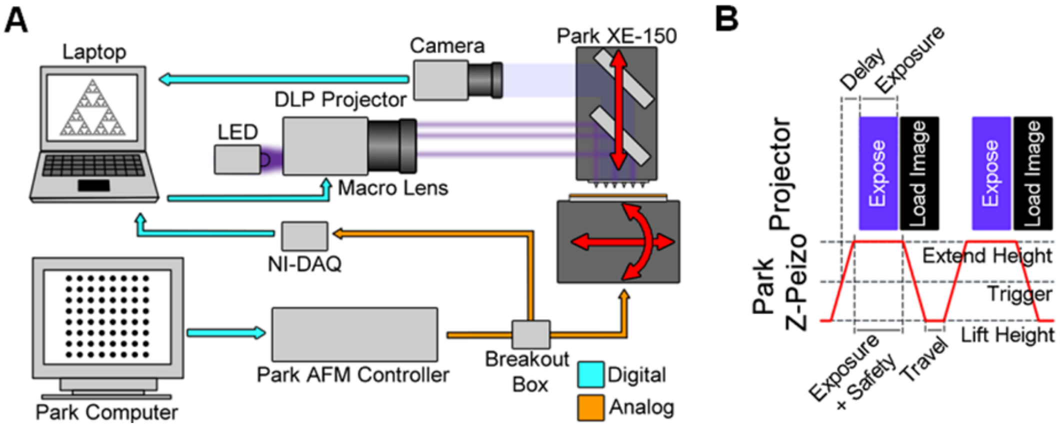

Figure 3.11. Block diagram of the BPL apparatus and the operational cycle.[219]

BPL was performed using a modified photolithography protocol. Typically, a <100> silicon wafer was spin-coated with a 500 nm thick layer of positive photoresist (Shipley1805, MicroChem Inc., USA) at 4000 rpm for 45 s followed by soft-baking on a hot plate at 115˚C for 60 s. For lift-off processing, a layer of lift-off resist (LOR 1A, MicroChem Inc., USA) was spin-coated at 4000 rpm for 45 s and then baked at 180 ˚C for 5 min. Subsequently, the pattern resist was spin-coated using a pre-diluted photoresist solution with propylene glycol monomethyl ether acetate (MicroChem Inc., USA) at 1:1 v/v for 100 nm thick layers and 1:3 v/v for 40 nm thick layers. BPL pen arrays were mounted onto a BPL apparatus based on a scanning probe platform (XE150, Park Systems) and leveled to the photoresist-coated substrates using the same method as PPL. Patterns were generated under the control of piezoelectric actuators and a commercial digital micromirror device (DMD, DLP LightCommander, Logic PD) coupled with a collimated 440 mW 405 nm LED light source (M405L2, Thor Labs USA) to allow the exposure time between 1 and 10 s. After patterning, the photoresist was developed in MF24A (MicroChem Inc. USA) for 20-30 s and rinsed with DI water. A layer of 2 nm Cr and 10 nm Au was evaporated onto the developed samples followed by etching of polymer resist in Remover PG

(MicroChem Inc., USA) overnight. Patterns of photoresist and metals were characterized using optical microscopy (Axiovert-Zeiss), AFM (Dimension Icon, Bruker), and SEM (S-4800-II, Hitachi).

3.5 Characterization

3.5.1 Atomic Force Microscopy (AFM)

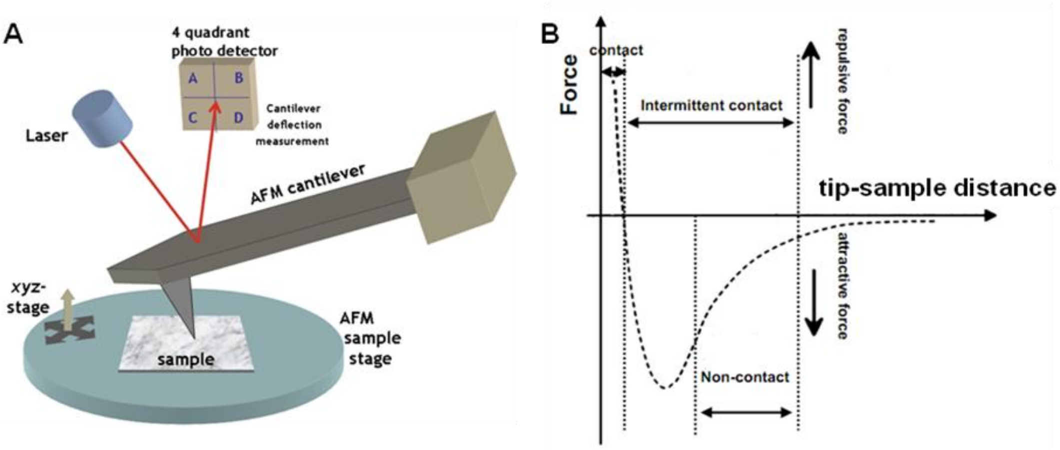

Figure 3.12. (A) Principle of AFM. (B) Van der Waals force as a function of tip-sample distance.

An atomic force microscope employs an ultrasharp tip (<10 nm) mounted on the end of a microscale cantilever spring to record surface information in the three dimensions based on tip-surface interactions by raster scanning. To image the surface topography, the deflection of the cantilever is measured by an optic deflection sensor composed of a laser beam reflected by the cantilever backside and a position-sensitive photodetector to receive the laser signal (Figure 3.12A). Before imaging, the position value is set to approach zero, and the position change of the laser spot indicates the angular deflection of the cantilever as well as the surface profile. The imaging mode of AFM is based on the Van der Waals force between the tip and the sample, which changes as a function of tip-sample distance (Figure 3.12B). In contact mode where the tip keeps contact with the sample surface under a certain force, the tip-sample interaction is repulsive and both vertical and lateral deflection of the cantilever are recorded, corresponding to topography and lateral force microscopy (LFM) images. The latter one is useful in the differentiation of the surface containing chemical materials with different frictional properties. On the other hand, the Van der Waals force becomes attractive with increasing distance, and AFM working in this region is on non-contact mode or tapping mode. An oscillated tip at the resonance frequency with constant amplitude is moved near the surface. The variation in attractive force due to change in tip-sample distance will cause shift of the vibrating frequency, reflecting the surface profile without damaging the sample. Moreover, tapping mode is most frequently adopted by taking advantages of both contact and non-contact imaging. It works with intermittent contacting to eliminate frictional forces by the surface, while the oscillation with sufficient amplitude avoids tip trapping or adhesion by the surface contaminant layer. By monitoring the phase lag between the signal that drives the cantilever to oscillate and the cantilever oscillation output signal in tapping mode, the variation in surface properties such as elasticity, adhesion and friction can be also mapped by phase imaging.

3.5.2 Field Emission Scanning Electron Microscopy (FESEM)

FESEM is used to characterize surface morphology at a resolution as high as 1-2 nm. Under high vacuum, a field-emission cathode can generate narrow electron beam, which is accelerated in a field gradient and focused through electromagnetic lenses before reaching the sample surface. The interactions between the electron beam and the specimen result in different types of electrons emitted from the specimen. The most common imaging mode utilizes a detector collecting electrons with energy below 50 eV, also known as secondary electrons. These electrons are ejected from the K-shell of specimen atom by inelastic scattering with primary beam. The emission is highly related to surface topography that only the electrons near surface (<10 nm) can overcome the energy barrier and be ejected. Therefore, the difference in collection efficiency of secondary electrons caused by the topography change can be used to reconstruct the surface image in high resolution. Another important emission is X-ray from interaction with high energy beam, which contributes to elemental analysis by energy-dispersive X-ray spectroscopy (EDX). When an electron in the inner shell of the specimen atom is excited and ejected from the shell, the vacancy left in the shell can be occupied by an electron from the outer high-energy shell with energy release in the form of X-ray. The intensity and energy of the emitted X-rays can be measured by an energy-dispersive spectrometer, and each element has its own characteristic energy, allowing analysis of element composition.

3.5.3 Optical Microscopy

The surface patterns can be observed from optical microscope by bright-field, dark-field or fluorescence microscopy. Bright-field microscopy uses the transmitted light on the sample while dark-field takes advantages of scattering light. Fluorescent molecules are also useful probes for imaging surface patterns by fluorescence emission under lamp illumination. Fluorescence is separated from excitation light by a dichroic mirror and appropriate filters: excitation light is reflected back into the objective while fluorescence is transmitted. For example, in Nikon Eclipse 80i optical microscope, the channels used are: λ_{ex} = 465–495 nm, λ_{em} = 515–555 nm for green fluorescence; λ_{ex} = 528–553 nm, λ_{em} = 577-632 nm for red fluorescence.

3.5.4 Attentuated Total Reflectance Fourier Transform Infrared Spectroscopy (ATR-FTIR)

The chemical composition of a thin film on the surface can be analyzed by

ATR-FTIR. This reflective technique is operated by locating the sample surface to face a crystal surface and measuring the changes that occur in a totally internally reflected infrared beam passing through the crystal and contact with the sample surface. IR spectrum is obtained after the sample absorption. The technique can be used to identify either SAMs or polymers on the surface.

CHAPTER 4

DIRECT PRINTING OF POLYMER MATERIALS

In this chapter, direct printing of polymer materials by scanning probe arrays is first investigated. Two typical polymer inks were studied here, including polyelectrolytes and liquid-like hygroscopic polymer inks. The ink transport was systematically investigated and the application of liquid polymer ink as delivery matrix was demonstrated.

4.1 Introduction

Most of the materials that can be deposited from AFM tip by DPN are water-soluble since DPN printing of molecules relies on the water meniscus formed between the tip and the substrate as a media. Polyelectrolytes are important water-soluble polymer materials and thus they can be the major candidates for DPN. It has been reported that conducting polymers with ionic side groups and several commonly used polyelectrolytes can be nanopatterned by DPN driven by electrostatic attraction with charged surface.[83] And these polymers have shown similar ink diffusion properties like small molecules. However, whether the patterning of polyelectrolytes by DPN or PPL can be conducted on neutral substrates is unclear. Thus we conducted studies on the ink transport of a fluorescent conjugated polyelectrolyte PNT by single tip or parallel tip arrays onto various neutral substrates.

In recent studies, another type of ink has been extensively used for DPN, that is, liquid ink. Different from molecular inks, the transport of liquid ink is less dependent on water meniscus and the feature size is determined by various parameters including the dwell time, ink viscosity, capillary bridge and surface energy of substrate. Because liquid polymer inks allow ink deposition in bulk instead of molecular monolayer, they have been found wide range applications as polymer resists, cargo matrixes for functional materials and microlenses. Particularly, hygroscopic polymer poly(ethylene glycol) (PEG) has attracted much attentions due to its excellent solubility, chemical inertness, biocompatibility, and versatility. PEG has been utilized as matrix to enhance the delivery of many nanomaterials and biomacromolecules that are difficult to diffuse from an AFM tip. Moreover, the use of polymer matrix can tune the ink transport rate to print uniform features. However, the immobilization of the delivered materials on the substrate remains a major concern. To address it, we explored a combined approach to use PEG as a delivering matrix and the surface-grafted polymer as a receiving matrix for site-selective printing and immobilization of catalysts through which metal structures could be formed on flexible substrates.

4.2 DPN and PPL of Cationic Polythiophene PNT

4.2.1 DPN of PNT on Various Substrates

PNT is a polythiophene derivative with a quaternary ammonium pendant group attached to the polythiophene backbone (see chemical structure in Figure 4.1A, kindly provided by Prof. Shu Wang, CAS). The yellow solid of PNT is highly soluble in water or alcohols to form dark red solution at concentration>1 mg/mL, which turns to yellow after dilution. For DPN printing, the ink solution was prepared by dissolve PNT in H_2O: methanol (1:3 v/v) at 1 mg/mL. The DPN substrates without surface charges were chosen as Au, Si wafers with native SiO_2 and modified with hexamethyldisilazane (HMDS) or octadecyltrichlorosilane (OTS).

First of all, we examined DPN of PNT on Au surface. A contact-mode AFM tip was dipped in PNT ink solution and dried in air. The inked tip was contacted with Au surface at 1 nN, in an environment of 70%-90% relative humidity (RH). The tip was controlled to move on the surface with varied writing speed to draw lines, while it remained in a location at programmed dwell times to form dot features. The patterns were immediately characterized in contact mode using the same writing tip after writing. Seen from the lateral force microscopy (LFM) image in Figure 4.1B, PNT nanolines (100-340nm line width) were generated with the writing speed of 0.01, 0.02, 0.04 and 0.06 μm/s on Au surface. The linewidth increases and the intensity becomes denser as the writing speed slows down, indicating more ink deposition. The ink diffusion property was further investigated through the obtained dot arrays with controlled dwell time (Figure 4.1C). In DPN process, the growth of dot size D with contact time t exhibits the form of $D=b+kt^{1/2}$, where k is the parameter related to diffusion rate at a certain condition and b corresponds to tip/meniscus size parameter.[74] The patterned PNT dot array fitted well with the linear relationship of $D \sim t^{1/2}$. Unlike DPN of thiols on Au, the dot feature was not formed at a short dwell time, which can be attributed to a slow dissolution process of PNT molecules in the water meniscus prior to molecular diffusion onto the surface via Van der Waals force. However, no topography information was observed due to the insufficient ink transport. It is suggested that only a monolayer of polymer chains randomly laid on the surface is formed by DPN according to previous reports.

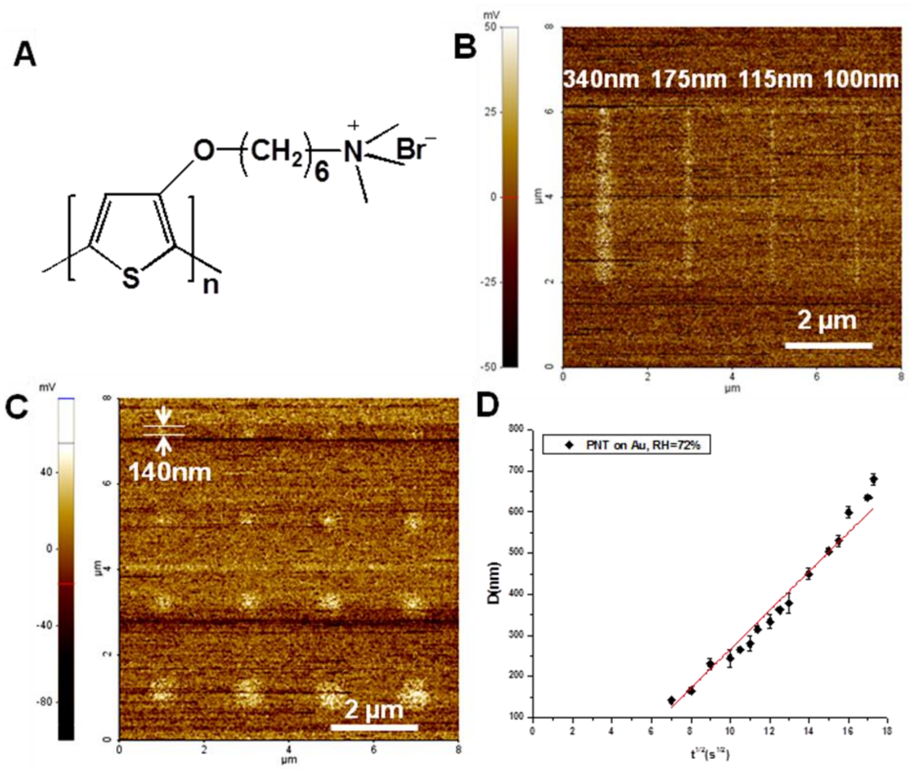

Figure 4.1. (A) Chemical structure of PNT. (B) Lateral force microscope (LFM) image of PNT nanolines written on Au, with writing speed of 0.01, 0.02, 0.04, 0.06 μm/s from left to right. (C) LFM image of PNT nanodot array on Au with dwell time from 49 s to 300 s. (D) Plot of dot diameter with square root of dwell time ($t^{1/2}$) with linear fitting.

The DPN printing of PNT was found to be facilitated on native SiO_2 surface. Because the molecular diffusion is mediated by water meniscus and interactions between ink molecules and substrate, a hydrophilic surface would promote meniscus formation as well as ink transport. After ultrasonic washing with organic solvents, the SiO_2 surface (contact angle < 30°) is more hydrophilic than Au (contact angle: 50°-60°). As a result, PNT was found to deposit on SiO_2 surface by E-type 1-D cantilever array under 40-50% RH with writing speed of 0.1, 0.2, 1, and 2 μm/s, much faster than that on Au (Figure 4.2A). The linewidth was found to maintain as 200-250 nm and the height ranged from 0.5-1 nm. The results indicate improved ink transport, but still the diffusion of PNT on SiO_2 surface is slow. On silane-modified HMDS-SiO_2 (contact angle: ~78°), PNT was deposited at 5 nN under 95% RH and writing speed ranging from 0.01 to 0.06

µm/s (Figure 4.2B). A constant linewidth of ~150 nm was also presented. However, PNT cannot be deposited on OTS-SiO_2 surfaces with typical contact angles of ~100°. The increased hydrophobicity can significantly hinder the molecular diffusion through water meniscus even in highly humid (>95%RH) environment. By applying additional force to scratch away the surface molecular layer while conducting DPN, it was found that highly confined PNT patterns can be written without ink diffusion to the surrounding areas. Dot and line arrays were patterned on HMDS-SiO_2 at 90%RH by M-type 1-D cantilever array with z-piezo extension > 0.5 µm (corresponding to force >1000 nN). The as-made features show height of 1-3 nm and lateral size of ~100 nm for lines and ~50 nm for dots. The written dots were found to be stretched to ~200 nm length in one direction due to the sliding of tip under large z-piezo extensions. Similar phenomenon has also been observed in dip-pen nanodisplacement lithography (DNL) in which an initiator molecule is written on a thiol SAM-protected Au substrate with simultaneously tip scratching and ink deposition. Patterns of polymer brushes also present this kind of trail when grown from the patterned initiator moieties.

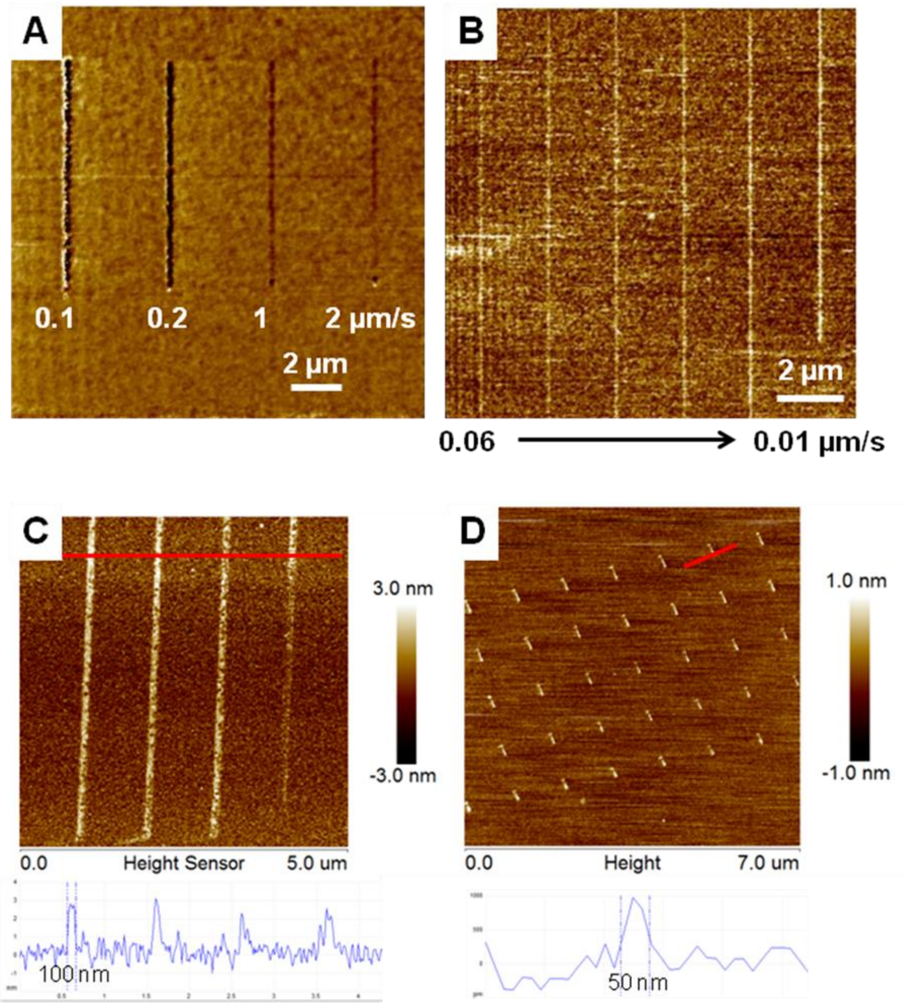

Figure 4.2. (A&B) LFM images of PNT nanolines written by E-type tip array on SiO_2(A) and HMDS-SiO_2(B). (C&D) Tapping-mode AFM images of PNT nanolines (C) and nanodots (D) written by M-type tip array on HMDS-SiO_2.

4.2.2 DPN of PNT Assisted with Additives

One of the most important properties of PNT is the highly efficient fluorescence. PNT shows yellow fluorescence (λ_{ex} = 420 nm, λ_{em} = 570 nm) in aqueous solution as reported in the literature,[220] and the spin casted film is observed to emit strong green fluorescence under blue light excitation and weaker red fluorescence under green light excitation. However, the DPN-generated PNT nanopatterns cannot show optical or electronic performance due to the molecular deposition with thickness of only a few nanometers. To improve ink transport, inspired by the previous studies on DPN assisted by surfactant[221] or liquid matrix[98], we found that a small amount of additives added to the ink solution e.g., glycerol and PEG, could facilitate the transfer of PNT onto substrate, resulting in patterned nanostructures with considerable thickness. In these cases, the ink transport did not comply with molecular diffusion but more like liquid ink.

First we investigated the function of glycerol as a liquid matrix, which was added to the 1 mg/mL PNT aqueous solution with a concentration of 10 mg/mL. The M-type 1-D cantilever array was then used to deposit the ink mixture onto HMDS-SiO_2. Dot arrays were generated under 55%RH and 0.5-10 s dwell time, which was the normal condition for printing glycerol. The patterned dot arrays were clearly observed from optical and fluorescence microscopy. Both green and red fluorescence could be easily seen in the exposure time range of 1-10 s, with the intensity of the green emission showing 2 to 3 folds greater than the red one (Figure 4.3A). Tapping-mode AFM topography image shows that the dots in the 10×10 array with 0.5 s dwell time have an average diameter of 442 ± 38 nm with the height of 70-80 nm (Figure 4.3B). These results confirm the effectiveness of glycerol matrix to greatly increase the amount of PNT to be delivered onto the substrate.

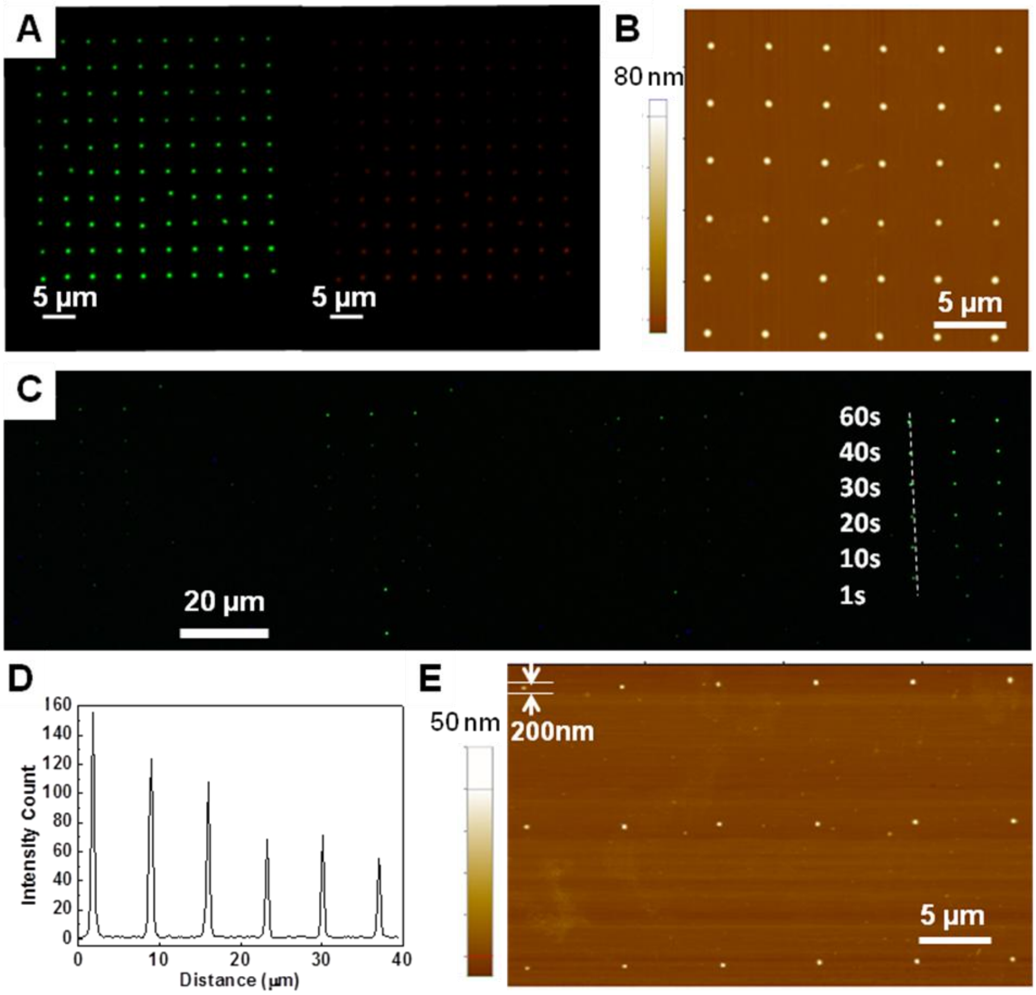

Figure 4.3. (A) Fluorescence microscope images of dot arrays by DPN patterning of PNT/glycerol (1:10 w/w). (B) Tapping-mode AFM topography image of the array shown in (A). (C) Fluorescence microscope images of parallel dot arrays generated from PNT/glycerol (5:1 w/w) ink. (D) Intensity count of dots with varied dwell time, as indicated in (C). (E) Tapping-mode AFM topography image of one array shown in (C).

Interestingly, PNT nanoarrays could also be fabricated by adding a small amount of glycerol. In this case, glycerol would function as surfactant to promote the dissolution of PNT in water as well as water absorbent to create liquid-like ink on the tip end. Reliable DPN results were obtained with the glycerol ratio as low as 1/5 w/w to PNT (1 mg/mL) under 60%-95%RH. PNT dot array was repeatedly written on HMDS-coated Si wafer for 5-6 cycles by M-type cantilever array at 85-95%RH with dwell time ranging from 1 to 60 s.

Also, lines were drawn with varying tip speed from 0.2 to 2 µm/s. The 6 × 3 dot arrays fabricated at the first 3-4 cycles were distinctly observed from optical and fluorescence microscope, as shown in Figure 1. All the tips were shown to pattern the dot arrays. The tapping mode AFM characterization of the fabricated dots shows that the dot has a diameter of 310-370 nm and a height of 44-65 nm in the array with stronger fluorescence, while in the array that had only 1/10 fluorescence intensity, the diameter and the height decrease to 190-270 nm and 35-55 nm (Figure 4.3C), respectively. There is a slight increase in diameter and height with the longer dwell time, however, the effect of dwell time can be negligible compared with conventional DPN, which indicates the characteristic of liquid ink deposition. The patterned dot arrays were difficult to observe in optical microscopy after 5 printing cycles, indicating that the ink was exhausted on the tip. Through AFM characterization, such arrays with decreased ink amount were found to have typical dot diameter of 100-120 nm and height of 12-16 nm, and the smallest dot can be 65 nm in size with ~ 10 nm height (Figure 2B). The height-to-diameter ratio in all the cases are almost the same, being 1/5~1/6. Nevertheless, the as-made lines were only 1-2 nm thick with the line width of ~100 nm (Figure 2C).

Similarly, dot arrays were also generated using PNT/PEG mixtures. PNT dots were printed in the presence of 1/10 w/w PEG (Mw=2000) to PNT (Figure 4.4). The dot arrays, which can be observed by optical microscopy, show distinct green fluorescence with a high signal-to-noise ratio up to 60, however, red fluorescence fails to be observed. Furthermore, the smallest size of the patterned dots as measured by tapping mode AFM could reach 140 nm with a height of 30 nm. However, in some cases, the fabricated dots only show very weak fluorescence, indicating non-uniform transfer of PNT along with the PEG.

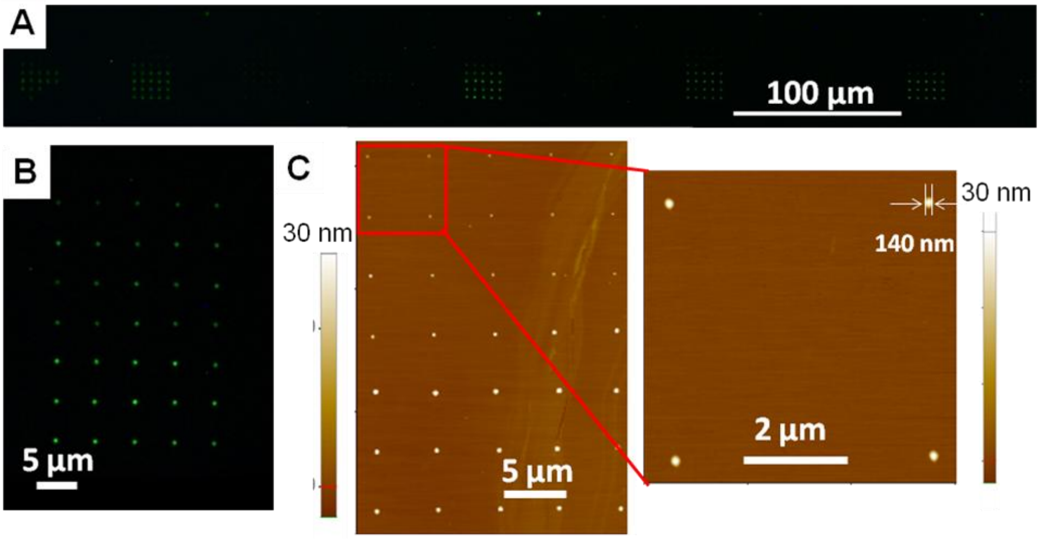

Figure 4.4. (A) Fluorescence microscope images of dot arrays by DPN patterning of PNT/PEG2000 (10:1 w/w). (B) Magnified fluorescence image of one array shown in (A). (C) Tapping-mode AFM topography image of the array shown in (B).

In brief, we demonstrated the successful generation of fluorescent nanoarrays composed of conjugated polyelectrolytes, which may have potential applications in optoelectronics and biosensors. However, since the presence of surfactants can affect the optical and electronic performance, method to pattern PNT without additives is still desirable.

4.2.3 PPL of PNT

In this section, we investigated the performance of 2-D polymer pen arrays to pattern PNT inks. Different from Si-based AFM tips, polymer pen arrays consist of elastomeric PDMS tips that have excellent permeable property to improve ink absorption and reversible tip deformation to toggle the feature size. Therefore, the polymer pen is expected to deliver more ink materials than Si tip in the absence of surfactant or matrix. To test the hypothesis, the polymer pen array was inked with aqueous PNT ink (1 mg/mL) by drop casting, and PPL was performed on HMDS-SiO_2 surface with varied dwell time (*t*) and Z-piezo extension (Z_{ext}) under 90%RH. The polymer pen array was observed to maintain wet during the patterning, with the deposited PNT ink on the substrate forming liquid-like droplets as observed from optical microscope. To investigate the time- and force-dependence properties of PPL, a 8 × 8 array (pitch = 3 µm) was written with dwell time of 0.5 to 6 s and Z_{ext} of 2 µm, together with a 7 × 7 array (pitch = 4 µm) with increasing Z_{ext} from 0 to 6 µm and dwell time of 1 s. Both arrays were seen from optical and fluorescence microscope, however, only partial pens succeeded in printing due to the non-uniform inking from drop casting. Tapping mode AFM was used to characterize the patterned structures. The dot diameter and height increased as increasing dwell time, however, the increasing rate slowed down at longer dwell time, which can be attributed to insufficient ink supplement from the bulk to the surface of polymer pen. We observed an increase in size and height of patterned dots with increasing Z_{ext}, with the volume of the dot features shows a linear function of Z_{ext}. Nevertheless, the dot size at Z_{ext} of 6 µm only reached ~1 µm, which was much smaller than the deformed tip area (~ 3 µm). This can be attributed to the dewetting of PNT ink on the hydrophobic HMDS surface, which leads to a ring surrounding the patterned dots corresponding to the contact area of deformed tip, as confirmed by phase images. Therefore, features smaller than the tip contact area could be generated even when large tip deformation occurs, and features as small as 140 nm were obtained by the deformed tips. These results suggest that PNT can be printed in a liquid deposition manner by PPL with time- and force-controlled ink transport. In addition, the dewetting of polymer ink on a hydrophobic surface can be used to generate features smaller than the tip contact area for high-resolution patterning.

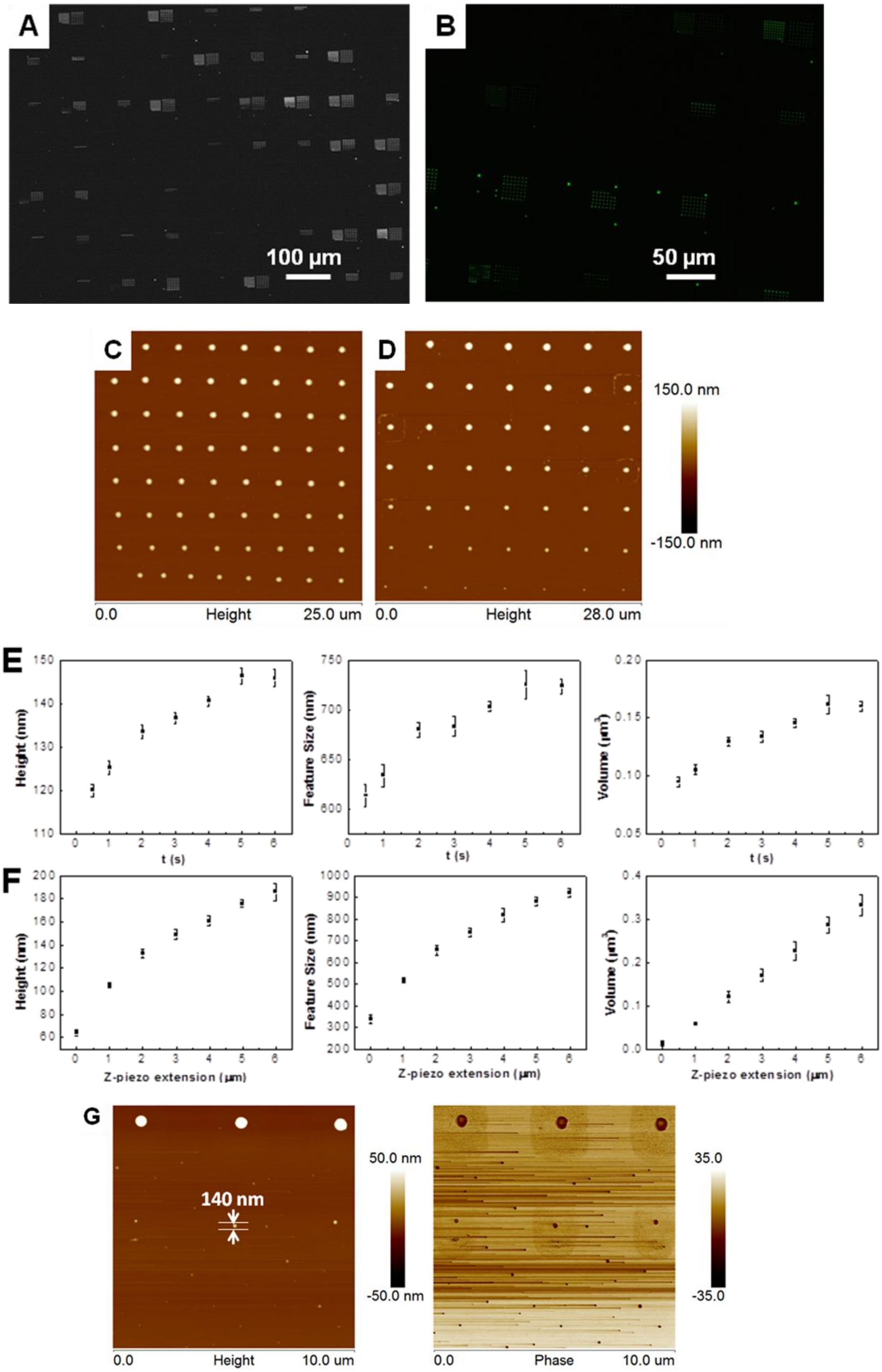

Figure 4.5. (A) Dark-field and (B) fluorescence microscope images of PNT dot

arrays patterned by PPL. (C&D) Tapping-mode AFM images of dot array printed by one tip with varied dwell time (C) and contact force (D). (E&F) Plots of height, feature size and dot volume versus dwell time (E) and z-piezo extension (F). (G) Magnified tapping-mode AFM topography and phase images of one array, showing dot with feature size of 140 nm and halos around the dots in the phase image.

4.2.3 Summary

To conclude, direct printing of the conjugated polyelectrolyte PNT by DPN and PPL was demonstrated to fabricate molecular nanopatterns as well as fluorescent nanoarrays. We demonstrated that PNT could be deposited onto various neutral substrates by DPN through meniscus-mediated molecular diffusion, in which the ink transport was determined by surface energy of the substrates. Also, we found that PNT could be patterned as liquid ink in the presence of small amount of hygroscopic additives or by printing with polymer pen arrays. These observations establish the foundation for direct-write fabrication of functional polyelectrolyte nanostructures for guided phase separation or device integrations.

4.3 DPN of Liquid Matrix for Matrix-Assisted Catalytic Printing

In previous section, we have shown the function of liquid glycerol and PEG ink to aid the printing of polyelectrolytes. However, usually it is necessary to remove the liquid matrix after printing while maintaining the functional materials. Previous approaches have used reactive SAMs on the surface to immobilize the deposited molecules, but the capture density is limited.[105] To improve the immobilization efficiency, here we developed a combined approach with the employment of a surface-grafted polymer layer as a receiving matrix[222] in addition to the PEG delivering matrix. As proof-of-concept, we demonstrated scanning probe printing and immobilization of catalytic salts assisted by the two matrixes. Owing to DPN and the high-density loading sites in polymer receiving matrix, high-resolution and robust metal patterns were produced by electroless deposition (ELD)[223] on the catalyst-immobilized areas.

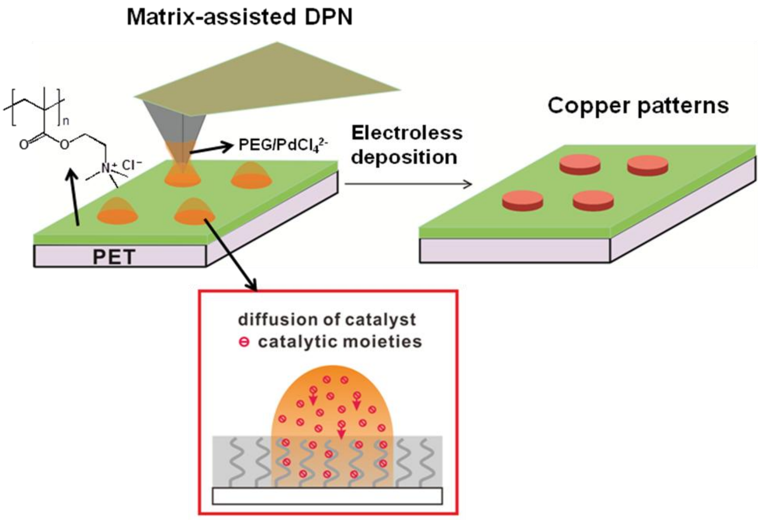

Figure 4.6. Schematic illustration of matrix-assisted catalytic scanning probe printing.

4.3.1 Experimental

Poly(ethylene terephthalate) (PET) films (thickness of 175 µm) were supplied by DuPont Company. For surface grafting of polymers on the PET surface, the substrates were exposed to O_2 plasma followed by immersing in an ethanol solution containing [3-(methacryloyloxy)propyl]trimethoxysilane (MAPTMS) (1 wt.%) for 1 h. Then the substrates were baked at 120 ^{o}C for 30 min. Next, the substrates modified with methacrylate group were placed in an aqueous solution of 2-(methacryloyloxy)ethyl-trimethylammonium chloride (METAC, 20 wt.%) and potassium peroxodisulfate (2.5 g/L) in an oven at 80 ^{o}C for 60 min to produce the surface-grafted PMETAC by free-radical polymerization. After polymerization, the substrates were rinsed with DI water and dried in air.

To perform dip-pen nanolithography (DPN), the M-type 1-D cantilever array was first immersed in an ethanol solution containing 2.5 mg/mL $(NH_4)_2PdCl_4$ and 10 mg/mL PEG (*Mw*. 300 and 1540, 1:1 w/w) and dried in air. The inked tip was mounted on an atomic force microscope (XE-100, Park Systems) and brought into contact with the PMETAC-grafted PET substrate with dwell time ranging from 1 to 25 s under 80-95%RH. Subsequently, the patterned substrates were placed in the dark for 15 min to load $PdCl_4^{2-}$ into PMETAC layer by ion exchange, followed by rinsing with DI water to remove the PEG matrix and excess catalysts. ELD of Cu was then conducted in a plating bath consisting of a 1:1 mixture of freshly prepared solution A and B. Solution A contains 12 g/L NaOH, 13 g/L $CuSO_4{\cdot}5H_2O$, and 29 g/L potassium sodium tartrate. Solution B is 9.5 mL/L HCHO aqueous solution. After 15 min ELD plating, patterned Cu structures on PET were obtained, which were characterized by optical microscope (Nikon Eclipse 80i) and scanning electron microscope (Hitachi TM3000 Tabletop SEM).

4.3.2 Results and Discussions

In order to create an environment for robust and high-density loading of catalytic ions $PdCl_4^{2-}$, a polyelectrolyte with quaternary ammonium side groups, PMETAC, was grafted onto the surface of flexible PET film through free-radical polymerization. The PET surface was first modified with silanes to generate methacrylate-functionalized surface, followed by *in-situ* polymerization and grafting of PMETAC with covalent bonding formed through the silane SAM. The obtained transparent PMETAC layer was measured as 10-24 nm thick and ~4 nm roughness by AFM. On the other hand, to tune the transport of catalytic ink, PEG was used as delivering matrix. Importantly, the viscosity of ink can be adjusted by the molecular weight and concentration of PEG. For DPN printing, the ink needs to be at low viscosity at the inking state, and at high viscosity during DPN patterning. We screened PEG with various molecular weight and concentrations and found that a semi-solid mixture of PEG 300 and PEG 1540 in 1:1 weight ratio with a concentration of 10 mg/mL can produce reliable patterning results compared with the solid PEG with higher molecular weight. The ink prepared with semi-solid PEG was observed to maintain liquid state after printing for several hours, which could facilitate the diffusion of ions from PEG matrix into the PMETAC layer.

The ink consisting of PEG matrix and $(NH_4)_2PdCl_4$ was then printed onto the PMETAC-modified PET surface by M-type cantilever array under 90%RH. Note that without the delivering matrix, inorganic salts are difficult to deposit from the AFM tip due to the precipitation of salts. Dot arrays were patterned by DPN with varied dwell times over an area of > 1 mm^2 (Figure 4.7A). After printing, the patterned inks were allowed to stay on the PET surface in ambient environment for 15 min, in which the $PdCl_4^{2-}$ anions diffused into PMETAC and were bound to the quaternary ammonium cationic groups by ion exchange. After removing PEG matrix and excess catalysts, the immobilized $PdCl_4^{2-}$ ions were used for site-selective ELD of Cu by immersing the substrate into an ELD plating solution for 15 min at room temperature. Large-area Cu micropattern arrays were successfully obtained in correspondence with the previous DPN patterns (Figure 4.7B).

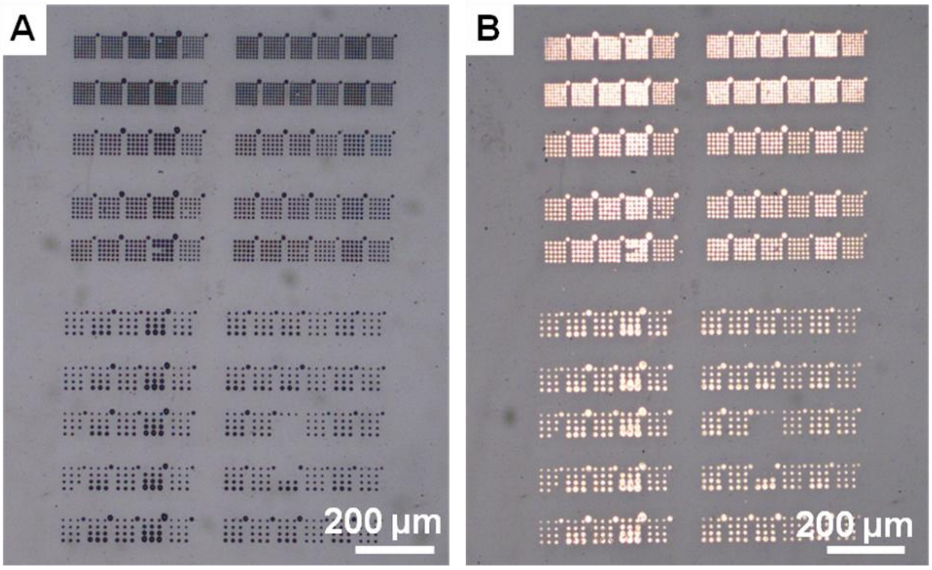

Figure 4.7. (A) Optical microscope image of the printed polymer matrixes with catalysts on the PMETAC-grafted PET by DPN. (B) Corresponding Cu patterns obtained after ELD.

The Cu patterns were characterized by SEM, in which halos were found surrounding each metallic dot due to the diffusion of catalysts. The size of the Cu dots could be controlled by dwell time. As demonstration, dot arrays with dwell time ranging from 0.5 to 25 s were patterned by DPN, and typical Cu patterns with dwell time of 1, 4, 16 s were shown in Figure 4.8A. A linear relationship between the dot diameter and the square root of dwell time was observed, where the feature size of Cu patterns was tuned from 3 μm to 8 μm with increasing dwell time. Moreover, the feature size of Cu patterns could reach even smaller by controlling the experimental conditions, as shown in Figure 4.8B. For instance, a 5 × 5 dot array of Cu was generated with an average diameter of 1.67 ± 0.33 μm (Figure 4.8C) under ~80%RH. Submicrometer Cu features down to ~380 nm could also be achieved (Figure 4.8D). In addition, the as-made Cu patterns passed the Scotch tape adhesion tests, which can be accounted for by the composite layer of PMETAC and metal nanoparticles at the metal/substrate interface formed during ELD. These results confirm the essential roles of delivering and receiving matrixes to improve the loading of catalysts and stability of the obtained metal structures.

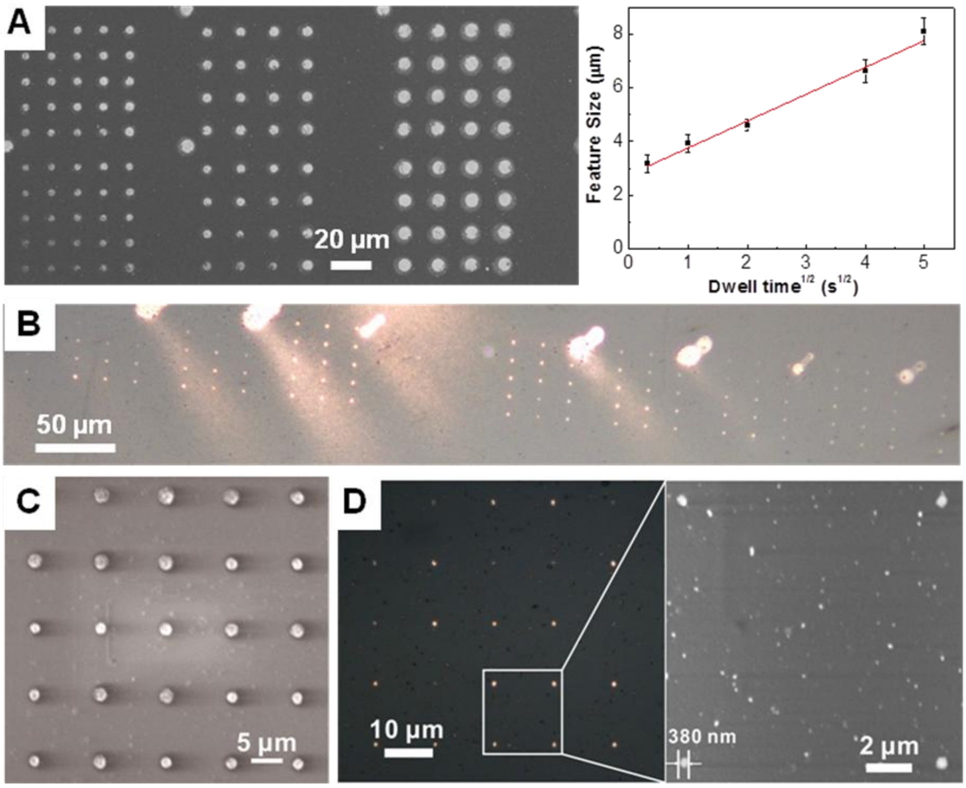

Figure 4.8. (A) SEM image of Cu dot arrays produced by varying dwell time in printing of catalytic ink. The dwell time is 1, 4, 16 s for the arrays from left to right. A linear function is also shown between the feature size and square root of dwell time. (B) Optical microscope image of Cu dot arrays with size of 1-2 µm. (C) SEM image of one Cu dot array with average feature size of 1.67±0.33 µm. (D) Optical and SEM images of submicrometer Cu dot array.

4.3.3 Summary

In conclusion, we have employed direct printing of PEG matrix by DPN onto surface-grafting PMETAC to enable the spatially confined, highly efficient loading of catalytic salts for generating patterned metallic structures on flexible substrate. The use of both delivering and receiving matrixes can be a versatile strategy for various functional materials and substrates especially soft elastomer, paper or textiles.

4.4. Conclusions and Future Outlooks

In this chapter, we discussed the patterning of polymer materials by direct printing with AFM tip arrays and polymer pen arrays. Water-soluble polymer inks were demonstrated to be printed from the AFM tip or polymer pen array in a way of either molecular diffusion or liquid deposition. Also the function of liquid polymer matrix was highlighted to enable printing of ink materials that are difficult to be delivered. Despite the success of direct printing approach, it still faces limitations in ink material, environment conditions, and fabrication of complex structures. Therefore, indirect or hybrid patterning strategies are in demand to pattern other functional polymers that are difficult to print.

CHAPTER 5

PATTERNING MOLECULAR TEMPLATES FOR FABRICATION OF 3D POLYMER BRUSHES

In this chapter, a “bottom-up” approach is described to generate 2D and 3D complex polymer brush nanostructures to over large areas by printing molecular templates using 2D polymer pen arrays followed by surface-initiated polymerization. The applications of such 3D-structured polymer brushes were then explored.

5.1 Introduction

Polymer brushes are polymers with one end of the polymer chain tethered onto a surface. The vertically aligned, covalently bonded polymer chains have shown remarkable advantages in surface functionalization by creating a robust three-dimensional (3D) environment with high spatial density of functional groups. The ability to pattern polymer brushes by either bottom-up “grafting from” pre-immobilized initiators or top-down destructive methods further extends their device applications into new areas, and enables the fundamental study of the behavior of polymer chains at different length scales. More recently, polymer brushes have been considered as building blocks to construct 3D gradient or complex 3D structures based on controlled polymer growth or the steric interaction between the polymer chains under nanoscale confinement.[224-225] The unique 3D-patterned surface is particularly highlighted in material and bio-related researches for the studies in cell adhesion and growth, surface molecular transport or high-throughput screening of nanomaterials.

Despite the tremendous potentials of complex 2D and 3D polymer brush structures, the lack of high-throughput tools to fabricate them over a macroscopic area has dramatically hindered their usage both in fundamental research and practical applications. Current serial lithographic methods such as e-beam lithography (EBL)[226-229] and scanning probe lithography (SPL)[132-133, 137, 160, 163] are dominant techniques in fabricating complex 2D and 3D polymer brushes with ultrahigh resolution. The fatal drawback for the serial methods, however, is very low throughput, leading to limited patterning areas and very high cost per patterning unit. Indeed, the state-of-the-art demonstration of patterning 2D and 3D arrays of polymer brushes by serial methods is limited to a throughput of ~1 mm × 0.1 mm in 1 hr, far too low for most applications. On the other hand, mask or mould-based lithography such as photolithography,[18, 230-231] imprint lithography,[232-233] colloidal lithography,[234] and microcontact printing[235-238] can rapidly produce patterned polymer brushes with submicrometer resolution over square-centimeter areas. Despite a few reports on patterning gradient polymer brushes by controlling optical intensity using interference or gray-scale photomask,[18, 230-231] or by multi-step contact printing,[235, 237] it is very challenging for the above approaches to produce arbitrary and complex structures with fine control. To date, how to realize large-area fabrication of complex 2D and 3D polymer brushes for practical applications in a simple, rapid, and cost-effective manner remains to be a central challenge in this field.

Herein, PPL as a “bench-top” printing technique was explored for massively parallel and serial patterning of 2D and 3D polymer brushes over macroscopically large areas, and the applications in material micro/nanofabrication and microarray-based bioassays were demonstrated. By directly printing initiator molecules on a substrate followed by growth of functional polymer brushes from the printed molecular templates via surface-initiated atom transfer radical polymerization (SI-ATRP, **Figure 5.1**), we show that patterned submicrometer-sized 2D arrays and complex 3D arrays of polymer brushes can be readily generated over square-centimeter areas with good uniformity, and more importantly, a remarkable throughput being 3 orders of magnitudes higher than the best result reported in the literatures using serial fabrication methods. This method can meet the throughput and resolution requirement for lab-scale rapid prototyping of functional 2D and 3D templates for various purposes. As proof-of-concept, we demonstrate the use of 2D arrays of polymer brushes as effective etching resist for micro/nanofabrication of metal structures and soft stamps, and 3D-patterned polymer brushes as functional immobilization substrates to generate bioactive DNA and protein 3D arrays.

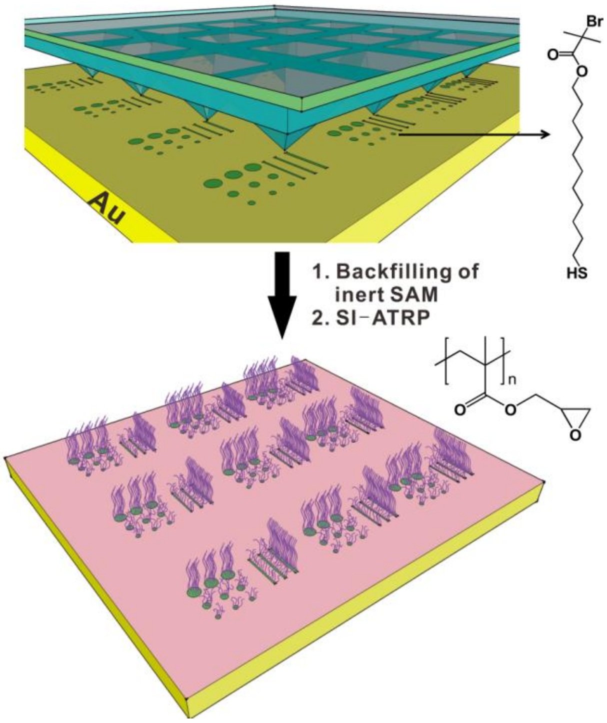

Figure 5.1. Schematic illustration of the large-area, arbitrary patterning of PGMA brushes through a combination of PPL and SI-ATRP.

5.2 Experimental

5.2.1 Materials

ATRP initiator ω-mercaptoundecyl bromoisobutyrate (MUDBr, see chemical structure in Figure 5.1) was kindly provided by Prof. Hongwei Ma, Suzhou Institute of Nano-Tech and Nano-Bionics. Oligonucleotides were purchased from Takara (Dalian, China). The target sequence was 5’-NH_2-$(CH_2)_6$-CAT GAT TGA ACC ATC CAC CA-TET-3’ and the probe sequence was 5’-TAMRA-TGG TGG ATG GTT CAA TCA TG-3’. The random control sequence was 5’-TAMRA-CAT AGT GTG GAC CCC TAG CA-3’. Glycidyl methacrylate (GMA, Aldrich) was purified on a neutral alumina column before use. All other chemicals were obtained from Sigma-Aldrich and used as received. Au substrates were prepared by thermal evaporation of 25 nm Au/5 nm Cr on n-doped <100> silicon wafers.

5.2.2 Polymer Pen Lithography (PPL)

Prior to patterning, the Au substrates were cleaned by ultrasonication in DI water, acetone, isopropanol sequentially and were blown dry with N_2. A drop of 1 mM MUDBr ethanol solution was spin coated onto the polymer pen array at 3000 rpm for 30 s for inking. The inked polymer pen array was then mounted onto the customer-made z-piezo scanner of AFM (XE-100, Park Systems) and aligned to the plane of the Au substrate. After leveling, the pen array was programmed to contact with the substrate to write the initiator patterns at 15-20% relative humidity (RH) and room temperature (RT). Finally, the initiator-patterned substrate was backfilled with 1 mM octadecylthiol (ODT) or 0.5 mM 11-mercaptoundecyl tri(ethylene glycol) (EG_3) ethanol solution for 30 min.

5.2.3 SI-ATRP of PGMA Brushes

GMA (7.5 mL), methanol (6 mL) and DI water (1.5 mL) were mixed and bubbled with argon for 15 min in a Schlenk tube, followed by dissolving copper(I) bromide (CuBr, 78 mg) and 2,2’-dipyridyl (dipy, 210 mg). The resulting dark brown mixture was transferred into an argon purged 15 mL centrifuge tube containing the initiator-patterned substrate to start the polymerization. After 2 h polymerization at 30±1 °C, the substrate was taken out and rinsed with methanol and water, then it was washed in dichloromethane and methanol followed by blow drying with compressed air.

5.2.4 Au Etching and PDMS Stamp Fabrication

The patterned PGMA brushes were exposed to 30 s O_2 plasma to remove the background SAM. Subsequently, the substrate was immersed in the Au etching solution containing 20 mM thiourea, 30 mM $Fe(NO_3)_3$, 20 mM HCl and 20 mM octanol for 5 min to obtain the Au patterns. To transfer the pattern to a PDMS stamp, a thin layer of 2 nm Cr and 10 nm Au was evaporated onto the etched substrate. Subsequently, the substrate was immersed in 5 mM 1H,1H,2H,2H-perfluorodecanethiol ethanol solution for 24 h. PDMS (Sylgard 184, Dow Corning) prepolymer and crosslinker (10: 1 w/w) were mixed and degassed, and then the liquid was poured onto the fluoro-treated substrate and cured at 70 °C for 2 hrs to obtain PDMS stamp with replicated patterns.

5.2.5 Immobilization of Biomolecules on Brush Patterns

The substrate with patterned PGMA brushes and EG_3 background was employed in the immobilization experiments. A 20-mer, 5'-amine-modified oligonucleotide labeled with TET in 3'position was dissolved in 1× PBS (pH=8) to prepare a 10 μM solution. The substrate was covered with the target oligonucleotide solution (ca. 10 μL) and then placed in a sealed chamber with saturated NaCl solution over night at RT. Unreacted oligonucleotides were removed by washing with 1× PBS and DI water under vigorous shaking for 15 min. Subsequently, the reactive groups on the substrate were blocked with 50 mM ethanolamine in 10× Tris EDTA (pH=7.6) for 1.5 h at RT. For hybridization, 100 nM TAMRA-labeled oligonucleotide in the hybridization buffer (4× SSC, 0.08% SDS) was applied to the above substrate. The hybridization was maintained at 45 °C for 7 h, followed by sequentially washing the substrate with hybridization buffer at 45 °C for 10 min, 0.1× SSC with 0.01% SDS for 5 min at RT and DI water for 5 min. Protein immobilization was achieved by dropping 1 μL of IgG (from human serum, Sigma) solution (50 μg mL^{-1} in 1× PBS) onto the brush-patterned substrate. After 16 h incubation at RT, the substrate was washed in 0.6× PBS, 0.02% Tween-20 with vigorous agitation for 30 min. The substrate was blocked with BSA (100 μg mL^{-1} in 1× PBS) at 37 °C for 30 min, and then was incubated with FITC-labeled anti-IgG (anti-human IgG-FITC antibody produced in goat, Sigma) solution (0.1 - 50 μg mL^{-1} in 1× PBS) at RT for 2 hrs, followed by thoroughly washing.

5.2.6 Characterization

Optical and fluorescent images were recorded with a Nikon Eclipse 80i optical microscope (Nikon, Japan), λ_{ex} = 465–495 nm, λ_{obs} = 515–555 nm for green fluorescence and λ_{ex} = 528–553 nm, λ_{obs} = 577-632 nm for orange fluorescence. AFM topography was measured by an XE-100 AFM (Park Systems, Korea) with non-contact mode at ambient conditions. ATR-FTIR was performed using PerkinElmer Spectrum 100 FI-TR spectrometer. SEM images were taken with a Hitachi TM3000 tabletop electron microscope (Hitachi High-Technologies Corp., Japan).

5.3 Results and Discussions

5.3.1 Patterning of 2D and 3D Polymer Brush Arrays

Polymer pen arrays with pyramidal tips made of hard polydimethylsiloxane (*h*-PDMS) were used to conduct the PPL experiments (see Chapter 3 for detail fabrication process of the pen arrays). In a typical experiment, the size of the tip array is 6.6 × 4.2 mm^2 and it contains ~4,500 pyramidal tips (40 μm edge length, 80 μm pitch) with tip radius of curvature being ~100 nm. The polymer pen array was inked with the ATRP initiator ω-mercaptoundecyl bromoisobutyrat (MUDBr) by spin coating, and then attached onto the customer-made scanning head of AFM (XE-100, Park Systems), which was placed in an environmental chamber (15%-20% relative humidity, 25±1 ^{o}C). Because the intitiator molecules are volatile and the ink writing is dependent on humidity, the dry environment can effectively reduce ink diffusion for high resolution patterning. The inked tips were leveled, and then brought to contact with the underlying Au substrate at different positions, dwell times and contact areas, where MUDBr molecules diffused and self-assembled on the Au surfaces at the areas of contact. As shown in the design schematic in Figure 5.2A, each pyramidal tip was programmed to fabricate three arrays: a 7×4 dot array (pitch = 7 µm) with dwell time (*t*) ranging from 0.1 s to 9 s in each column, a 5×4 dot array (pitch = 7 µm) with relative Z-piezo extension (Z_{ext}) ranging from 0 to 3 µm in each column, and a dotted line array of 4 lines (pitch = 7 µm) with dot-to-dot distance (*d*) decreasing from 2500 nm to 250 nm in each line. After PPL patterning, the Au substrate was immediately backfilled with inert thiols such as octadecylthiol (ODT) or 11-mercaptoundecyl tri(ethylene glycol) (EG_3) for surface passivation, which can ensure no polymers will grow in the background. Multifunctional poly(glycidyl methacrylate) (PGMA) was chosen as the target polymer because their reactive epoxy side groups could be used for further immobilization of biomolecules. PGMA brushes were grown from the initiating moieties by immersing the MUDBr-patterned Au substrate into an ATRP reaction solution. After brief rinsing with fresh solvents, patterned arrays of PGMA brushes from a 2h polymerization were clearly seen from the optical microscope (Figure 5.2B and C), where the denser polymer brushes showed darker appearance. All tips of the pen array succeeded in patterning (Figure 5.2C), i.e., ~4,500 replicas of molecular templates for PGMA brush arrays were generated simultaneously in ~20 min. The brush patterns exhibited high uniformity, for instance, patterned dots with 1 s dwell time showed an average size of 1.39±0.09 µm and size variation of 6.5% from statistics of 9 arrays across ~2 mm distance.

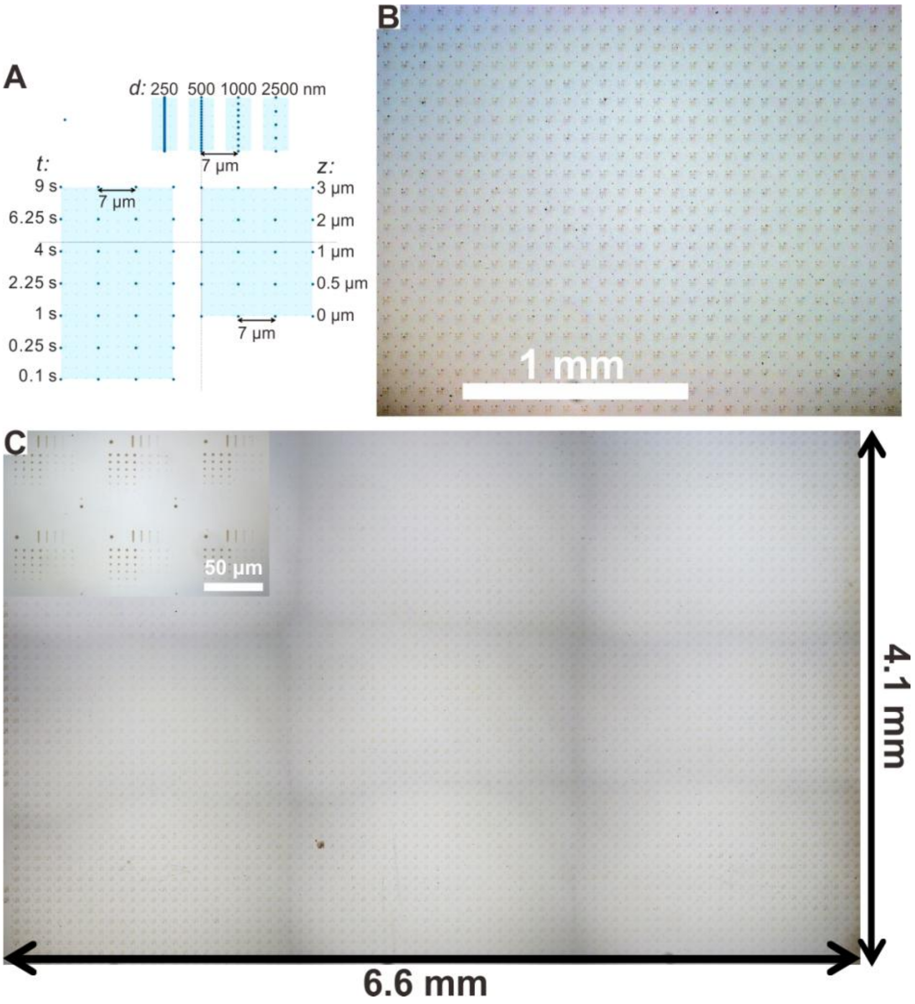

Figure 5.2. (A) Designed patterning parameters for brush arrays in PPL. In the bottom left array, the dwell time (t) ranges from 0.1 s to 9 s from bottom to top, and the z-piezo extension (z) is set as 0.5 µm; in the bottom right array, z increases from 0 to 3 µm from bottom to top (t=0.25 s); in the top array, the feature distance (d) varies from 250 to 2500 nm from left to right, with t=0.25 s and z=0.5 µm. (B) Optical microscope image of the patterned PGMA brush arrays over large areas. (C) Image of brush patterns over the whole 6.6 by 4.1 mm^2 area. The figure is obtained by blending 9 optical microscope images using Photoshop. Inset shows a magnified optical microscope image of the pattern arrays.

Because the tip arrays are fabricated by moulding methods with PDMS similar to those in soft lithography, the size of the tip arrays and the number of tips can be readily scaled up. In the current study, we also succeeded in using a larger tip array containing $\sim 3\times10^4$ tips to fabricate similar PGMA structures over 2 × 1 cm^2 areas following the same procedures (Figure 5.3A). Compared with the state-of-the-art serial fabrication of polymer brushes in the literature, the throughput of our method is at least 3 orders of magnitudes higher. For example, patterning by single AFM tip[137] and 1D cantilever array[138] present a patterning speed of 1 and 18 features per writing time within an area of 0.1 × 0.1 mm^2 and 0.1× 1.2 mm^2, respectively, while PPL shows at least 10^3 fold increase in throughput (10^3-10^4 features per writing time) and covered area (>1 × 1 cm^2), despite the larger feature size by polymer tip (>250 nm) than that by Si tip (~100 nm). Note that the throughput can even be improved much further, providing that larger tip and sample holders are used. Because of the considerable quantity of patterned brushes over a macroscopic area, we were able to verify the chemical structures of PGMA by attenuated total reflectance Fourier transform infrared (ATR-FTIR) spectroscopy. Indeed, characteristic peaks of GMA were found at 907 cm^{-1} for the epoxide group, 1265 and 1150 cm^{-1} for the ester group, 1735 cm^{-1} for the carbonyl group, and 2930 and 2855 cm^{-1} for C-H stretching (Figure 5.3B). In contrast, this kind of spectroscopic analysis is very difficult for structures generated by low-throughput serial methods because the patterning area is typically less than 1 mm^2.

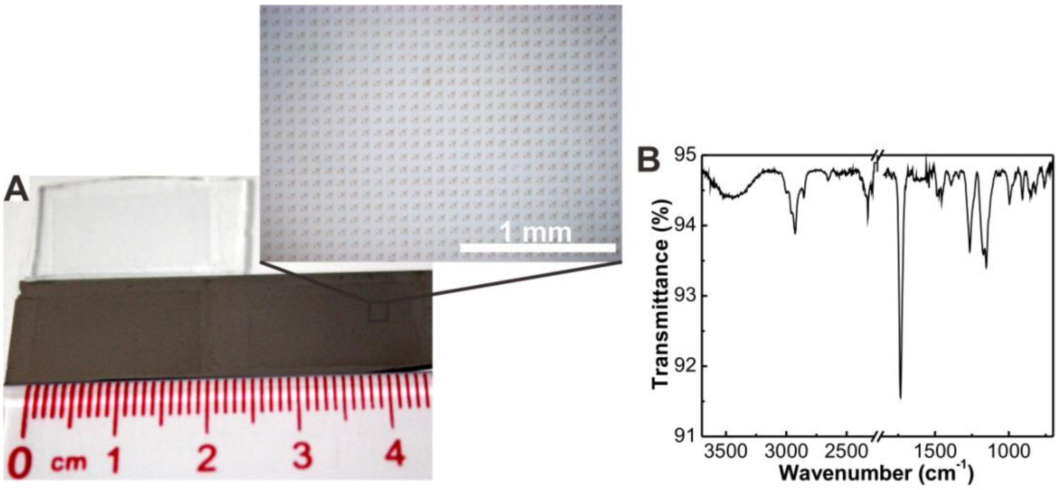

Figure 5.3. (A) A polymer pen array with ~2×1 cm^2 patterning area and the corresponding 2-cm^2 PGMA brush arrays on Au substrate. (B) ATR-FITR spectra of the patterned PGMA brush arrays.

Taking advantages of the scanning probe system, the feature size of PGMA brushes can be tailored by controlling the contact force and contact time in PPL experiments, allowing rapid generation of patterns with size ranging from submicrometer to tens of micrometers and various shapes. As the polymer tip was just contacted with the substrate with minimum tip deformation ($Z_{ext} = 0$), nanodots of PGMA brushes were produced with feature sizes of 250-400 nm (full width in half maximum, FWHM). Figure 5.4 shows a typical nanodot array of ~340 nm feature size (t = 0.25 s). When gradually pushing the Z_{ext} to 3 μm, i.e., increasing the contact force between the tip and the substrate, the edge size of PGMA brushes increased to 2.42±0.03 μm as a first-order function of the Z_{ext} (Figure 5.4A and B). The size change is attributed to the elastic deformation of the tips at different applied forces. Note that "X"-shaped features of polymer brushes were obtained at $Z_{ext} > 0.5$ μm instead of square ones, indicating an uneven distribution of the initiators on the tip-substrate contacts at large Z_{ext}. This phenomenon can be explained by that at large contact force and short contact time, the initiator molecules at the edges of the pyramidal tip preferentially contact with the substrate under tip deformation and do not have enough time to fill the underlying substrate.

The insufficient deposition of ink can be addressed by increasing the dwell time. Indeed, we observed an obvious shape transition from "X" to square and to dot, when we gradually increased the dwell time from 0.1 s to 9 s at fixed contact force (Z_{ext} = 0.5 μm). Notably, the shape transition was accompanied with size increase on both the edge length and height of the brushes: the edge length of PGMA features increased from 1.02±0.04 μm to 2.36±0.05 μm as a first-order function of $t^{1/2}$, and the corresponding brush height raised from 15±1 nm to 59±2 nm (Figure 5.4C and D). However, the brush height remained almost constant at dwell time longer than 9 s. The above phenomena can be ascribed to the diffusion of thiol initiators. As time goes, the initiator molecules can diffuse to fill in all the tip-substrate contact areas to form square shape. At the mean time, they also diffuse laterally through the water meniscus between the tip and the substrate so that the edge length grows. Since the lateral diffusion is isotropic, the square feature shall eventually become dot shape. During the ink diffusion process, the grafting density of initiator molecules, i.e., number of initiator molecules per unit area, also increases. When polymer brushes grow from denser initiators, the polymer chains tend to stretch up to form a higher structure because of the stronger repulsion force between neighboring chains, and vice versa.

Apart from patterning 2D arrays of polymer brushes, 3D polymer brush structures were also generated by employing a “feature density” concept developed in our group[137-138]. In the feature density method, polymer brushes of the same size and height are used as building blocks, and are positioned in controlled lateral spacing. When the spacing is small enough, the topography of the neighboring building blocks will change because of the configuration stretching of the polymer chains. For instance, isolated PGMA brush dots with size of ~1.2 μm and height of 17±1 nm were fabricated at the dot-to-dot spacing of 2500 nm. As the feature spacing reduced to 250 nm, the brush dots were observed to merge together, accompanied with increase in the brush height. Finally, lines with smooth top surface were obtained at the 250-nm feature distance with the average brush height of 45±2 nm (Figure 5.4E and F).

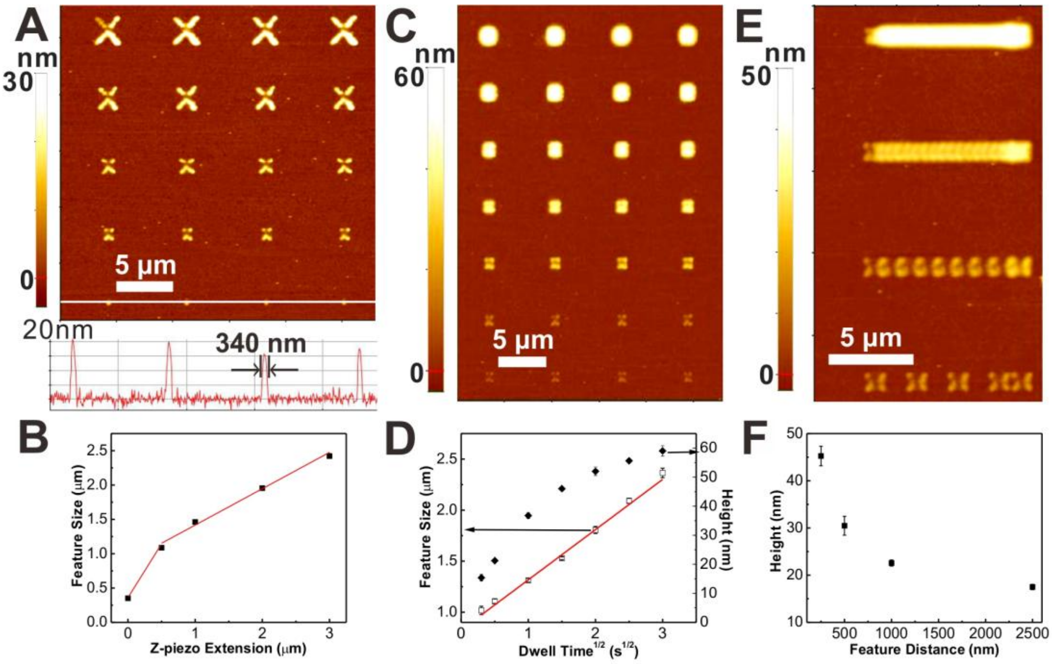

Figure 5.4. (A) AFM topography of a typical PGMA brush array made with various z-piezo extensions. (B) Plot of the feature size versus z-piezo extension. (C) AFM topography of PGMA brush array made with various dwell times. (D) Plot of the feature size and brush height versus $t^{1/2}$. (E) AFM topography of PGMA brush array made with various feature distances. (F) Statistical results of the brush height at different feature distance, obtained from 4 different arrays.

With the same principle, large-area arrays of various complex 3D structures of PGMA brushes were successfully patterned by converting a grayscale bitmap into a feature density map of initiators, in which the black pixels were PPL printing positions while the white pixels served as spacing. Arrays of pyramids, triangular gradients and donuts were chosen as proof-of-concept structures for demonstration (Figure 5.5). Take the fabrication of pyramids for example. The neighboring black pixels were set respectively to be 1200 nm, 600 nm, and 300 nm for the bottom, middle, and upper layers, corresponding to the resulted brush height of 20 nm, 50 nm and 70 nm approximately. Considering the similar feature distance, the pyramid still shows higher height than that of 1D lines shown in Figure 1G, indicating that the dimensionality of pattern also affect the 3D topography. The 2D initiator map for fabricating pyramid leads to enhanced steric repulsion effect from all directions along the 2D plane as well as increased initiator density compared with 1D pattern, as a result, much higher brushes can be grown. Again, the 3D patterns appear to be uniform over the writing areas with well controlled height variations of the structures, except for a few arrays showing much higher brushes due to the low-quality tips or non-uniform inking by spin coating.

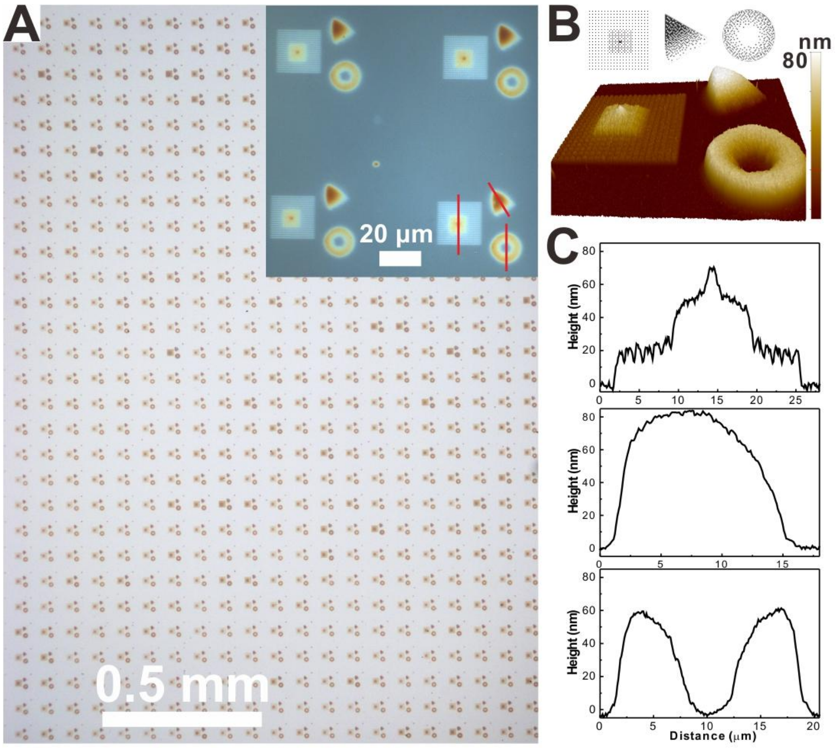

Figure 5.5. (A) Optical microscope images of the large-area patterned 3D structures of PGMA brushes. The inset shows a magnified polarized optical image of the 3D patterns. (B) The bitmap density maps used to fabricate the 3D structures and the corresponding 3D AFM topography image of the patterned PGMA brushes. (C) Cross-sectional analysis of the topographic profiles of 3D PGMA patterns. The selected cross sectional positions are shown as red lines in the inset of A.

5.3.2. PGMA Brushes as Resist for Micro/nanofabrication

The as-made large-area, arbitrarily patterned 2D and 3D PGMA brushes can be readily used as functional templates for a wide range of research areas. We demonstrate herein four examples of how one can make use of these PPL-patterned brushes in applications of micro/nanofabrication and bioassays. First of all, we show that patterned PGMA brushes can serve as etching resist in generation of 2D Au micro/nanopattern arrays (Figure 5.6A). Polymer brushes have been previously reported as superior etching resist to SAMs because they are less likely to generate pinholes and can resist strong etchants.[239] As demonstration, patterned PGMA brushes on Au made with various z-piezo extensions, dwell times, and feature densities (Figure 5.6B) were exposed to O_2 plasma briefly to remove the background SAM. The substrate was then immersed in an Au etching solution, in which Au was etched away on the uncovered areas. From the optical microscope and SEM images (Figure 5.6C&D), it was found that the brush patterns could be successfully transferred to Au patterns after the chemical etching step. Submicron Au patterns can be obtained using PGMA brush features generated under the conditions of $Z_{ext}<1$ μm and $t<1$ s, with the smallest dot diameter of ~250 nm and line width of ~450 nm. Note that Au lines are formed only with sufficient polymer brush height, e.g. at feature distance of 500 nm or less, otherwise isolated dots are obtained, indicating that thicker brush film (>10 nm) has better resist property.

These brush-protected Au patterns can further work as hard moulds to replicate PDMS stamps for soft lithography. We first coated the Au-etched substrate with a thin Au/Cr layer (10 nm Au/2 nm Cr) followed by surface fluorination treatment with 1H,1H,2H,2H-perfluorodecanethiol. The treated substrate was then used as a mould for PDMS replication to obtain a PDMS stamp with 3D relief structures (Figure 5.6A&E). The AFM topography images of the PDMS stamp show concave patterns with varying size and depth complementary to the original convex patterns of PGMA brush/Au. The depth of 35-70 nm is in accordance with the total height of PGMA brushes (15-50 nm) and Au (25 nm). Submicron features down to ~500 nm can be successfully replicated. To the best of our knowledge, this is the first report on fabricating macroscopic-sized hard moulds and PDMS stamps using scanning-probe-based techniques. The replication of 3D-structured stamp also provides a way to fabricating other functional 3D-structured or topographic gradient surface by imprinting.

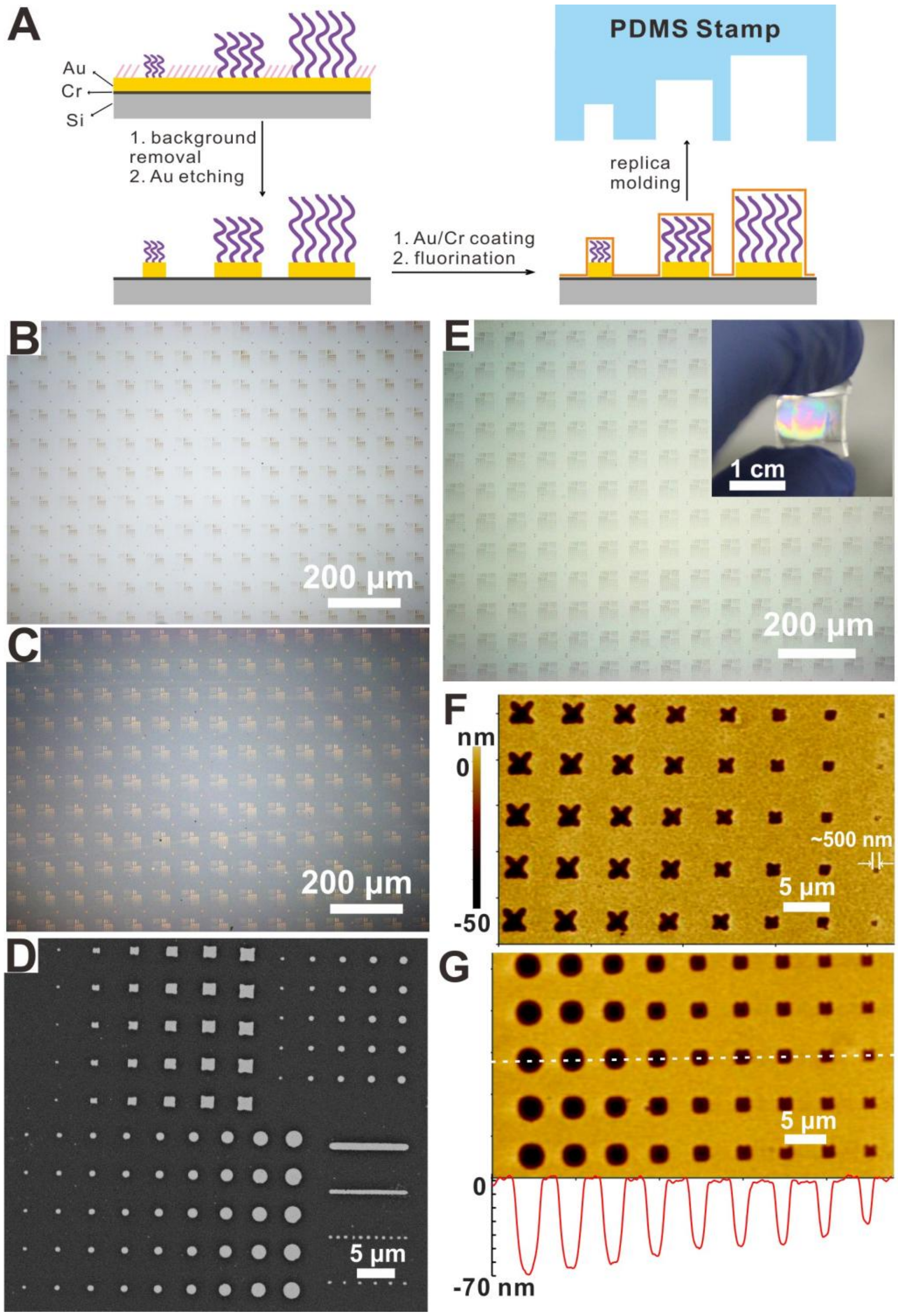

Figure 5.6. PGMA brushes as resists for micro/nanofabrication. (A) Scheme of the fabrication of Au arrays and PDMS stamp. (B) Optical microscope images of the PPL-patterned PGMA brushes, and (C) the resulted Au arrays after etching. (D) SEM image of a typical array of Au patterns shown in C. (E) Optical microscope image of a PDMS stamp fabricated from patterns shown in C as the mold. The inset shows the digital image of the 1×1 cm^2 PDMS stamp. (F, G) AFM topography images of the concave pattern arrays on the PDMS stamp. The profile shows the depth varying from 35 to 70 nm.

5.3.3. PGMA Brush Templates for Biomolecular Immobilization

Not only can polymer brushes be used as physical resists for etching and moulding purposes, but also they act as chemically and biologically active templates if one designs the chemical structures properly. For instance, epoxy groups in PGMA brushes easily react with amines so that one can use them to immobilize biomolecules such as DNAs, proteins, and enzymes.[240] Apart from 2D arrays, 3D biomolecular arrays are particularly interesting platforms for cellular environment since they provides patterned surface with biological/chemical and topographic gradients, which can decouple the complex chemical and physical parameters involved in the cell adhesion and growth processes, such as geometry and nanoscale topography. Also, gradient structures can serve as model systems to understand the transport and motion of biomolecules on the surface. We demonstrate herein that the usage of PPL-patterned PGMA brushes passivated with 3-nm-thick EG_3 monolayer (Figure 5.7) for the production of DNA oligonucleotide microarrays and 3D gradient arrays of proteins over large areas. It is worth noting that once being made, PGMA brushes are highly stable at ambient conditions so that they are active even after storage for several months, which will benefit practical biochip applications.[241]

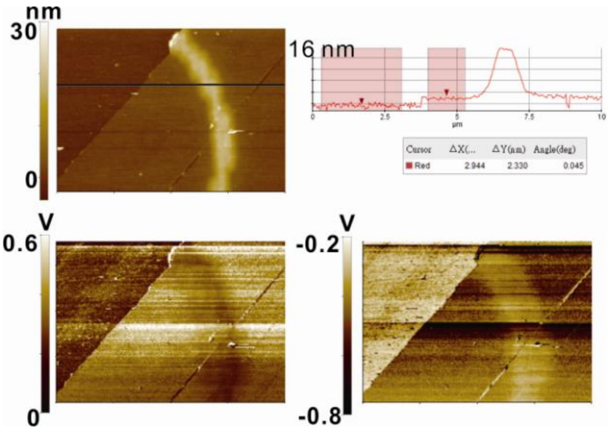

Figure 5.7. AFM topography and lateral force images of PGMA brush pattern backfilled with EG_3 SAM.

For DNA oligonucleotide arrays (Figure 5.8A), PGMA brushes with EG_3 SAM background were first produced by PPL with four basic pattern designs, namely triangle, square, ring and cross (Figure 5.8B and E). The line width for the four patterns ranged from 1.7 to 2.4 μm and the height was controlled as 30, 40, 50 and 60 nm respectively by tuning the feature distance. A drop of 10 μM solution of 5'-amino-modified, 3'-TET-labeled oligonucleotides (TET-ssDNA) was then dropped onto the patterned PGMA brushes followed by overnight incubation, during which TET-ssDNA covalently bound to the brushes through the ring-opening reaction of epoxy groups with amine. Because TET dye shows maximum λ_{ex} of 521 nm and λ_{em} of 536 nm, after rinsing away the physisorbed molecules, green fluorescence was seen from the patterned regions under blue light excitation (λ_{ex} = 465–495 nm, λ_{em} = 515–555 nm), and there was no observable adsorption on the background (Figure 5.8C). Note that a difference in the fluorescence intensity was observed from four patterns with different brush heights. From statistical results of 9 arrays, the average fluorescence intensity shows significant increase with the increasing brush height from 30 to 50 nm, however, the increment lowers at a brush height of 60 nm (Figure 5.8F). To test whether the PGMA-bound TET-ssDNA is bioactive, the ssDNA was further hybridized with its complementary strand by immersing the substrate into a 100 nM 5'-TAMRA-labeled complementary DNA oligonucleotide (TAMRA-cDNA, maximum λ_{ex} = 555 nm, maximum λ_{em} = 580 nm) solution for 7 hrs at 45 °C. The success of hybridization was confirmed by the observation of orange fluorescence under green light excitation (λ_{ex} = 528–553 nm, λ_{em} = 577-632 nm) as well as the decreased intensity in green fluorescence under blue excitation due to the fluorescence resonance energy transfer process between the two adjacent dyes (Figure 5.8D & Figure 5.9).[242] We also tested a random sequenced probe as control, and observed none of the two above phenomena. The double-stranded DNA also shows stronger fluorescence on the higher brushes due to higher spatial density of reactive sites.

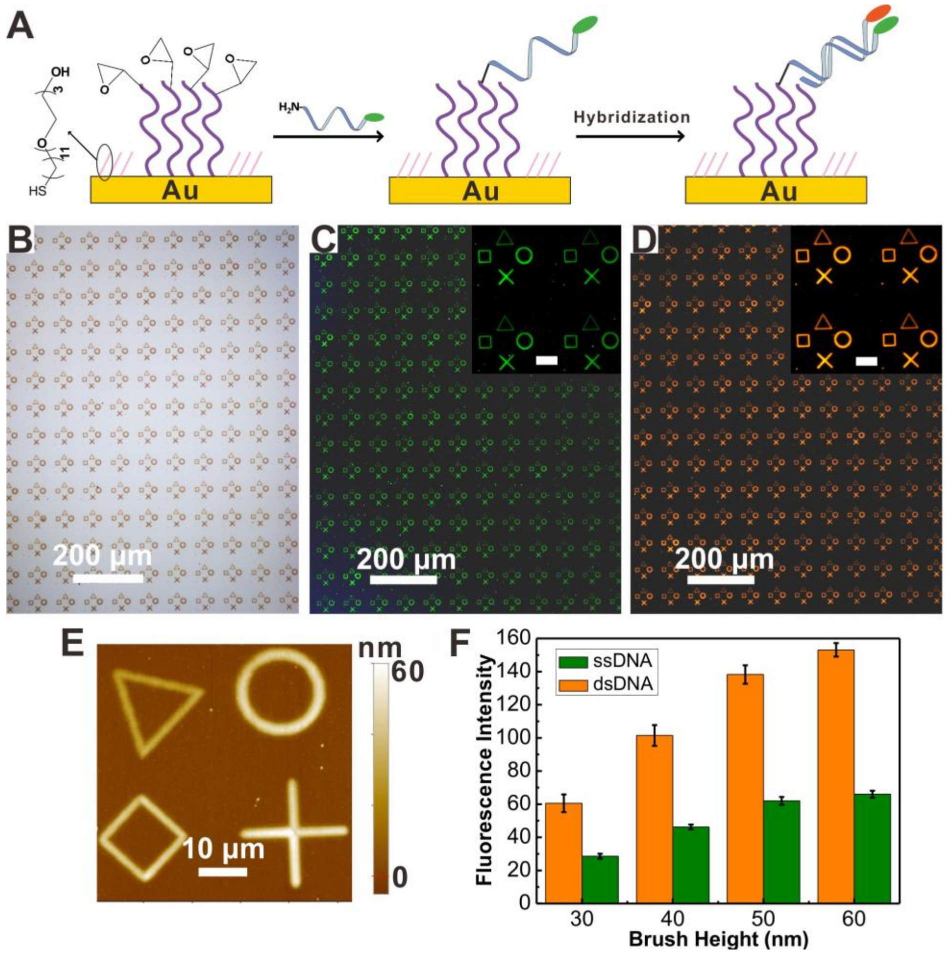

Figure 5.8. PGMA brushes for DNA immobilization. (A) Scheme of DNA binding and hybridization on PPL-patterned PGMA brushes. (B) Optical microscope image of PGMA brush pattern arrays. (C-D) Fluorescent microscope images of the patterned PGMA brushes bound with 5'-NH_2, 3'-TET-modified ssDNA (C), and after hybridization with 5'-TAMRA-labeled complementary probes (D). λ_{ex} = 465–495 nm, λ_{obs} = 515–555 nm for green fluorescence and λ_{ex} = 528–553 nm, λ_{obs} = 577-632 nm for orange fluorescence. The scale bars in the insets are 20 μm. (E) AFM topography of the patterned PGMA brushes. (F) Statistical results of fluorescence intensity counts for TET-ssDNA and dsDNA with different brush height, obtained from randomly selected 9 arrays.

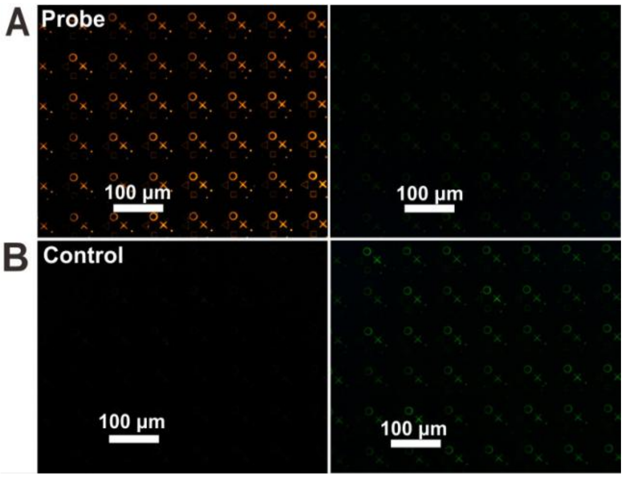

Figure 5.9. Control experiments of DNA hybridization. One sample with TET-ssDNA functionalized PGMA brushes was cut into two pieces for the hybridization with probe and control oligonucleotides respectively. After hybridization and washing, the sample with random sequenced control oligonucleotides did not present orange fluorescence, but stronger green fluorescence than the probe oligonucleotides.

The 3D-patterned brushes can also be useful supports for 3D protein microarrays and the effect of the 3D morphology on the protein immobilization was examined. A model system for immune assay, human IgG and anti-human IgG, was taken as a demonstration. Human IgG was first immobilized onto the above-mentioned 3D brush structures (as those shown in Figure 4.) by incubating the brush-patterned substrate with a 50 µg mL^{-1} IgG solution at room temperature for 16 hrs. After passivating with bovine serum albumins (BSA) and washing, the substrate was then covered with FITC-labeled anti-human IgG (50 µg mL^{-1}) and incubated for 2 hrs. The specific biomolecular interaction between the immobilized IgG and the captured anti-IgG resulted in strong fluorescence (Figure 5.10). The obtained protein microarrays exhibit gradient fluorescence intensity as a function of its corresponding topography (as those shown in Figure 5.5B). When the brush height is below 60 nm, the fluorescence intensity increases as brush height increases, and it reaches a plateau when the brush height is around 60 nm. Surprisingly, the fluorescence intensity decreases when the brush is higher than ~65 nm. This phenomenon may be attributed to the difficulty in infiltration into polymer brushes with very high grafting density for anti-human IgG.[52-53] In addition, analysis was also conducted on the concentration of FITC-labeled anti-IgG on a single brush-patterned substrate by taking advantage of the massive microarrays over large areas. We printed 4 drops of FITC-labeled anti-IgG solution with concentration ranging from 0.1 to 20 μg mL-1 onto the patterned brushes over ~4×4 mm^2 area, with each drop occupying ~2-3 mm^2 area. We then compared the fluorescence intensity on the three-step pyramid patterns that have the approximate height of 30, 60, 80 nm for each step obtained from the 4 regions. The fluorescence intensity decreases as reducing concentration, but it is still observable at 0.1 μg mL^{-1} concentration for 60-nm-thick brushes. And in all range of concentration, the 60-nm-thick brush shows the highest intensity while the 80-nm-thick brush leads to weaker fluorescence. The above results suggest that 3D polymer brushes are potentially effective platforms to examine the infiltration of molecules or even nanomaterials into polymer of different grafting densities as well as high-throughput screening by combining with other bio-printing techniques.

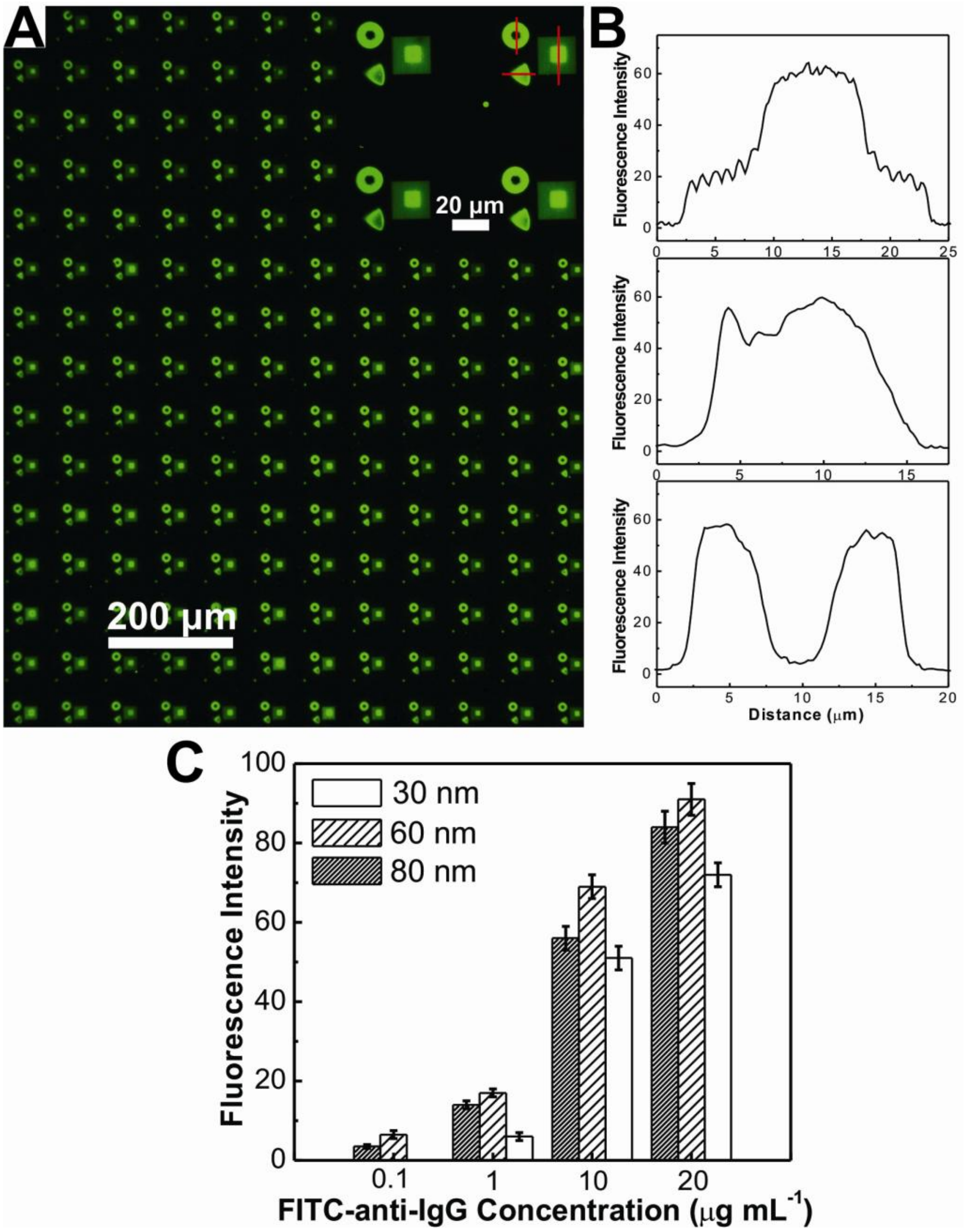

Figure 5.10. Protein immobilization on 3D-patterned PGMA brushes. (A) Fluorescent microscope images of the immobilized human IgG/FTIC-labeled anti-human IgG on the 3D-patterned PGMA brushes. (B) Cross-sectional analysis of the fluorescence intensity from one array shown in the inset of A. (C) Statistic results on fluorescence intensity versus FITC-anti-IgG concentration and brush height collected from the fluorescence image of the 3-step pyramid patterns.

5.4. Conclusions and Future Outlooks

In this chapter, the molecular printing capability of PPL has been combined with SI-ATRP to demonstrate the first example of large area (~2 cm^2) serial patterning of complex 2D and 3D polymer brushes. Importantly, the throughput of fabrication is 3 orders of magnitude higher than the best results reported previously using serial lithographic methods. The shape, feature size and height of the brush patterns are well-controlled by tuning the dwell time, contact force and feature distance. The patterned PGMA brushes were demonstrated as effective etching resists and robust, active platforms for chip-based bioassays. This low-cost “bench-top” fabrication tool meets the requirements for lab-scale high speed prototyping of micrometer and sub-micrometer structures and proof-of-concept experiments for combinatorial screening in chemical, material and biomedical research fields, given that polymer brushes posses a wide diversity of tailored functionality, such as templates for loading ions and nanoparticles or guiding self-assembly, and responsive properties to environmental stimuli etc. In addition, other patterning strategy with cantilever-free pen array can be explored for fabricating 3D brush nanostructures, e.g. by molecular displacement between the printed initiators and a protective SAM on the substrate; or immobilization of initiators assisted with mechanical or optical energy.

CHAPTER 6

SCANNING OPTICAL LITHOGRAPHY BY APERTURELESS POLYMER PEN ARRAYS

In this chapter, in addition to printing materials, the delivery of energy by cantilever-free polymer pen arrays is exploited for patterning on photoreactive surfaces. In particular, based on the unique optical property of transparent, self-light-focusing PDMS pyramids, a novel apertureless cantilever-free pen array was developed for dual scanning optical lithography and photochemical printing.

6.1. Introduction

Techniques for defining patterns on a surface can be divided into two categories: those based on the delivery of energy and those based on the delivery of materials. The high-energy light or electron beam is the mainstream in the microelectronics community while material printing is more popular in biological context where the materials of interest are chemically diverse and sensitive to harsh conditions. The recently developed cantilever-free scanning probe arrays have spanned this divide, in which either materials or energy can be deposited from the pyramid-shaped tips rest on an elastomeric support. Given the widespread usage of energy delivery techniques, beam pen lithography (BPL), in which the elastomeric pyramid arrays are converted into near-field probes to direct light onto a surface, not only provides a powerful mask-free nanofabrication schema in a massively parallel and multiplex fashion,[11, 219] but also arouses the interest in nano-confined photochemistry.[243]

The key component in BPL is the opaque metal-coated pyramid arrays with sub-wavelength apertures opened at each tip. Through gentle contact with the substrate and the use of apertures to confine the light pathway, the pen array is endowed with the capability to break the diffraction limitation and pattern features as small as 100 nm in the near-field operation. While it is straightforward to fabricate cantilever-free pen arrays composed of elastomeric pyramids, several groups have developed methods for fabricating aperture arrays based on metal[219, 244] and carbon black[245] opaque layers following the original demonstration of BPL.[11] However, from a practical standpoint, requiring apertures brings a limitation as this is the part of the pen array fabrication process that is most sensitive to processing conditions and can result in non-uniform apertures. Although near-field photolithography has also been demonstrated using pyramid arrays coated uniformly in chromium,[246] these predominantly opaque pen arrays have limited utility for the delivery of materials as the rigid metal coatings physically block the elastomer and cannot be reversibly deformed, properties that diminish the use of elastomeric tip as ink reservoir to mediate molecular patterning[247] and prevent one from toggling ink transport by altering contact force,[10, 204, 215-216, 248] respectively. Therefore, the only demonstration of using aperture-based BPL for patterning materials and light involves matrix-assisted deposition of materials and far-field light illumination in subsequent steps.[243] Interestingly, one can question the need for an opaque film on the pen as early work by the Whitesides' group has shown that transparent PDMS pyramids can support total internal reflection on the faces of such pyramids, which in some cases can lead to light being directed out the top surface of the pyramid array.[249-250] Based on these observations, we proposed that cantilever-free scanning probe arrays with no opaque coatings on the pyramidal pens can effectively deliver optical energy together with the molecular printing capability, which could enable one to control surface reactions with combined approaches based on light, contact force, and material transfer.

Here we explored the optical implications of not having opaque films or apertures at the tip of pens in a cantilever-free pen array and found that by simply blocking the flat backing layer between pens, the optical interaction with the surface is dominated by the light at the tip of the pen, allowing one to serially write sub-wavelength features. Furthermore, without a rigid metal film coating the pens, the elastomeric pens can be reversibly deformed to tune the illumination region from submicrometer to micrometer scale and can afford simultaneous delivery of optical energy and materials in a single experiment; thereby providing multiplexing of length-scales for patterning.

6.2. Experimental

6.2.1. Fabrication of Apertureless Pen Arrays

Polymer pen array made of hard polydimethylsiloxane (*h*-PDMS) was treated with O_2 plasma at 150 mTorr and 45 W for 1 min. Next, an opaque coating of 5 nm Ti and 200 nm Au was evaporated onto the pen array using an electron-beam evaporation system (Kurt J. Lesker Co., USA). To expose the transparent pyramidal tips, poly(methyl methacrylate) (PMMA950 A3, MicroChem Inc., USA) was spin-coated onto the tip array at 1000 rpm for 45 s followed by baking at 100 ℃ for 10 min. The PMMA coating was repeated for one more time to ensure complete coverage. Finally the pen array was immersed in a Au etching solution (Gold Etchant TFA, Transense Company Inc., USA) for 70 s followed by Ti etching (Titanium Etchant TFT, Transense Company Inc., USA) for 5 s to remove the metal coatings on the pyramids while maintaining the backplane between pens opaque.

6.2.2. Lithography Procedure

Typically, an n-type <100> silicon wafer was spin-coated with a 450 nm thick layer of positive photoresist (Shipley1805, MicroChem Inc., USA) at 4000 rpm for 45 s followed by soft-baking on a hot plate at 115˚C for 1 min. For lift-off processing, a layer of lift-off resist (LOR 1A, MicroChem Inc., USA) was spin-coated at 4000 rpm for 45 s and then baked at 180 ˚C for 5 min.

Subsequently, the pattern resist was spin-coated using a pre-diluted photoresist solution with propylene glycol monomethyl ether acetate (MicroChem Inc., USA) at 1:1 v/v for 100 nm thick layers and 1:3 v/v for 40 nm thick layers. Apertureless pen arrays were mounted onto a BPL apparatus and leveled to the photoresist-coated substrates optically. Patterns were generated under the control of piezoelectric actuators of a scanning probe platform (XE150, Park Systems) and a commercial digital micromirror device (DMD – DLP LightCommander, Logic PD) coupled with a collimated 440 mW 405 nm LED light source (M405L2, Thor Labs USA) to allow the exposure time between 1 and 10 s. After patterning, the photoresist was developed in MF24A (MicroChem Inc. USA) for 20-30 s and rinsed with DI water. A layer of 2 nm Cr and 10 nm Au was evaporated onto the developed samples followed by etching of polymer resist in Remover PG (MicroChem Inc., USA) overnight. Patterns of photoresist and metals were characterized using optical microscopy (Axiovert-Zeiss), atomic force microscopy (Dimension Icon, Bruker), and scanning electron microscopy (S-4800-II, Hitachi).

6.2.3. Photochemical Printing

The ink for photochemical patterning was prepared by mixing Rhodamine-modified thiol (1 mg mL^{-1}), photoinitiator 2,2-dimethoxy-2-phenylacetophenone (0.3 mg mL^{-1}) and glycerol (50 mg mL^{-1}) in ethanol. Then the ink was spin coated onto the plasma-treated pen array (2000 rpm, 30 s). The piranha-washed Si wafers were immersed into the solution of 10-undecenyl trichlorosilane (1% v/v in toluene) for 2 h to form an alkene-terminated surface. The inked tip array was mounted onto the scanning head, leveled and brought into contact with the alkene-modified substrate under simultaneous UV illumination (365 nm, 150-200 mW cm^{-2}) from Hg lamp, with illumination time ranging from 1 to 4 min. After patterning, the substrate was sonicated in ethanol for 30 min and blow dried with nitrogen. Patterns were characterized using fluorescence microscopy (λ_{ex}= 537-562 nm, λ_{em}= 570-640 nm).

6.2.4. Simulations

Ray tracing simulations of light normally incident on a pen array was conducted using Persistence of Vision Raytracer Pty. Ltd. Finite-difference time-domain (FDTD) simulations were performed with a commercial package (Lumerical FDTD solutions v.8.7.0). The refractive indices of photoresist and PDMS pyramid were assumed to be 1.66 and 1.43. FDTD was run with purely pyramid structures. Due to the computation limitation, the pyramid size in the simulation was reduced to 8 µm. Perfectly Matched Layers (PML) boundary condition was used to absorb the electromagnetic fields at the simulation boundary. The Total Field Scattered Field (TFSF) plane wave source was used to avoid the light interaction with simulation boundary. The light polarization was paralleled to the edge of the pyramid. The spectral profile of the light source (LED) was addressed by averaging the intensity profiles over spectral range of the light source with the spectral line shape as the weighting factor.

6.3. Results and Discussions

6.3.1. Principle and Preparation of Apertureless Pen Arrays

In order to explore the optics for serial writing with apertureless pens, we considered the paths through which light can propagate through an elastomeric pyramid. In observing an elastomeric pyramid from the top, it is clear from the varying contrast in different regions that light incident on different areas is directed in different ways (Figure 6.1A). Through ray tracing simulations of light normally incident on a pen array (Persistence of Vision Raytracer Pty. Ltd.), we determined that there are four distinct optical paths that may play a role in

BPL (Figure 1A): a) light that is directed to the vicinity of the tip, b) light that is incident on flat faces of the pyramid near their centers, c) light that is incident on the flat faces of the pyramids near their edges, and d) light that is incident on the flat backing layer. The central requirement for effective BPL is that the light path a) dominates the delivery of optical energy to the surface. In order for this to be true, all other light paths must be somehow marginalized. Fortunately, the light path b) internally reflects once in the pen and then leaves via the opposing face at a 24 °angle with respect to the surface. This steep angle serves to diffuse this light broadly across the photosensitive surface. In contrast, the light path c), which accounts for ~40% of the light illuminating the pyramid, internally reflects twice in the pen and then leaves via the opposing face at a 2 ° angle, moving vertically away from the photosensitive surface. Finally, the light path d) is directly transmitted to the photosensitive surface. Since light of this kind would represent an uncontrolled background illumination, it must be blocked for reliable scanning optical lithography to occur. These optical calculations led us to hypothesize that by simply blocking the flat backing layer (light path d), we may effectively deliver optical energy predominately at the apex of an apertureless pen by virtue of the self-light-focusing nature of the PDMS pyramid.

Based on this principle, we fabricated cantilever-free pen arrays with an opaque coating on the backing layer, but not on the sidewalls of the pyramidal pens (Figure 6.1B). Notably, this procedure is significantly less complex than known procedures that produce apertures. Hard PDMS arrays of pyramids with 30 μm base widths and 100 μm pitch were produced according to previously published protocols. In order to render the backing layer opaque, pen arrays were coated with 5 nm Ti/200 nm Au and subsequently spin-coated with a protective layer of PMMA. Importantly, we found that at specified PMMA concentrations and spin speeds, the PMMA coated the backing layer but not the pens themselves, allowing us to use chemical etching to remove the opaque coating on the pyramidal pens (Figure 6.1B and C, see experimental details in

Section 6.2).

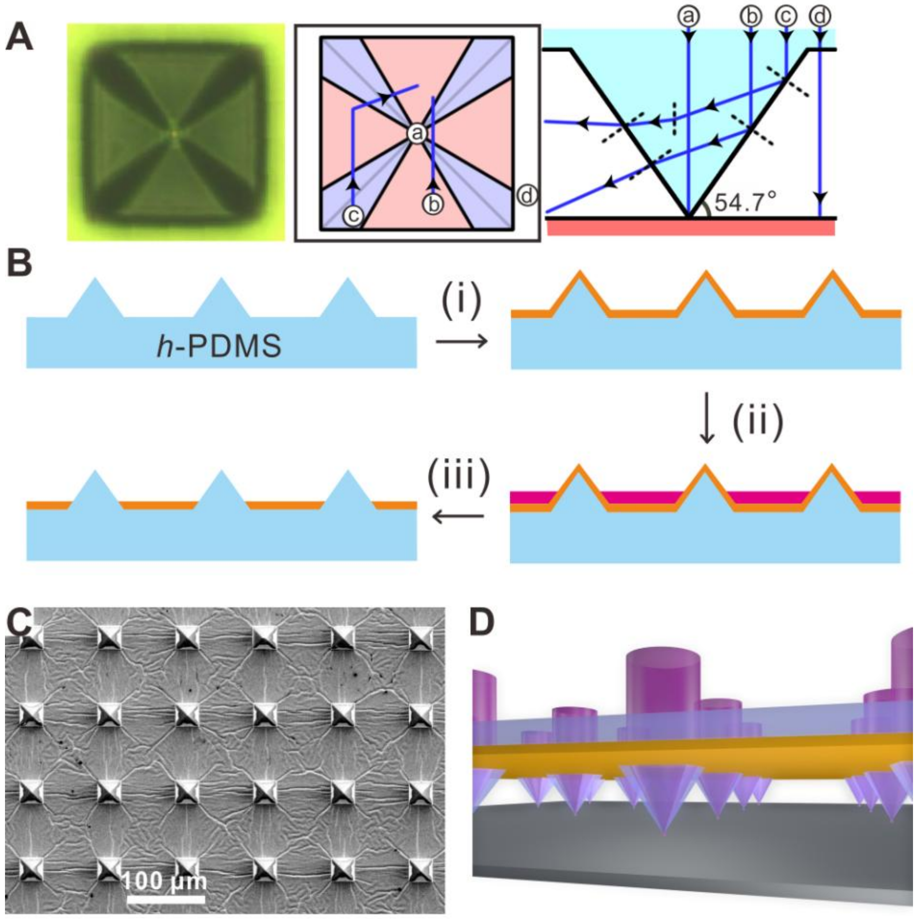

Figure 6.1. Principles and fabrication of apertureless cantilever-free pen arrays. (A) Optical microscope image and schematic illustration showing the four light paths present when elastomeric pyramids are illuminated. These suggest that if the light incident on the back layer could be blocked, light at the tip of the pen will dominate the optical interaction with the surface. (B) Schematic of the fabrication of the apertureless BPL pen arrays: (i) evaporation of 5 nm Ti and 200 nm Au on hard polydimethylsiloxane (*h*-PDMS) pen arrays; (ii) spin coating of PMMA that only covers flat region of the pen array; (iii) chemical etching of metal layer followed by removal of PMMA. (C) Scanning electron microscopy (SEM) image of the as-fabricated apertureless pen arrays. (D) Schematic of scanning optical lithography using the apertureless cantilever-free pen arrays.

6.3.2. Scanning Optical Lithography on Photoresist

In order to quantify the propagation of light through the self-light-focusing tips, we performed lithography experiments on polymer photoresist. The apertureless elastomer pen array was mounted on a scanning probe system (XE150, Park Systems) and leveled with respected to a patterning substrate pre-coated with a 450-nm-thick positive-tone photoresist. Subsequently, the pen array was brought into contact with the surface and illuminated from the back side for a specified time (λ = 405 nm). The light was guided to individual pens using a digital micromirror device.[219] Importantly, this apparatus allowed us to independently control the location of the pen array, contact pressure, and illumination time. Following exposure to light, treating the photoresist with a developer caused the photoresist that had been exposed to dissolve, effectively leaving a physical remnant of the light intensity profile. As an initial experiment, we exposed a 7 × 3 dot array with 5 μm pitch to 4 s of light with a relative Z-piezo extension (Z_{ext}) that gradually increased from 0 to 6 μm in each row. After developing the photoresist, we observed a large region of uniform duplicates of this dot array pattern, and the background areas without contacting with the tips were unexposed, in agreement with our expectation that each pen in the 20, 000 pen array would generate a copy of the pattern (Figure 6.2A). The nanoscale morphologies of the features in these patterns were characterized by atomic force microscopy (Figure 6.2B). As Z_{ext} was increased from 0 to 1 μm, the size and shape of the exposed region did not change significantly and the developed regions corresponded to roughly circular holes ~400 nm in width (full width at half maximum) with maximum depths of ~200 nm, indicating no significant tip deformation owing to the buffering of the soft bulk PDMS layer.[10] It should be also noted that as the tip was slightly elevated for 0.5-1 μm, holes with similar size and shape were still formed, but the depth was only less than half of those written at initial contact. The depth difference can be attributed to less energy loss in the near-field regime upon tip contact due to lack of scattering/reflection at the interfaces created by air gap. These observations prove that the light self-focused on the tip apex (optical paths a) dominates the optical interaction with the photoresist surface and that light exiting through the faces (optical paths b and c) does not contribute significantly to the light intensity on the patterning surface.

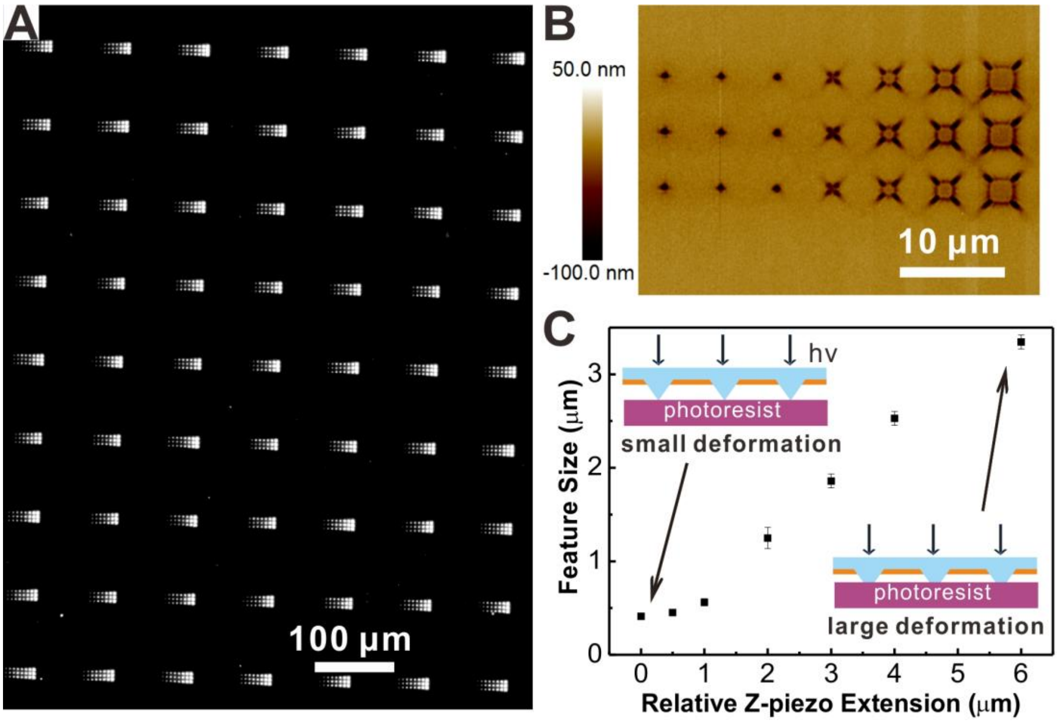

Figure 6.2. Force dependence in photoresist patterns generated with an apertureless cantilever-free pen array. (A) Dark field optical microscope image of a large region of developed photoresist patterns. Each 7 × 3 array of dots is written by a single pen under same exposure dose but with a z-piezo extension that increases from left to right. (B) Tapping-mode AFM image of a typical dot array showing the change in size and shape with increasing z-piezo extension from left to right. (C) Average size of features written at varying z-piezo extension.

In molecular printing with elastomeric pens, the force-dependent patterning with an extension sweep has been extensively studied.[10, 204] While a metal-coated BPL pen array cannot be compressed without plastic deformation of the metal, since the apertureless pens are composed entirely of an elastomer, the reversible tip deformability can give rise to a variable amount of optical energy delivered to the surface. Specifically, by increasing Z_{ext} from 1 to 6 µm, the shapes of the exposed feature were found to change from round dots to squares with the four protruding corners. The reversible change in feature size (the rows were written one at a time) illustrates that applied pressure can dictate the region that is exposed to light. It is important to note that this result is in contrast with aperture-based BPL where features larger than a micron take prohibitively long to pattern due to the rapid decay of near-field light. Rather than being restricted to a fixed aperture, the elastomeric pens are effectively behaving as having variable apertures as defined by refractive optics.[249-250] The feature size of these protruding squares increased from 0.56 ± 0.04 μm to 3.35 ± 0.07 μm as a linear function of Z_{ext}, showing the similar force dependence as that in PPL (Figure 6.2C). Interestingly, the light intensity was observed to have uneven distribution, where the central area is much less affected compared with the corner and edge areas of the square shape and the four corners exhibit the highest depth value. The observation can be analogous with the molecular printing results in PPL, and the elastic deformation of tip is believed as the main cause.

The exposure time was also investigated to tuning the patterned features. A series of 4 × 2 dot arrays were fabricated with exposure time varying from 1 s to 10 s, while increasing Z_{ext} from 0 to 6 μm in each array (Figure 6.3A-C). For those dot features written at initial contact, the feature size presented a linear increase with the exposure time from 294 ± 35 nm to 840 ± 33 nm (Figure 6.3D). Interestingly, at short exposure time, light focusing on the tip apex resulted in deep penetration in the dot features, while the intensity is distracted to four corners and most of the central regions within the square-shaped tip contact area maintained undeveloped. As exposure time prolongs, the corner, edge and central regions of the square patterns were sequentially filled with minimal loss of optical confinement. The increased aperture area has caused increased dosage delivered to the resist. We used the photoresist depth profile to estimate the irradiation dose. The volume of the developed photoresist shows a linear increase as the degree of tip deformation increases after 10 s exposure (Figure 6.3E), indicating the increase in the total irradiation dosage on the surface, which is in accordance with previous report. Furthermore, through the linear function between the fraction of photoresist remaining thickness and the exposure time (Figure 6.3F) and assumption that the dose is 50 mJ/cm^2 at fraction=0, we calculated the time for totally expose a 500-nm S1805 photoresist and the optical intensity in the center as 3.3, 4.4, 1.5, 1.5 mW/cm^2 for Z_{ext}=0, 2, 4, and 6 μm, respectively. Although the tip shows enhanced intensity at small deformation, these square features at high deformation could still be reliably used for lithography. The maximum depth generated in each features were plotted with exposure time and Z_{ext} (Figure 6.3G) to provide a guidance to adjust the contact force, exposure time and photoresist thickness for lift-off process.

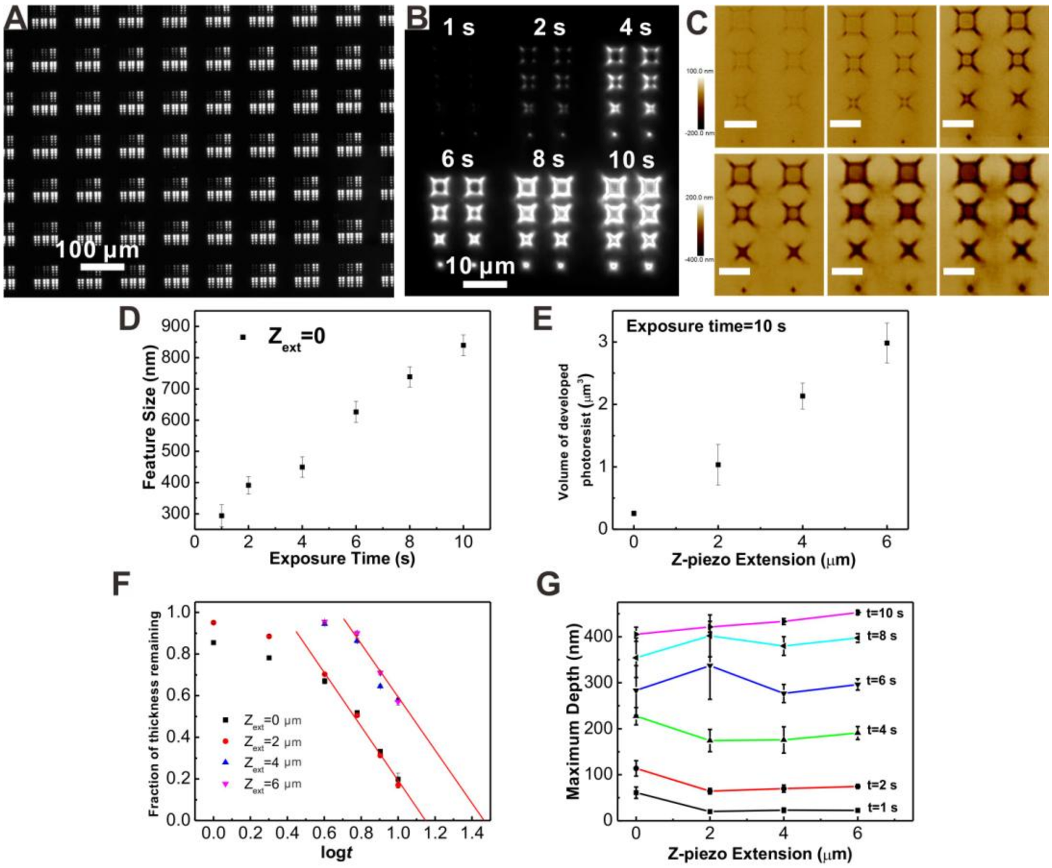

Figure 6.3. Effect of exposure dose on the photoresist patterns generated with an apertureless cantilever-free pen array. (A&B) Dark field optical microscope images of a large region of developed photoresist patterns by varing exposure dose (A), and one typical array of dots produced with varied exposure time from 1 to 10 s and Z_{ext} of 0, 2, 4 and 6 μm from bottom to top row. (C) Tapping-mode AFM images of the patterned dot arrays shown in (B). Scale bars: 5 μm. (D) Plot of feature size at initial contact with exposure time. (E) Plot of volume of developed photoresist versus z-piezo extension. (F) Plot of fraction of remaining thickness in the center of patterns versus the logarithm of exposure time. (G) Statistic results of maximum depth in photoresist patterns with the exposure time and the z-piezo extension.

To further understand the optical phenomena contributing to the observed patterns, FDTD simulations were performed with a commercial package (Lumerical FDTD solutions v.8.7.0). The refractive indices of photoresist and PDMS pyramid were assumed to be 1.66 and 1.43. Due to the computation limitation, the size of pyramid base in the simulation was reduced to 8 μm. We obtained the intensity distribution in the photoresist using tips with square cross section and edge size of 0.2, 1.2 and 3.2 μm, respectively. Overall, a good agreement was found between the simulational (Figure 6.4) and experimental results (Figure 6.2 and 6.3) on less deformed tips. The light illuminating from the tip base is highly concentrated at the tip apex owing to the pyramidal shape, with an intensity of ~7×10^4 times higher than that in the background. Also the calculations suggest that the light at the tip is ~7 times more intense than the incident light. Due to the interference caused by the tip surface and the bottom layer of photoresist, periodic intensity modulation is observed in all three dimensional directions. The cross-sectional profiles also point out that the penetrated light in the photoresist shows higher intensity in the dot feature than the square feature at the same depth, which is consistent with the observations on exposure time. However, the spatial distribution of light at high levels of tip deformation is neither reproduced by FDTD nor ray tracing simulations, leading us to attribute the interesting light patterns to a complex deformation of the elastomeric tips. These fascinating shapes could be studied by coupled mechanical-optical simulations and could even be used as a diagnostic to learn about tip deformation.

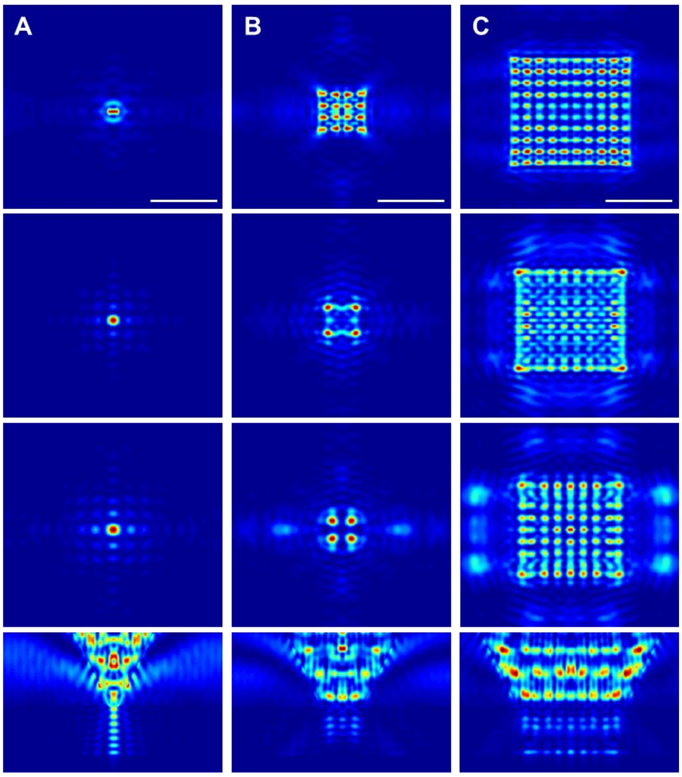

Figure 6.4. Near-field intensity profiles generated by FDTD simulations. (A) From top to bottom: intensity profiles at horizontal planes at the top, in the middle and at the bottom of photoresist and at a vertical plane. The tip size is 0.2 µm. (B-C) The same information as (A) for the tip sizes of 1.2 and 3.2 µm. Scale bar: 2 µm.

6.3.3. Generation of Gradient Au patterns

Since a standard application of photolithography is the generation of metallic features using a lift-off process, generation of Au patterns was demonstrated through the same lithographic approach using apertureless pen arrays. In evaluating this, we also took advantage of an important capability of the elastomer pen array in the context of molecule printing wherein by slightly tilting the pen array with respect to the pattern surface, one can rapidly create a gradient in feature sizes from nanometer to micrometer length scales.[205] Since the light propagation through the deformable tip can be force-tunable in a wide range, the tilting approach would also apply to the apertureless pen array (Figure 6.5A). As proof-of-concept, we performed a lithography experiment on a substrate coated with a polymer bilayer of 100 nm photoresist atop a 150 nm lift-off resist. Each pen was programmed to write a 8×8 dot array (pitch=7 μm) with 2 s exposure time, and the tilt was chosen such that the tip-substrate distance was varied by 6 μm across the ~0.5 cm pen array (~0.07°). After developing the resist, evaporating 2 nm Cr and 10 nm Au, and subsequently removing the polymer using a chemical etch, Au features were obtained with a size gradient ranging from ~ 3 μm to ~400 nm along the ~0.5 cm distance. From optical and SEM images of typical Au pattern arrays selected from 3 regions in one direction (Figure 6.5B), the Au patterns gradually change from square shapes to round dot, with the average size of 2.91±0.12 μm, 1.48±0.07 μm and 0.41±0.09 μm, respectively. Interestingly, by choosing thinner photoresist films and shorter exposure times, hollow square features and isolated Au features as small as 250±30 nm were generated (Figure 6.6A and B). In addition, continuous lines were also made by writing dot patterns with pitches smaller than their feature size (Figure 6.6C). For instance, Au patterns consisting of lines with width of 400 nm, 2 μm and 8 μm were produced, in which the Z_{ext} was set as 0, 2, and 4 μm to write pixels with approximate size of 400 nm, 1 μm and 2.5 μm, respectively. These patterning results suggest that the apertureless elastomer pens can be used for a variety of micro- and nanofabrication tasks and combinatorial screening.

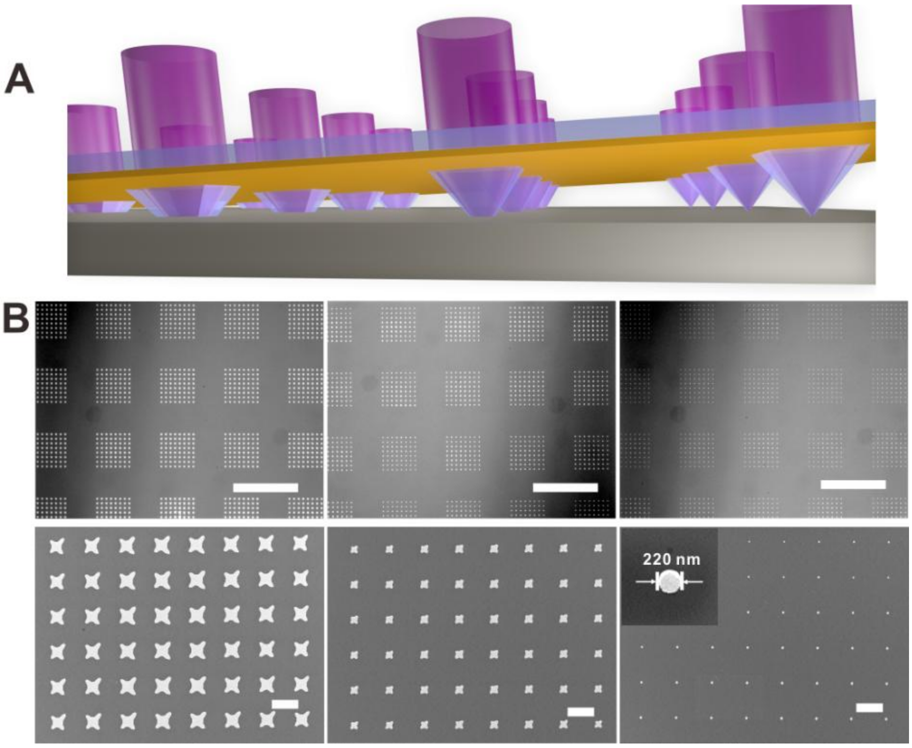

Figure 6.5. Generation of feature gradients with force-tuned size and shape. (A) Schematic of a tilted lithography experiment using apertureless pen arrays. (B) Representative dark-field optical microscope and SEM images of Au dot arrays generated at the left, middle and right edges of a ~0.5 cm wide pen array. Here, the average sizes were 2.91 ± 0.12 µm, 1.48 ± 0.07 µm and 0.41 ± 0.09 µm from left to right. Scale bars are 100 µm and 5 µm, respectively.

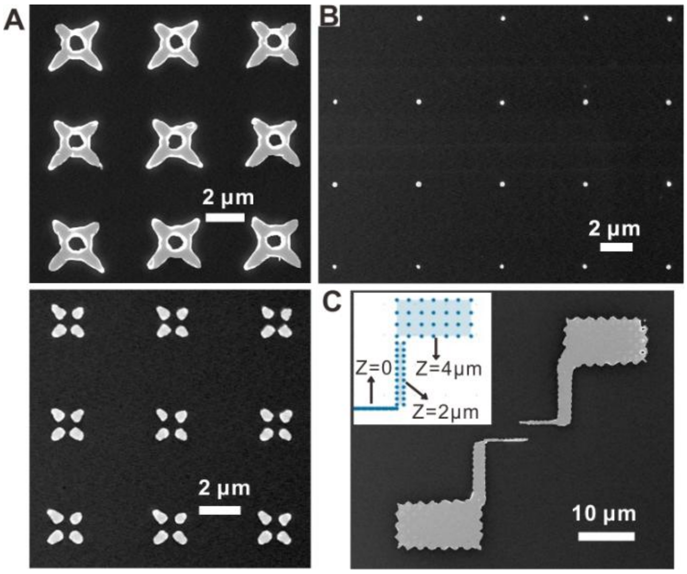

Figure 6.6. (A-B) SEM images of Au patterns arrays fabricated with 40 nm photoresist and 150 nm lift-off resist. By adjusting Z_{ext} and exposure time, we obtained Au features with various shapes (A) and dot arrays with average size of 250±30 nm (B). (C) Au lines patterned by adjusting Z_{ext} to write pixels with different sizes.

6.3.4. Photochemical Printing by Apertureless Pen Array

Having shown that apertureless cantilever-free pen arrays can be used to effectively pattern light on a photosensitive surface, we evaluated ability to use these arrays to combine molecular printing and the delivery of optical energy. To this end, we used thiol-ene photo "click" chemistry[243, 251] to pattern a thiol molecule modified with fluorescent Rhodamine B dye onto an alkene-functionalized surface (Figure 6.7A). Prior to patterning, the apertureless pen array was spin-coated with a mixture of the fluorescent thiol, 2,2-dimethoxy-2-phenylacetophenone (DMPA) as photoinitiator and glycerol as high-viscosity liquid matrix. Then, the inked pen array was brought into contact with the alkene-terminated Si substrate to write a 4 × 3 dot array while the pen array was illuminated by UV light (365 nm, 150-200 mW cm^{-2}) to induce local surface photo-click reactions. In order to study the effect of illumination, the dwell time was varied between 1 and 4 min, and a column of 4 dots was also printed with the same dwell times but no illumination as a control. After patterning and subsequently sonicating the substrate in ethanol for 30 min, we characterized the samples using fluorescence microscopy (Figure 6.7B, λ_{ex}= 537-562 nm, λ_{em}= 570-640 nm) and found that the fluorescence intensity gradually increased with dwell time (Figure 6.7C and D), while the control dots showed very little fluorescence and did not change intensity with dwell time, as expected.[243] These results confirm that the apertureless PDMS pen can be used to simultaneously print molecules and drive a chemical reaction with light. In contrast to PPL, we did not observe spurious dots from incidental contact during leveling or a diffusion-controlled feature size owing to the efficient light confinement at the tip. It should also be noted that while the optical intensity profile is not isotropic at high deformation, all features observed in this experiment were round, which we attribute to the feature shape being defined by molecule printing in addition to confinement of light. This raises the interesting possibility of using a combined molecule-light based approach to define uniform features that would be smaller than either technique alone.

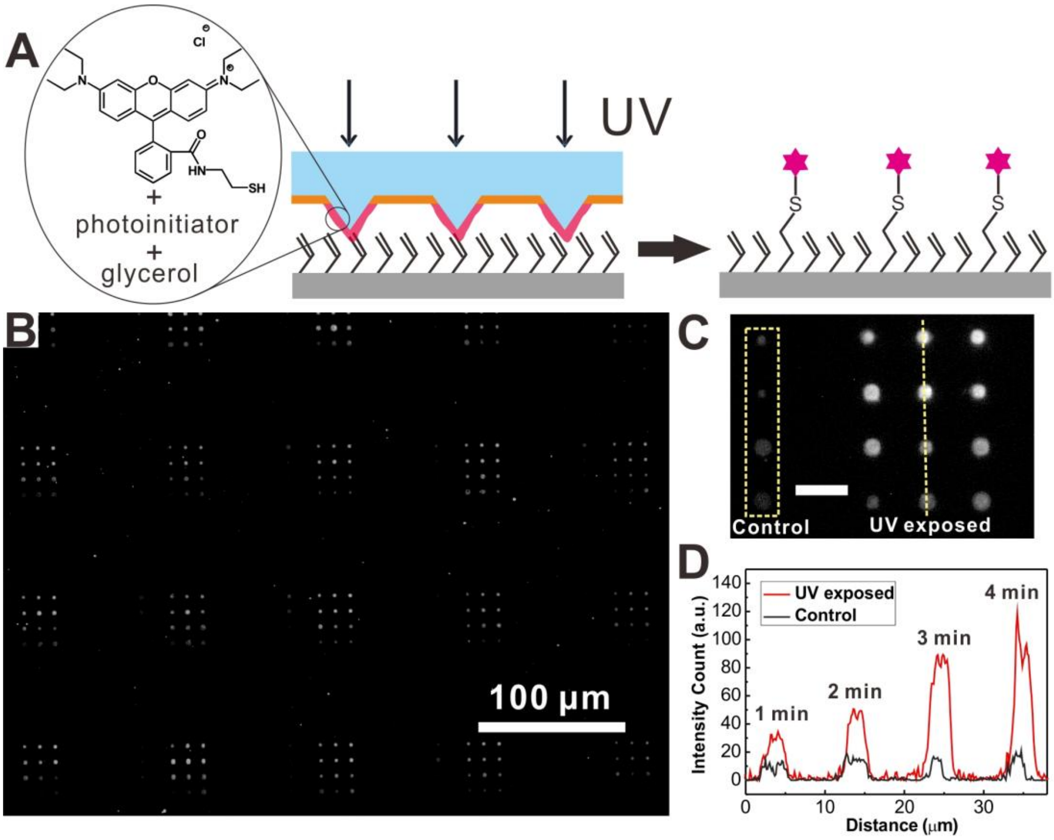

Figure 6.7. Simultaneous delivery of optical energy and materials. (A) Schematic of photochemical printing of Rhodamine-modified thiol inks by thiol-ene photochemistry. (B) Fluorescence microscope image (λ_{ex}= 537-562 nm, λ_{em}= 570-640 nm) of the patterned 4 × 3 arrays with illumination times of 1, 2, 3, and 4 min from bottom to top rows by apertureless pens. (C) Fluorescence microscope image of an array patterned by a single pen, showing dots with (right 3 columns) and without (left 1 column) UV illumination. Scale bar: 10 µm. (D) Intensity profiles of the patterned features with different illumination times as well as the control group, indicated by the dotted lines shown in (C).

6.4. Conclusions and Future Outlooks

In this chapter, we have shown that how the photoreactive polymer surface can be patterned by optical energy delivered from the cantilever-free pen array.

Photopatterning by Apertureless Pen Arrays

Due to the fascinating optical and mechanical properties of elastomeric pyramids, it is possible to locally control the chemical and optical environment of a nanoscopic region on a surface in a manner that allows for the simultaneous delivery of materials and energy. An apertureless cantilever-free pen array has been developed for such purpose by passivating the flat backing regions between the transparent elastomeric pyramids with opaque metal coating. Since lithographic tools are evaluated in part based on their versatility and ease of use, given the simplicity of the pen arrays used here, this approach is expected to become very important for a wide range of applications that require features greater than or equal to ~200 nm, with the ability to control surface chemistry by light, contact force, and material transfer. In addition to providing insights into the optics and mechanics of nanoscale elastomeric systems, we expect this technique to significantly lower the barrier to entry to researchers interested in performing rapid prototyping and combinatorial chemistry. Following the apertureless pen concept, multiplexed surface patterns can be envisioned by combining the pen array with multiplexed printing or actuation techniques.[211, 219] And the apertureless tip structure would allow more functionality by coating with functional materials on the tip.

CHAPTER 7

DEVELOPMENT OF DUAL-ELASTOMER TIP ARRAY FOR SCANNING PROBE LITHOGRAPHY

In previous two chapters, the 2D polymer pen arrays have been shown to control the feature size by tuning contact force, and to generate large-scale gradient features in a simple and rapid manner, either in molecular printing or optical lithography. However, the easy deformation of the elastomeric tip has also restricted their potential in high-resolution patterning with high uniformity. In this chapter, a well-engineered tip structure is invented to address the uniformity challenge by reducing the degree of tip deformation.

7.1. Introduction

The key advantage of the elastomeric tip array used in cantilever-free scanning probe lithography is that the feature size is dependent on the tip-substrate contact area which can be readily adjusted by the force applied on the pen array due to elastic deformation.[10, 204, 248] Therefore, one can fabricate patterns spanning from ~100 nm to tens of micrometers over large areas rapidly. The “force-dependent” nature, however, has also created a great challenge at the same time for researchers to make uniform and precise features over large areas, which is vital if one would like to develop a low-cost “desktop nanofab” tool. The reason is that the tips of one tip array are difficult to simultaneously contact the underlying substrate. On one hand, it is very difficult to align the polymer pen array perfectly parallel to the underlying substrate. Previous works have shown that the best optical leveling technique cannot resolve a titling angle less than 0.02^{o}, i.e., ~3 µm difference in height across 1 cm.[204, 206] On the other hand, the heights of the pyramidal tips of one tip array exhibit a random variation of 0.5 to 2 µm, which is a typical resolution limit as a consequence of photolithography, wet etching and resist curing procedures involved in the tip fabrication process. As a result, some tips inevitably contact the substrate surface earlier and deform more than the others when the tip array is pressed against the underlying substrate. Efforts made to address the challenge include the development of "force feedback" sensor arrays for high-precision leveling and the quality improvement of the tip fabrication.[206, 217] Other hard materials such as silicon and polymers have been explored to fabricate tip arrays as well. Nevertheless, these methods substantially increase the equipment and fabrication costs of polymer pen array, require specialists, and are only applicable to certain types of scanning probe systems, which hamper the accessibility of polymer pen array to researchers in wider physical and life science communities.

Alternatively, we herein advocate a simple, low-cost, yet effective material-based approach, different from the aforementioned machinery efforts, to significantly improve the uniformity and precision of PPL. The key innovation is that, instead of using a homoelastomer as the tip material in traditional polymer pen arrays, a pair of hard and soft elastomers is used to fabricate the tips. This dual-elastomer tip array consists of a hard elastomer as the apex of the tips and a soft elastomer as the base of the tips as well as the backing layer on glass (Figure 7.1A). The soft elastomer serves as cushion to absorb part of the mechanical force applied on the hard apex, and the variation of tip-substrate contact size induced by the unevenness of tip-substrate distance can be dramatically reduced. Therefore, the hard-apex, soft-base structure of the dual-elastomer tip array can effectively improve the feature uniformity made by different writing tips, while maintaining the advantages of low-cost fabrication by mould replication and the force-dependent feature of PPL. We show in our mechanical simulation that use of hard-soft elastomer pair in the tip can effectively decrease the patterning deviation and improve uniformity. To the best of our knowledge, this is the first study on the tip arrays of a scanning probe that are made of one pair of hard and soft elastomers.

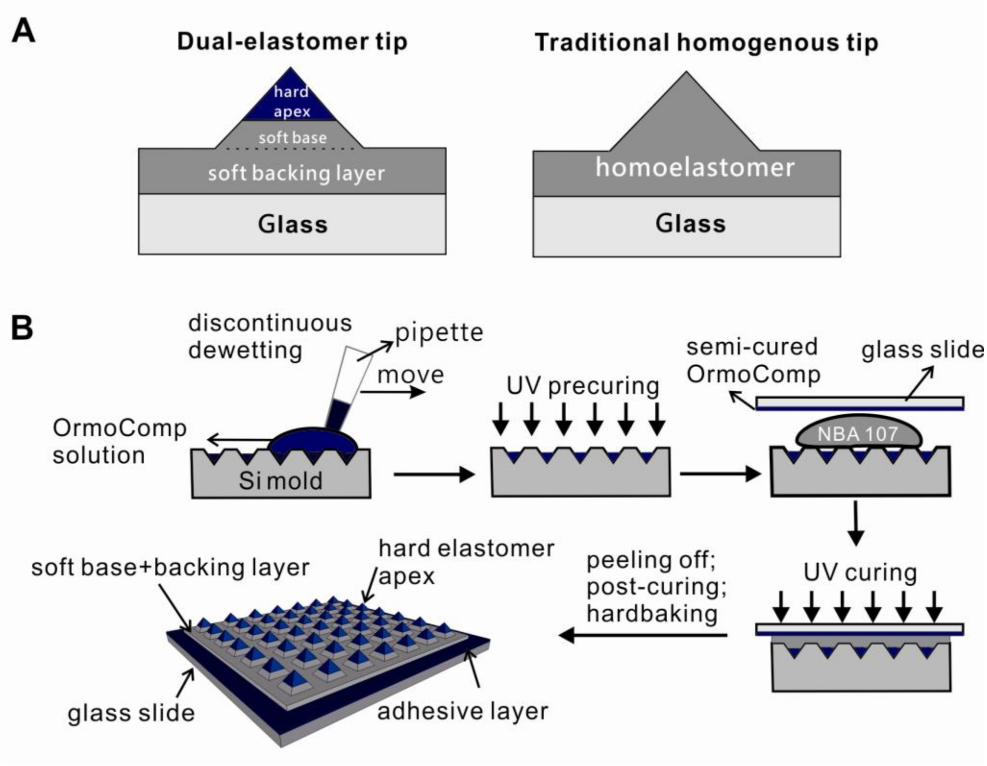

Figure 7.1. Schematic illustrations of (A) the structures of dual-elastomer tip and traditional homoelastomer tip, and (B) the fabrication process of dual-elastomer tip array.

7.2. Experimental

7.2.1 Pretreatment of Glass Substrate

Glass slides were cleaned by ultrasonication in acetone and isopropanol for 10 minutes, respectively. OrmoComp (Micro Resist Technology GmbH) solution was prepared by diluting with OrmoThin (Micro Resist Technology GmbH) in a ratio of 1:3 in weight. An adhesion promoter OrmoPrime08 (Micro Resist Technology GmbH) was first spin-coated on the plasma-treated glass substrate at a speed of 4000 rpm for 60 s followed by baking on hot plate at 150 ℃ for 5 min. Subsequently, diluted OrmoComp was spin-coated on the pretreated glass at a speed of 3000 rpm for 30 s. Finally, the glass substrate was placed under UV lamp (365 nm, 2 mW/cm^2) for 2 min to obtain the semi-cured OrmoComp as an adhesive layer.

7.2.2 Fabrication of Dual-Elastomer Tip Arrays

Discontinuous dewetting was employed to deposit OrmoComp inside the microwells first. A droplet of OrmoComp solution was placed on the mould and was quickly pulled with a pipette to move through the whole area of the mould. After evaporating the solvent in the air for 30 min, OrmoComp was pre-cured by UV exposure (365 nm, 2 mW/cm^2) for 2 min. Subsequently, one droplet of NBA 107 (Norland Product, Inc., USA) was poured on the mould with the pretreated glass slide covered on top. The whole assembly was placed under UV lamp for 3 minutes for curing. Afterwards, the semi-cured pen array was carefully separated from the mould and underwent a post-curing of 3 min and hardbaking at 130℃ under vacuum for 10 min to obtain the fully cured dual-elastomer tip array, which was characterized by optical microscope (Nikon eclipse 80i), SEM and EDX (JSM-6335F).

7.2.3 Polymer Pen Lithography (PPL)

Au substrate with thermally evaporated 5 nm Cr and 25 nm Au on Si <100> wafer was cleaned by ultrasonication in DI water, acetone, isopropanol sequentially and were blown dry with N_2. Hexamethyldisilazane (HMDS) modified Si wafers was prepared by vapor silanization at 60 ℃ for 15 min. The dual-elastomer tip array was treated by O_2 plasma for 60 s before inking. The tip array was inked with 16-mercaptohexadecanoic acid (MHA, Sigma-Aldrich) by immersing in a 10 mM MHA ethanol solution for 10 min, followed by rinsing with ethanol and blown-dry. Inking with polyethylene glycol (PEG, M_w=4,000) or PEG/Rhodamine B mixture were conducted by spin coating of 0.5 mL acetonitrile solution (5 mg/mL PEG, 5 mM Rhodamine B) at 2000 rpm for 2 min on the tip array. Subsequently, the inked dual-elastomer tip array was attached to a customized probe holder of an atomic force microscope (AFM, XE-100, Park

Systems), leveled optically against the underlying substrate by the built-in tilting stage of XE-100 AFM, and brought into contact with the substrate to generate MHA patterns on Au substrate at 45-50% humidity or PEG patterns on HMDS-SiO_2 substrate at 90% humidity. After printing, Au patterns were generated by immersing the Au substrate in an etching solution (20 mM thiourea, 30 mM $Fe(NO_3)_3$, 20 mM HCl, 20 mM octanol) for 3 min, which were subsequently characterized by SEM and optical microscope. The deposited PEG patterns were characterized by optical and fluorescence microscopy (λ_{ex} = 525–540 nm, λ_{obs} = 605–655 nm) and AFM.

7.2.4 Finite-Element (FE) Simulations

The FE simulations were carried out using the commercial package ANSYS™ (ANSYS Inc., Canonsburg, PA, USA). To simplify the analysis, the four-sided pyramidal tip was taken as a cone in the simulation (Figure 7.6A). By following the principle of geometrical similarity, i.e. indenters (or the AFM tips for our case) of different geometries shall produce the same load-displacement response during a mechanical contact as long as they possess the same cross sectional area at the same height, the conic angle was deduced to be ~ 33 degrees according to the original four-sided pyramidal shape. Due to the inadequate information on the profile of the tip apex, different radii of curvature were used to match the simulated feature size (contact diameter) with the experimental data at a series of tip extensions. Finally, the radius of curvature was determined to be ~100 nm, which qualitatively reproduced the experimental observations when the height of the hard apex was chosen to be 30 µm. To maintain the simulation accuracy at a reasonable computational cost, a gradient meshing strategy was used to produce the discrete FE model with the boundary conditions shown in Figure 7.7. The ANSYS Parametric Design Language (APDL) was also used to write a script file for automatically generating the outputs of force, displacement, contact radius as a function of the tip extension.

7.3. Results and Discussions

7.3.1 Preparation and Characterization of Dual-Elastomer Tip Arrays

Three important issues have to be addressed in the fabrication of dual-elastomer tip array: (1) generation of ultrasharp tip (<100 nm tip radius of curvature), (2) optical transparency of the materials, and (3) fine control of the hard-apex, soft-base layered structures. OrmoComp, a UV-curable hybrid polymer, was chosen as the material for the hard tip apex because it is commercially available with excellent properties, e.g. high Young’s modulus of 1.16 GPa, low shrinkage of 5~7 vol. %, optical transparency down to 350 nm, and chemical inertness, which has been widely adopted for sub-100 nm nanofabrication by nanoimprint lithography (NIL) or photolithography. On the other hand, a UV-curable resin, NBA 107 is chosen as the soft material (Young’s modulus of 5.5 MPa) for the base backing layer owing to its good adhesive property. Both hard and soft PDMS materials have also been examined as the soft layer, however, they cannot adhere to the hard material.

The dual-elastomer tip array was fabricated by the sequential UV curing of precursors of hard and soft elastomers against a silicon mould with an array of pyramidal microwells (40 μm edge length, 80 μm pitch). Very importantly, discontinuous dewetting was used to deposit the hard elastomer only in the apex of the microwells.[252] This was achieved by quickly pulling a droplet of OrmoComp solution with a pipette to move through the whole area of the silicon mould, where the solution dewetted from the fluorosilane-treated surface of the silicon mould and a small amount of liquid was trapped in the microwells. After evaporating the solvent in the air for 30 min, OrmoComp was pre-cured by UV exposure (365 nm, 2 mW/cm^2) for 2 min. Subsequently, one droplet of NBA 107 was placed on the center of the silicon mould and a piece of glass slide pretreated with an adhesive layer of semi-cured OrmoComp was covered on top.

Because of the capillary force, NBA 107 automatically filled the rest of the space of the microwells and the gap between the glass slide and the Si mould. The assembly was cured under UV for 3 min to obtain the semi-cured tip arrays. After demoulding, a further 3 min UV curing and a 10 min vacuum baking at 130 ^{o}C were applied on the elastomers to obtain the fully cured dual-elastomer tip array (Figure 7.1B).

The as-made dual-elastomer tip array is transparent to optical light (Figure 7.2A) and consists of ~15, 000 pyramidal tips in 1 cm^2 area, with a tip to tip distance of 80 µm (Figure 7.2C). From cross-sectional scanning electron microscope (SEM), we find that the lateral size of the sharp end of the pyramidal tip is typically 40 nm, and the thickness of the flat soft backing layer and adhesive layer are 145 µm and 11 µm, respectively (Figure 7.2D). The zoom-in optical and SEM images show a clear boundary at the middle of the pyramidal tip (Figure 7.2B and E). Profile scans of the pyramid tip using energy-dispersive X-ray spectroscopy (EDX) reveal that Si element only exists in the apex region within the boundary, which is 18-µm-thick counting from the peak of the pyramidal tip (Figure 7.2E). Considering that the hard elastomer is a siloxane based material and the soft elastomer is a polyurethane based material, the EDX result confirms the successful fabrication of the hard-soft layered structure, in which the hard elastomer forms the apex of the pyramidal tip and the soft material forms the base of the tip, as well as the flat soft backing layer. Notably, the ratio between the hard and soft parts in the tip can be tuned by varying the concentration of the precursor of hard materials.

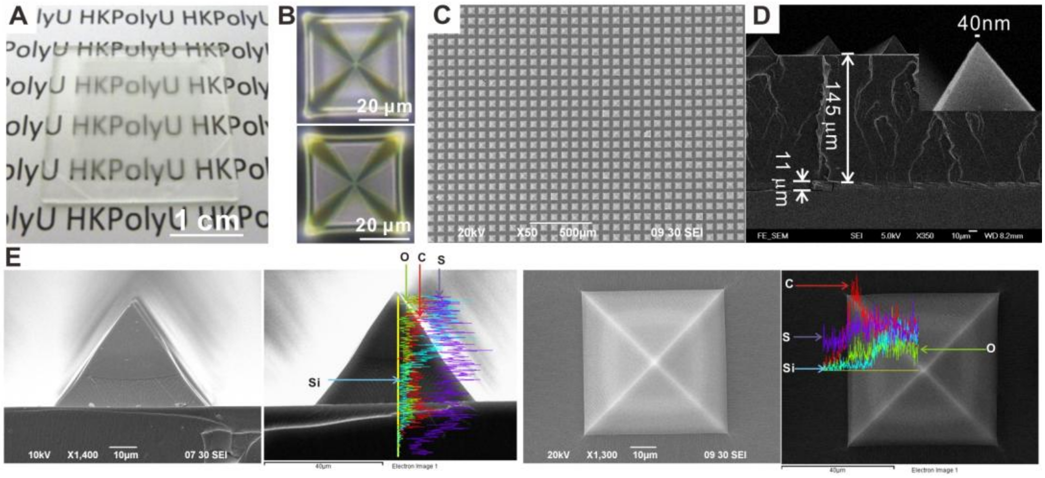

Figure 7.2. (A) Digital image of the transparent dual-elastomer tip array. (B) Zoom-in optical microscope image of a dual-elastomer tip (upper) and a homoelastomer tip (lower), where a clear boundary can be seen in the dual-elastomer tip. (C)Top-view and (D) cross-sectional SEM images of the dual-elastomer tip array. Inset is a zoom-in image of the tip. (E) SEM images and EDX analysis of one tip of the dual-elastomer tip array in cross section and top view.

7.3.2 Printing Small Molecules by Dual-Elastomer Tip Arrays

In order to examine the molecular printing capability, the dual-elastomer tip array was used as a writing pen array for PPL experiments to pattern MHA dots on Au substrates. In a typical experiment, the dual-elastomer tip array was exposed to O_2 plasma for 1 min to render the surface hydrophilic, and then it was inked in an ethanol solution containing 10 mM MHA for 10 min. Subsequently, the dual-elastomer tip array was mounted on AFM, leveled optically against the underlying Au substrate, and brought into contact with the substrate to generate MHA patterns on Au (relative humidity: ~45%). Finally, the MHA-patterned Au substrate was immersed in an etching solution to yield Au patterns, which were observed and analyzed by SEM. To understand the force dependence properties of the dual-elastomer tip array, which is the most essential part of this work, each tip of the dual-elastomer tip array was programmed to pattern a 15 × 15 dot array (pitch = 3 μm), in which the relative Z-piezo extension (Z_{ext}) increases from the bottom row to the upper row gradually from 0 (just contact) to 7.0 µm while the tip-substrate contact time remained constantly at 0.1 s. Figure 7.3A shows the large-area SEM image of the as-made dot arrays over 1.5 × 1.5 mm^2, in which 100% of the tips succeed the patterning. From the zoom-in SEM image (Figure 7.3B), we observe that the feature size is uniform among each row, and it increases as the Z_{ext} is increased. For example, the dot diameter of the bottom row is 0.24±0.04 µm, while that of the upmost row is 1.19±0.02 µm. To quantify the uniformity of the feature within one writing tip, we characterized the dot sizes of the fourth row (counting from the top) in four corners of the whole area. The average diameters are 1.22±0.05 µm, 1.26±0.04 µm, 1.12±0.04 µm, and 1.24±0.03 µm, respectively. These results correspond to that the standard deviation of the feature size written by one tip is less than 5%. The dot diameters are plotted as a function of the Z_{ext} (Figure 7.3C). At the first 0.5-µm Z_{ext} range, the dot diameter increases rapidly from 236±36 nm to 656±10 nm, because of the large stress on the ultra-sharp tip end. Very importantly, the slope of the diameter increment is reduced to 0.087 when the Z_{ext} is larger than 0.5 µm, that is, only 87 nm differences in dot diameter at 1 µm variation of Z_{ext}. In comparison, PPL experiments using homogenous elastomer pen array typically exhibit a dot size increment of 200-300 nm per 1 µm Z_{ext} (from our experiments and references[10, 204]). The difference of force-dependence behavior becomes more significant when the tip array is under very large extension, e.g., 10 to 90 µm. The homogenous tip array has linearly large increase of tip-substrate contact size at the whole extension range, whereas the tips in the dual-elastomer tip array remain small deformation and the soft base layer is compressed.

Because of the advantage in small size variation using the dual-elastomer tip array, the uniformity of the features made by different tips across a large distance in PPL experiments can be significantly improved without the need for additional force-feedback system. We fabricated 10×10 dot arrays using the dual-elastomer tip array with a dwell time of 0.1 s, Z_{ext} of 7.5 µm, and humidity of 50%, and measured the average feature size in each array made by each tip over a distance of 4 mm (50 arrays in total). The result is shown in Figure 7.3D. In average, the dot has a diameter of 1.97 μm with a relative standard deviation (RSD) of 10%. In comparison, similar experiments made with conventional homogenous hard polydimethylsiloxane (*h*-PDMS) tip arrays showed an average dot diameter of ~4 μm and a size variation of ~15% across 4 mm distance.[204]

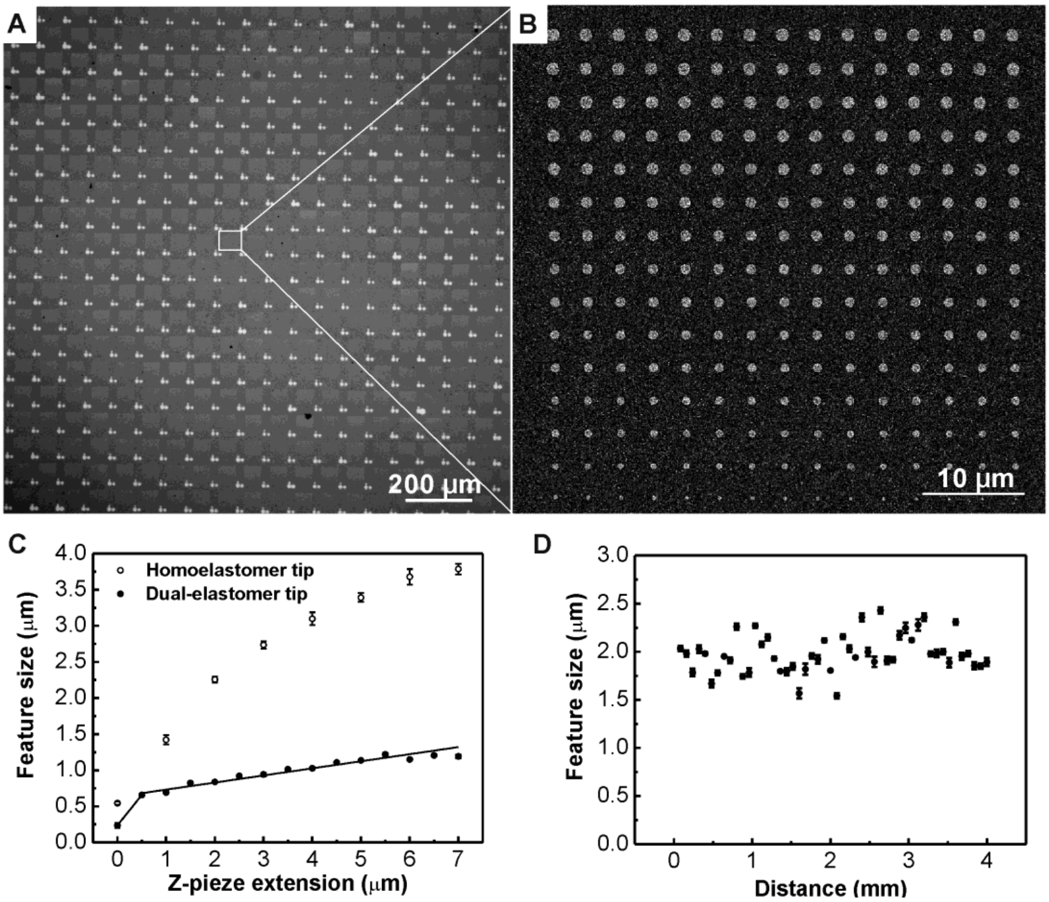

Figure 7.3. (A) Optical microscopes image of large-area Au patterns fabricated with a dual-elastomer tip array. (B) Zoom-in SEM image of one 15×15 array shown in (A), in which *z*-piezo extension was increased from 0 to 7 μm with a stepwise increment of 0.5 μm from bottom to top. (C) Plot of feature size versus *z*-piezo extension in (B), together with the results of control experiment using conventional homoelastomer pen arrays. (D) Plot of the feature sizes made by 50 tips across 4 mm distance.

7.3.3 Printing Polymer Ink by Dual-Elastomer Tip Arrays

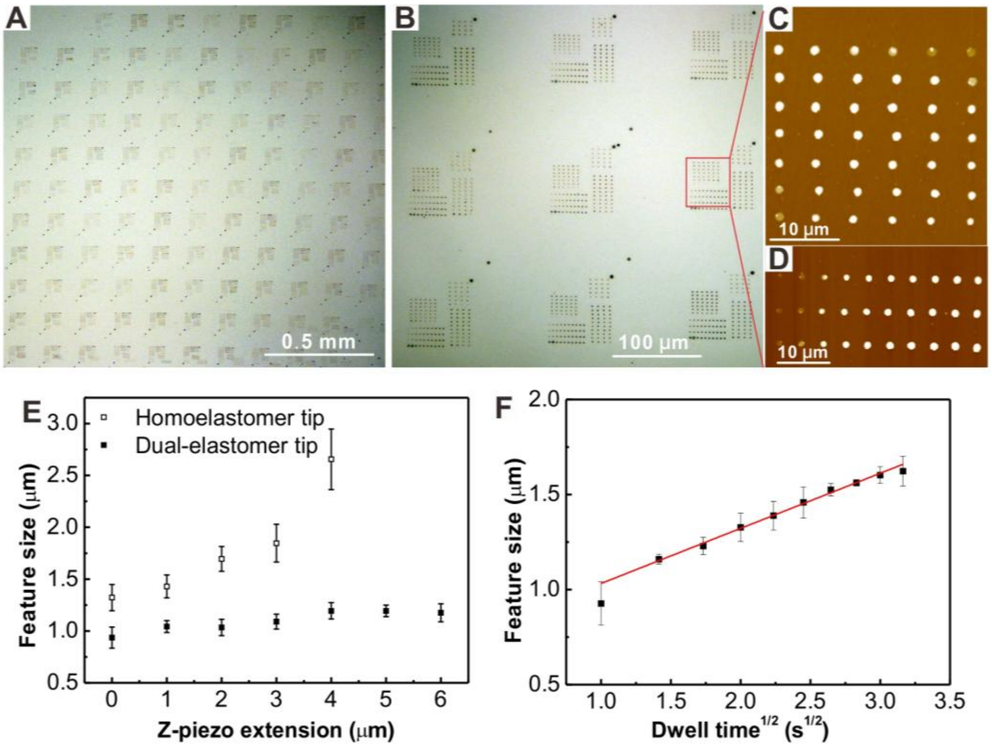

Figure 7.4. (A&B) Optical microscope images of PEG dot arrays printed by the dual-elastomer tip arrays, in which a 7×6 dot array (pitch=5 μm) was patterned by each tip with gradual increase in z-piezo extension from 0 to 6 μm (dwell time=1 s), and a 10×3 dot array (pitch=4 μm) was patterned with dwell time increasing from 1 s to 10 s (z-piezo extension=2 μm), under 90%RH. (C&D) Tapping mode AFM images of the generated arrays in A. (E) Force and (F) time dependence of the feature size. The force dependence of PEG features made by conventional homoelastomer tip is also shown in D as a comparison.

Apart from small molecules, highly uniform liquid ink can also be patterned using the dual-elastomer tip array. Polyethylene glycol (PEG, M_w=4,000) is taken as a demonstration because it can be used as cargo matrix to modulate ink transport and produce uniform patterns, which is particularly beneficial to patterning materials that are difficult to diffuse from a sharp tip, e.g., large biomolecules. PEG dot arrays were written under 90% humidity on Au surface over an area of ~1.5 × 1.5 mm^2 (Figure 7.4 A and B), in which a 7 × 6 dot array (pitch = 5 μm) was patterned by each tip with gradual increase in Z_{ext} from 0 to 6 μm (dwell time = 1 s), together with a 10 × 3 dot array (pitch = 4 μm) with dwell time between 1 and 10 s (Z_{ext} = 2 µm). From typical AFM images of the patterned dot arrays, as the Z_{ext} increased from 0 to 6 µm, the features maintained almost constant size from 0.94±0.10 µm to 1.17±0.09 µm (Figure 7.4C and E), with only ~24% size increase, which confirms the function of dual-elastomer tip. On the contrary, PEG features from homogeneous *h*-PDMS pen array showed significant size increase from 1.32±0.13 µm to 2.66±0.29 µm at a 4-µm increase in Z_{ext}. Meanwhile, by increasing the dwell time from 1 to 10 s, the dot diameter increased from 0.93±0.11 µm to 1.62±0.08 µm, with a linear relationship between the feature size and the square root of dwell time.

To pattern fluorescent arrays with Rhodamine B dye encapsulated in PEG matrix, each tip was programmed to make one 8 × 8 dot array (pitch = 7 µm) of PEG/Rhodamine B mixture on HMDS-SiO_2 using the conditions of 3 µm Z_{ext}, 1 s dwell time and 90% humidity. Figure 7.5A show the fluorescent patterns produced over very large areas. Some intensity scatter regions come from excessive amount of ink deposited in the first contact, especially due to low-quality tip and the non-uniform inking problem arising from spin coating. The halos of lower intensities are formed due to the diffusion of Rhodamine B molecules under highly humid environment, which was also observed in previous studies.[213] The average dot diameter within one array shown in Figure 7.5A is 1.64±0.10 µm (RSD = 6%). The dot diameter among different arrays across the whole imaging area is in the range of 1.4 to 2.0 µm. The average size measured from randomly selected 12 arrays is 1.66±0.14 µm (RSD = 8%), close to that within one array (Figure 7.5B).

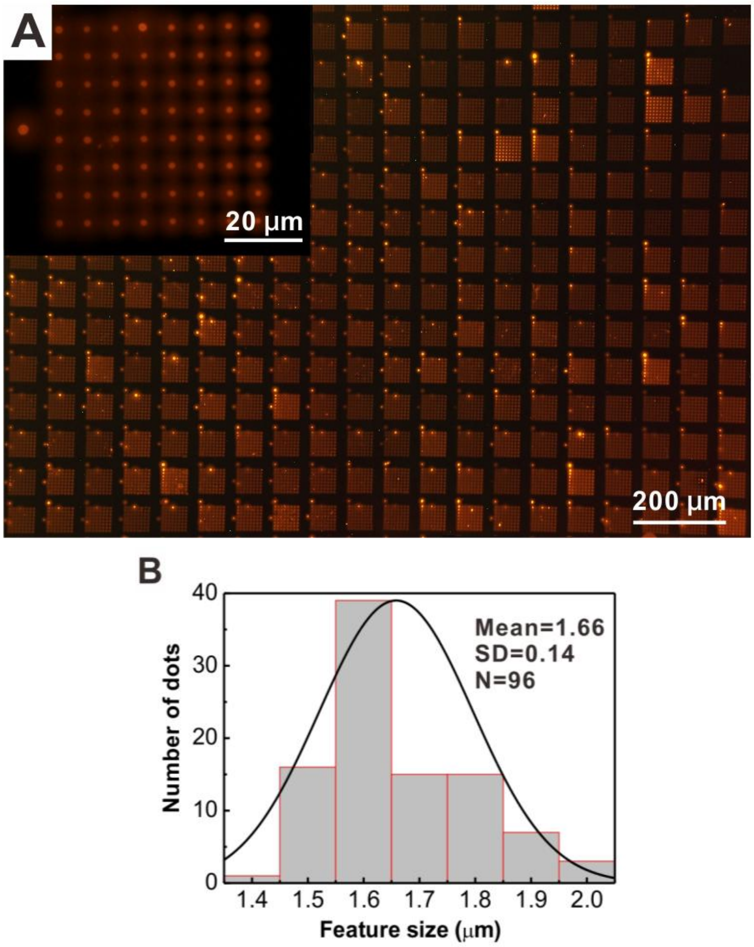

Figure 7.5. (A) Fluorescence microscope image of large-area fluorescent PEG/Rhodamine B dot arrays. The insert is a zoom-in image of a typical 8×8 array. (B) Feature size statistics of the fluorescent dots measured from 12 arrays in E.

7.3.4 Mechanical Simulations on Dual-Elastomer Tip Structure

The significant improvement in size control is attributed to the hard-apex, soft-base structure of the pyramidal tips of the dual-elastomer tip array. We performed finite-element (FE) simulations to study how a dual-elastomer tip deforms against a Si substrate during mechanical contact. Since Si possesses an elastic modulus two orders of magnitude higher than the elastomers, the substrate was taken as a rigid half-space whereas the tip as a linearly elastic solid in the simulation. To further minimize our computational effort, the tip was assumed to be of a conic shape with a finite tip radius. As a result, the original

3D contact problem can be simplified to a 2D axisymmetic one. Here, it is worth mentioning that the shape of the conic tip can be determined from the original four-sided pyramidal geometry by following the principle of geometric similarity in contact mechanics.[253] Figure 7.6A shows the geometry of the FE model and material properties used in the simulation (see Experimental for details). During the simulation, the tip is being “pressed” against the rigid half-space. Consequently, the apex is flattened with stress concentration being built up near the mechanical contact (Figure 7.6B), and the contact radius can be correlated with the half feature size in the PPL experiments. For comparison, we also carried out the FE simulations for a homogeneous tip design and different dual-elastomer tip designs. As shown in Figure 7.6C, we can clearly see that the contact radius grows rapidly at the small tip extensions regardless of the tip design. In this range of tip extension, the contact force is too small to cause appreciable deformation in the base material, and the size of the contact radius is sensitive to the geometry of the tip apex (radius of curvature). However, with the increasing tip extension, the “cushion” effect of the soft base becomes effective and the dual-elastomer tip thereby shows its advantage over the homogenous tip. As a result, the contact radius for the former tip grows at a much smaller rate than for the later. It is worth noting that the “cushion” effect of the soft base seems to become more prominent with the reducing portion of the hard apex. However, this is only valid for the size of the hard apex much larger than the radius of curvature. Otherwise, nonlinear effects, such as debonding and plasticity, may arise in the thin hard apex due to the local stress concentration, and the tip would behave as if it was only made up of the soft base. To find out an optimum tip design in the future work, we have to consider the tuning of the tip radius as well as the adjustment of the size of the hard apex relative to the soft base.

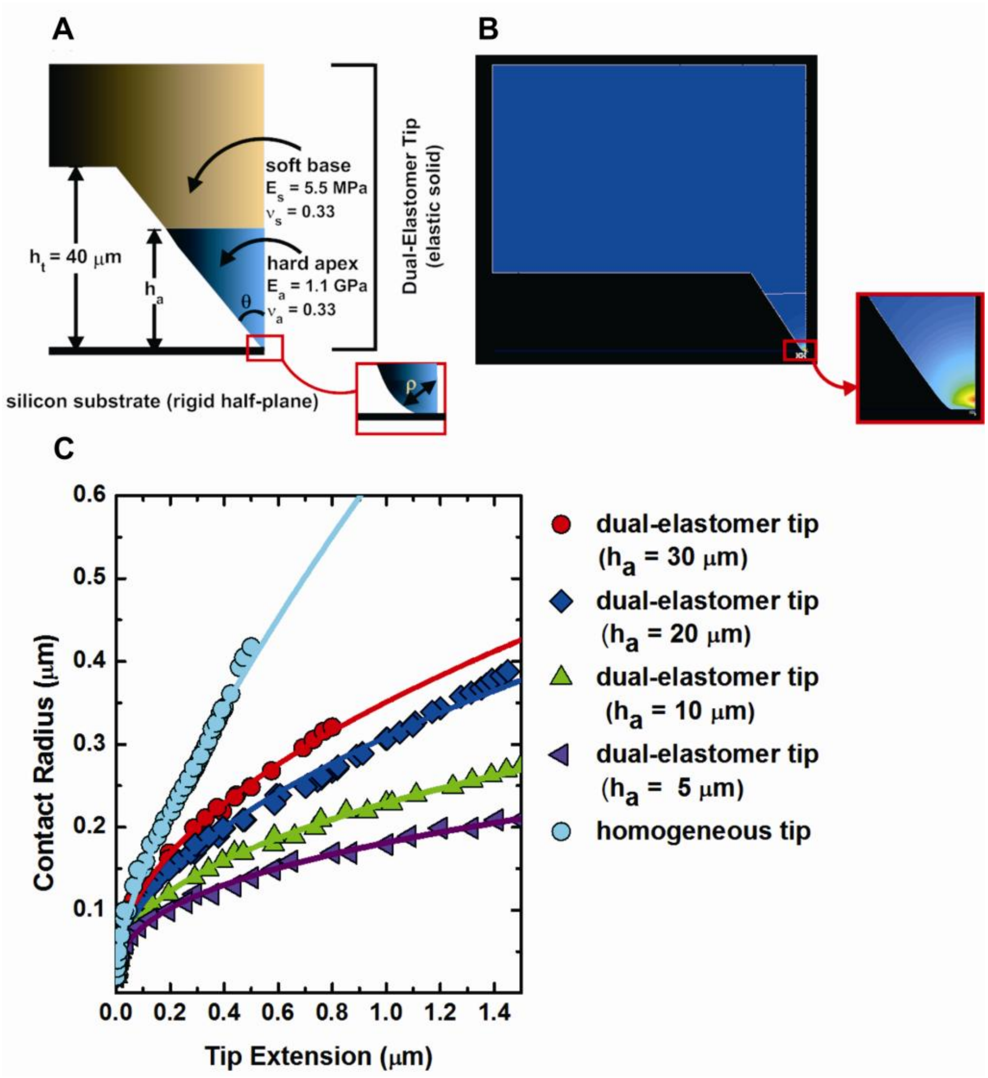

Figure 7.6. (A) Schematic illustration of the FE model used for simulating the tip-substrate contact during a PPL process (the conic angle θ = 33 deg; the tip radius ρ = 100 nm; the Young's modulus E_s = 5.5 MPa and Poisson's ratio ν_s = 0.33 for the soft base; the Young's modulus E_a = 1.1 GPa and Poisson's ratio ν_a = 0.33 for the hard apex; and the total height of the tip h_t = 40 μm). (B) von-Mises stress contour plot of the deformed dual-elastomer tip with a flattened apex, and (C) comparison of the contact radius as a function of the tip extension for different tip designs.

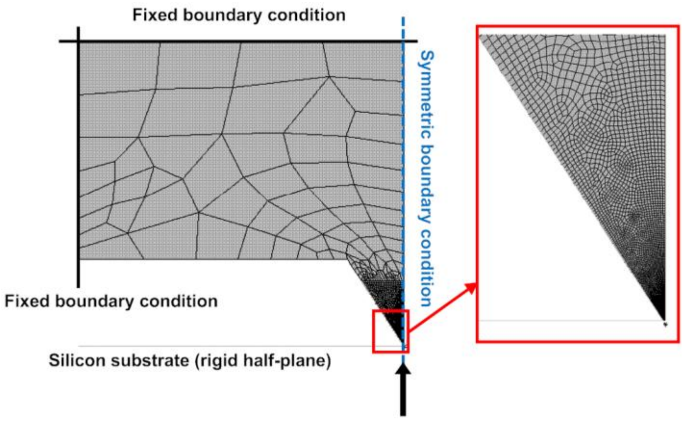

Figure 7.7. The FE model constructed by using the commercial package ANSYS™, which is meshed with the finest element size concentrated towards the tip apex while the coarsest in the area far away. During the simulation, the silicon substrate is pushed upwards while the tip maintains stationary, which equivalent to press down the AFM tip against a 'stationary' substrate.

7.3.5 Comparison with Other Tip Structures

From our experimental and simulation results, the dual-elastomer tip structure can give rise to enhanced resistance to tip deformation under large contact force compared with the homogeneous tip made with either hard or soft material. When compared with the Si-based cantilever and cantilever-free tip arrays,[193, 217] the dual-elastomer tip arrays show a great advantage in the fabrication process, being low-cost and high-speed mould replication. In contrast, Si-based tips are made by multistep lithography and etching process which requires expensive equipment and clean room environment. In addition, the dual-elastomer tip array maintains the force-dependence attribute, and can readily pattern nanometer and micrometer features. Although Si-based tips are more advanced in sub-50 nm patterning, it is force-independent and takes much long time for fabricating micropatterns. It should also be noted that in the literature, there are reports on using hard and soft elastomers to fabricate composite stamps for high-resolution microcontact and nanocontact printing.[51, 254-255] The soft part of the composite stamp can ensure easy handling and conformal contact of all hard elastomer features simultaneously with decreased pattern distortion over large areas. However, the structure of the composite stamp is dramatically different from our dual-elastomer tip array. In their composite stamp cases, the hard elastomer not only filled 100% of the recess wells in the mould, but also formed a thick backing layer that connects all the tips. On the contrary, the tip of dual-elastomer tip array developed here is designed into a hard-apex and soft-base structure further attached to a soft elastomeric backing layer, which exhibits more effectiveness in reducing the strain on the tip end.

7.4. Conclusions and Future Outlooks

In this chapter, we have reported PPL with dual-elastomer tip arrays for patterning nano and micro-scale structures. Very importantly, the study for the first time introduces a “hard-apex, soft-base” dual-elastomer tip structure, which significantly improves the patterning uniformity and resolution of PPL over large areas without the need for any additional force-feedback equipment or high-precision fabrication system. From our mechanical simulation, we envision that the performance of the dual-elastomer tip array can be substantially improved with the rational design of more optimized ratio between the hard apex and the soft base. Because the dual-elastomer tip arrays are fabricated by a simple, low-cost, and high-speed mould replication method, we believe that they can be readily applied by a wide variety of communities to fabricate uniform large-area arrays of functional patterns by either molecular printing or optical lithography.

CHAPTER 8

CONCLUSIONS AND SUGGESTIONS FOR FUTURE WORK

8.1. Conclusions

This thesis has described systematic studies and technology development on large-area, high-throughput, high-resolution patterning of function polymers via parallel scanning probe arrays. Nanoscale patterning, structural control and applications of the patterned polymer nanostructures have been achieved by combining parallel scanning probe printing with surface chemistry. Furthermore, by engineering the tip structure, two novel cantilever-free pen arrays have been developed with improved patterning capability.

In Chapter 4, direct writing of polymer materials by 1-D cantilever array and polymer pen array was studied. First, the ink transport of polyelectrolytes in DPN was shown to be determined by the surface chemistry of substrates and ink additives. The hydrophilic surface facilitated the transfer of ink molecules from the tip, while the hydrophobic surface was found to confine ink diffusion to generate patterns as small as ~50 nm. In the presence of only small percentage of hygroscopic additives, the ink transport was tuned from molecular diffusion to liquid deposition, leading to increased ink transfer while maintaining a size of sub-300 nm. By using the absorbent polymer pen and hydrophobic surface, polyelectrolyte inks were also printed in liquid form without additives over large areas, in which submicrometer-sized features were generated. Second, the liquid polymer delivering matrix was employed for site-selective immobilization of ionic species onto the substrate, in combination with the surface-grafted polyelectrolyte layer as receiving matrix. Catalytic salts were printed onto PMETAC-grafted PET film with high-density and stable loading, which were further used to generate robust Cu micropatterns through electroless deposition.

Conclusions and Suggestions for Future Work

In Chapter 5, PPL was demonstrated as a powerful tool for high-throughput generation of complex 2D and 3D polymer brush patterns over centimeter-square area. In PPL, the density and nanoscale position of printed molecular initiators were precisely programmed, thus the structures of polymer brushes grown by SI-ATRP were well-controlled in the three dimensions. Complex 3D patterns were generated by feature-density method, with a throughput being 3 orders of magnitudes higher than the state-of-the-arts. The large-area patterned functional polymer brushes were used as etching resist for fabricating Au patterns and soft stamps, as well as robust and versatile platforms for immobilization of biomolecules and chip-based assays.

In Chapter 6, the transparent, self-light-focusing PDMS pyramid was explored as an apertureless probe to direct light onto a surface as well as a soft pen for simultaneous molecular printing. By applying an opaque coating on the flat backing regions between the pyramid arrays, scanning optical lithography was successfully performed using the apertureless pens. The illumination region can be tuned by contact force through reversible deformation of the elastomeric pens, leading to photoresist and metal patterns with feature size gradient from several micrometers to ~200 nm. Furthermore, the apertureless pen array was demonstrated to simultaneously print molecules and initiate photochemical reaction for site-selective chemical modification on the substrates. This novel apertureless pen array is believed to be a promising low-cost, easy-accessible tool for maskless, high-resolution photochemical printing.

In Chapter 7, a novel dual-elastomer tip array was developed to address the challenge of severe tip deformation in conventional polymer pen arrays. The "hard-apex, soft-base" dual-elastomer tip structure was for the first time introduced and fabricated by a simple, low-cost, and high-speed mould replication method. The patterning capability was evaluated by both PPL experiments on molecular and polymer inks and mechanical simulations, which shows significant improvements in the patterning uniformity and resolution over large areas owing to reduced tip deformation. From our mechanical simulation, the performance of the dual-elastomer tip array can be substantially improved with the rational design of more optimized ratio between the hard apex and the soft base.

8.2. Suggestions for Future Work

Because this research project mainly focus on development of new methodology and nanofabrication tools, it has paved the avenue to patterning various functional polymers by parallel scanning probe arrays and practical applications from the large-area patterned nanostructures. In future work, there still remain many challenges to address with respect to the patterning techniques and the applications.

1. Polymer pen array has been demonstrated as an ideal tool for direct printing of polymer materials. Therefore, it can be used to print a wide range of water-soluble functional polymers for electronic device and biochip fabrication. For example, PPL is particularly suitable to pattern multilayered memory devices due to the high registration. Because the pen array also allows delivery of mechanical and optical energy, approaches combining contact force, light and surface chemistry can be explored to control the delivery of polymer materials and improve resolution to sub-100 nm.

2. Based on surface-initiated polymerizations, patterning 3D polymer brushes can be achieved by other scanning probe arrays, e.g., 2-D cantilever array, hard-tip, soft-spring pen array, dual-elastomer tip array or beam pen array. These pen arrays will enable enhanced resolution and uniformity compared with currently used polymer pen array. The topographic and chemical patterns of polymer brushes over large areas are interesting interfaces for regulating the adhesion, growth, migration and differentiation of cells in both passive and active ways. Multiplexed 3D brush arrays can be also made with gradient in size, composition, functionality for high-throughput screening of biological process.

3. Following the apertureless pen concept, multiplexed surface patterns can

be envisioned by combining the pen array with multiplexed printing or actuation techniques. And the apertureless tip structure would allow more functionality by coating the tip with functional materials, e.g. nanoparticles with photocatalytic or plasmonic properties. Moreover, the exact shape of deformed tip is still unknown, which can be studied by combining experiments and mechanical-optical simulations.

4. Optimization on dual-elastomer tip array is desirable to achieve sub-100 nm nanopatterning over cm^2 areas. Other hard and soft elastomers can be investigated to tune the tip deformation. The tip structure can be also applied to energy-based fabrication and other fields where uniform nanoscale contact area is needed.

REFERENCES

1. Nie, Z. H., and Kumacheva, E. (2008) Patterning surfaces with functional polymers. *Nat. Mater.,* 7: 277.
2. del Campo, A., and Arzt, E. (2008) Fabrication approaches for generating complex micro- and nanopatterns on polymeric surfaces. *Chem. Rev.,* 108: 911.
3. Menard, E., et al. (2007) Micro- and nanopatterning techniques for organic electronic and optoelectronic systems. *Chem. Rev.,* 107: 1117.
4. Stuart, M. A. C., et al. (2010) Emerging applications of stimuli-responsive polymer materials. *Nat. Mater.,* 9: 101.
5. Coyle, S., Wu, Y. Z., Lau, K. T., De Rossi, D., Wallace, G., and Diamond, D. (2007) Smart nanotextiles: A review of materials and applications. *MRS Bull.,* 32: 434.
6. Chou, S. Y., Krauss, P. R., and Renstrom, P. J. (1996) Imprint lithography with 25-nanometer resolution. *Science,* 272: 85.
7. Xia, Y. N., and Whitesides, G. M. (1998) Soft lithography. *Angew. Chem. Int. Ed.,* 37: 551.
8. Bang, J., Jeong, U., Ryu, D. Y., Russell, T. P., and Hawker, C. J. (2009) Block Copolymer Nanolithography: Translation of Molecular Level Control to Nanoscale Patterns. *Adv. Mater.,* 21: 4769.
9. Wouters, D., and Schubert, U. S. (2004) Nanolithography and Nanochemistry: Probe-Related Patterning Techniques and Chemical Modification for Nanometer-Sized Devices. *Angew. Chem. Int. Ed.,* 43: 2480.
10. Huo, F. W., Zheng, Z. J., Zheng, G. F., Giam, L. R., Zhang, H., and Mirkin, C. A. (2008) Polymer pen lithography. *Science*, 321: 1658.
11. Huo, F. W., et al. (2010) Beam pen lithography. *Nat. Nanotech.,* 5: 637.
12. Kumar, A., and Whitesides, G. M. (1993) Features of Gold Having Micrometer to Centimeter Dimensions Can Be Formed through a Combination of Stamping with an Elastomeric Stamp and an Alkanethiol Ink Followed by Chemical Etching. *Appl. Phys. Lett.,* 63: 2002.
13. Piner, R. D., Zhu, J., Xu, F., Hong, S. H., and Mirkin, C. A. (1999) "Dip-pen" nanolithography. *Science*, 283: 661.
14. Wiley, B. J., Qin, D., and Xia, Y. N. (2010) Nanofabrication at High Throughput and Low Cost. *ACS Nano*, 4: 3554.
15. Xia, Y. N., Rogers, J. A., Paul, K. E., and Whitesides, G. M. (1999) Unconventional methods for fabricating and patterning nanostructures. *Chem. Rev.,* 99: 1823.
16. Gates, B. D., Xu, Q. B., Stewart, M., Ryan, D., Willson, C. G., and Whitesides, G. M. (2005) New approaches to nanofabrication: Molding, printing, and other techniques. *Chem. Rev.,* 105: 1171.
17. Lee, T. W., Jeon, S., Maria, J., Zaumseil, J., Hsu, J. W. P., and Rogers, J. A. (2005) Soft-contact optical lithography using transparent elastomeric stamps: application to nanopatterned organic light-emitting devices. *Adv. Funct. Mater.,*

15: 1435.

18. Schuh, C., Santer, S., Prucker, O., and Ruhe, J. (2009) Polymer Brushes with Nanometer-Scale Gradients. *Adv. Mater.,* 21: 4706.

19. Manfrinato, V. R., Zhang, L., Su, D., Duan, H., Hobbs, R. G., Stach, E. A., and Berggren, K. K. (2013) Resolution Limits of Electron-Beam Lithography toward the Atomic Scale. *Nano Lett.,* 13: 1555.

20. Paik, M. Y., Xu, Y. Y., Rastogi, A., Tanaka, M., Yi, Y., and Ober, C. K. (2010) Patterning of Polymer Brushes. A Direct Approach to Complex, Sub-Surface Structures. *Nano Lett.,* 10: 3873.

21. Rastogi, A., Paik, M. Y., Tanaka, M., and Ober, C. K. (2010) Direct Patterning of Intrinsically Electron Beam Sensitive Polymer Brushes. *ACS Nano,* 4: 771.

22. Han, E., Kim, M., and Gopalan, P. (2012) Chemical Patterns from Surface Grafted Resists for Directed Assembly of Block Copolymers. *ACS Nano,* 6: 1823.

23. Christman, K. L., Schopf, E., Broyer, R. M., Li, R. C., Chen, Y., and Maynard, H. D. (2009) Positioning Multiple Proteins at the Nanoscale with Electron Beam Cross-Linked Functional Polymers. *J. Am. Chem. Soc.,* 131: 521.

24. Carrad, D. J., et al. (2014) Electron-Beam Patterning of Polymer Electrolyte Films To Make Multiple Nanoscale Gates for Nanowire Transistors. *Nano Lett.,* 14: 94.

25. Kim, S., et al. (2014) All-water-based electron-beam lithography using silk as a resist. *Nat. Nanotech.,* 9: 306.

26. Guo, L. J. (2007) Nanoimprint lithography: Methods and material requirements. *Adv. Mater.,* 19: 495.

27. Costner, E. A., Lin, M. W., Jen, W. L., and Willson, C. G. (2009) Nanoimprint lithography materials development for semiconductor device fabrication. *Annu. Rev. Mater. Res.,* 39: 155.

28. Tan, H., Gilbertson, A., and Chou, S. Y. (1998) Roller nanoimprint lithography. *J. Vac. Sci. Technol. B,* 16: 3926.

29. Resnick, D. J., Sreenivasan, S. V., and Willson, C. G. (2005) Step & flash imprint lithography. *Mater. Today,* 8: 34.

30. Khang, D. Y., Yoon, H., and Lee, H. H. (2001) Room Temperature Imprint Lithography. *Adv. Mater.,* 13: 749.

31. Di Benedetto, F., et al. (2008) Patterning of light-emitting conjugated polymer nanofibres. *Nat. Nanotech.,* 3: 614.

32. Mele, E., Di Benedetto, F., Persano, L., Cingolani, R., and Pisignano, D. (2005) Multilevel, room-temperature nanoimprint lithography for conjugated polymer-based photonics. *Nano Lett.,* 5: 1915.

33. Battaglia, C., Escarre, J., Soderstrom, K., Charriere, M., Despeisse, M., Haug, F. J., and Ballif, C. (2011) Nanomoulding of transparent zinc oxide electrodes for efficient light trapping in solar cells. *Nat Photonics,* 5: 535.

34. Li, G. J., Li, H., Ho, J. Y. L., Wong, M., and Kwok, H. S. (2014) Nanopyramid Structure for Ultrathin c-Si Tandem Solar Cells. *Nano Lett.,* 14:

2563.

35. Dong, Q., et al. (2012) A Polyferroplatinyne Precursor for the Rapid Fabrication of L10-FePt-type Bit Patterned Media by Nanoimprint Lithography. *Adv. Mater.,* 24: 1034.

36. Nougaret, L., et al. (2014) Nanoscale Design of Multifunctional Organic Layers for Low-Power High-Density Memory Devices. *ACS Nano,* 8: 3498.

37. Ahn, S. H., and Guo, L. J. (2008) High-Speed Roll-to-Roll Nanoimprint Lithography on Flexible Plastic Substrates. *Adv. Mater.,* 20: 2044.

38. Ahn, S. H., and Guo, L. J. (2009) Large-Area Roll-to-Roll and Roll-to-Plate Nanoimprint Lithography: A Step toward High-Throughput Application of Continuous Nanoimprinting. *ACS Nano,* 3: 2304.

39. Hu, Z. J., Baralia, G., Bayot, V., Gohy, J. F., and Jonas, A. M. (2005) Nanoscale control of polymer crystallization by nanoimprint lithography. *Nano Lett.,* 5: 1738.

40. Zheng, Z. J., Yim, K. H., Saifullah, M. S. M., Welland, M. E., Friend, R. H., Kim, J. S., and Huck, W. T. S. (2007) Uniaxial alignment of liquid-crystalline conjugated polymers by nanoconfinement. *Nano Lett.,* 7: 987.

41. Aryal, M., Trivedi, K., and Hu, W. (2009) Nano-Confinement Induced Chain Alignment in Ordered P3HT Nanostructures Defined by Nanoimprint Lithography. *ACS Nano,* 3: 3085.

42. Hlaing, H., Lu, X. H., Hofmann, T., Yager, K. G., Black, C. T., and Ocko, B. M. (2011) Nanoimprint-Induced Molecular Orientation in Semiconducting Polymer Nanostructures. *ACS Nano,* 5: 7532.

43. Hu, Z. J., Tian, M. W., Nysten, B., and Jonas, A. M. (2009) Regular arrays of highly ordered ferroelectric polymer nanostructures for non-volatile low-voltage memories. *Nat. Mater.,* 8: 62.

44. Yang, Y., Mielczarek, K., Aryal, M., Zakhidov, A., and Hu, W. (2012) Nanoimprinted Polymer Solar Cell. *ACS Nano,* 6: 2877.

45. Qin, D., Xia, Y. N., and Whitesides, G. M. (2010) Soft lithography for micro- and nanoscale patterning. *Nat. Protoc.,* 5: 491.

46. Weibel, D. B., DiLuzio, W. R., and Whitesides, G. M. (2007) Microfabrication meets microbiology. *Nat. Rev. Microbiol.,* 5: 209.

47. Kaufmann, T., and Ravoo, B. J. (2010) Stamps, inks and substrates: polymers in microcontact printing. *Polym. Chem.,* 1: 371.

48. Perl, A., Reinhoudt, D. N., and Huskens, J. (2009) Microcontact Printing: Limitations and Achievements. *Adv. Mater.,* 21: 2257.

49. Park, J., Kim, Y. S., and Hammond, P. T. (2005) Chemically nanopatterned surfaces using polyelectrolytes and ultraviolet-cured hard molds. *Nano Lett.,* 5: 1347.

50. Ricoult, S. G., Pla-Roca, M., Safavieh, R., Lopez-Ayon, G. M., Grütter, P., Kennedy, T. E., and Juncker, D. (2013) Large Dynamic Range Digital Nanodot Gradients of Biomolecules Made by Low-Cost Nanocontact Printing for Cell Haptotaxis. *Small,* 9: 3308.

51. Li, H.-W., Muir, B. V. O., Fichet, G., and Huck, W. T. S. (2003) Nanocontact

Printing: A Route to Sub-50-nm-Scale Chemical and Biological Patterning. *Langmuir,* 19: 1963.

52. Jang, S. G., Choi, D. G., Kim, S., Jeong, J. H., Lee, E. S., and Yang, S. M. (2006) Nanoscopic Pd line arrays using nanocontact printed dendrimers. *Langmuir,* 22: 3326.

53. Duan, X. X., Zhao, Y. P., Perl, A., Berenschot, E., Reinhoudt, D. N., and Huskens, J. (2009) High-Resolution Contact Printing with Chemically Patterned Flat Stamps Fabricated by Nanoimprint Lithography. *Adv. Mater.,* 21: 2798.

54. Sharpe, R. B. A., Burdinski, D., Huskens, J., Zandvliet, H. J. W., Reinhoudt, D. N., and Poelsema, B. (2005) Chemically patterned flat stamps for microcontact printing. *J. Am. Chem. Soc.,* 127: 10344.

55. Lee, M. H., Lin, J. Y., and Odom, T. W. (2010) Large-Area Nanocontact Printing with Metallic Nanostencil Masks. *Angew. Chem. Int. Ed.,* 49: 3057.

56. Wang, F., Xue, M., and Cao, T. (2009) Thermochemical Patterning of Polymer Thin Films With Tunable Size-Reduction Effects Using Metal-Coated Poly(dimethylsiloxane) Stamps. *Adv. Mater.,* 21: 2211.

57. Xue, M., Ma, X., Xie, Z., Duan, L., Jiang, Y., Zhang, M., and Cao, T. (2010) Fabrication of Gold-Directed Conducting Polymer Nanoarrays for High-Performance Gas Sensor. *Chem. Asian J.,* 5: 2266.

58. Kim, E., Xia, Y. N., and Whitesides, G. M. (1995) Polymer microstructures formed by moulding in capillaries. *Nature,* 376: 581.

59. Cavallini, M., and Biscarini, F. (2003) Nanostructuring conjugated materials by lithographically controlled wetting. *Nano Lett.,* 3: 1269.

60. Cavallini, M., Gentili, D., Greco, P., Valle, F., and Biscarini, F. (2012) Micro- and nanopatterning by lithographically controlled wetting. *Nat. Protoc.,* 7: 1668.

61. Hwang, J. K., Cho, S., Dang, J. M., Kwak, E. B., Song, K., Moon, J., and Sung, M. M. (2010) Direct nanoprinting by liquid-bridge-mediated nanotransfer moulding. *Nat. Nanotech.,* 5: 742.

62. Hamedi, M., Tvinstedt, K., Karlsson, R. H., Asberg, P., and Inganas, O. (2009) Bridging Dimensions in Organic Electronics: Assembly of Electroactive Polymer Nanodevices from Fluids. *Nano Lett.,* 9: 631.

63. Duan, X. X., Zhao, Y. P., Berenschot, E., Tas, N. R., Reinhoudt, D. N., and Huskens, J. (2010) Large-Area Nanoscale Patterning of Functional Materials by Nanomolding in Capillaries. *Adv. Funct. Mater.,* 20: 2519.

64. Cavallini, M., et al. (2005) Field-effect transistors based on self-organized molecular nanostripes. *Nano Lett.,* 5: 2422.

65. Gentili, D., et al. (2013) Logic-Gate Devices Based on Printed Polymer Semiconducting Nanostripes. *Nano Lett.,* 13: 3643.

66. Park, K. S., Cho, B., Baek, J., Hwang, J. K., Lee, H., and Sung, M. M. (2013) Single-Crystal Organic Nanowire Electronics by Direct Printing from Molecular Solutions. *Adv. Funct. Mater.,* 23: 4776.

67. Lee, J. I., Cho, S. H., Park, S. M., Kim, J. K., Yu, J. W., Kim, Y. C., and Russell, T. P. (2008) Highly aligned ultrahigh density arrays of conducting

polymer nanorods using block copolymer templates. *Nano Lett.,* 8: 2315.

68. Jung, Y. S., Jung, W., Tuller, H. L., and Ross, C. A. (2008) Nanowire Conductive Polymer Gas Sensor Patterned Using Self-Assembled Block Copolymer Lithography. *Nano Lett.,* 8: 3776.

69. Ruiz, R., et al. (2008) Density multiplication and improved lithography by directed block copolymer assembly. *Science,* 321: 936.

70. Braunschweig, A. B., Huo, F. W., and Mirkin, C. A. (2009) Molecular printing. *Nat. Chem.,* 1: 353.

71. Tseng, A. A., Notargiacomo, A., and Chen, T. P. (2005) Nanofabrication by scanning probe microscope lithography: A review. *J. Vac. Sci. Technol. B,* 23: 877.

72. Tseng, A. A., Jou, S., Notargiacomo, A., and Chen, T. P. (2008) Recent developments in tip-based nanofabrication and its roadmap. *J. Nanosci. Nanotech.,* 8: 2167.

73. Kramer, S., Fuierer, R. R., and Gorman, C. B. (2003) Scanning probe lithography using self-assembled monolayers. *Chem. Rev.,* 103: 4367.

74. Ginger, D. S., Zhang, H., and Mirkin, C. A. (2004) The evolution of dip-pen nanolithography. *Angew. Chem. Int. Ed.,* 43: 30.

75. Salaita, K., Wang, Y. H., and Mirkin, C. A. (2007) Applications of dip-pen nanolithography. *Nat. Nanotech.,* 2: 145.

76. Tseng, A. A. (2011) Removing Material Using Atomic Force Microscopy with Single- and Multiple-Tip Sources. *Small,* 7: 3409.

77. Garcia, R., Knoll, A. W., and Riedo, E. (2014) Advanced scanning probe lithography. *Nat. Nanotech.,* 9: 577.

78. Lee, W. K., and Sheehan, P. E. (2008) Scanning probe lithography of polymers: Tailoring morphology and functionality at the nanometer scale. *Scanning,* 30: 172.

79. O'Connell, C. D., Higgins, M. J., Marusic, D., Moulton, S. E., and Wallace, G. G. (2014) Liquid Ink Deposition from an Atomic Force Microscope Tip: Deposition Monitoring and Control of Feature Size. *Langmuir,* 30: 2712.

80. O'Connell, C. D., Higgins, M. J., Sullivan, R. P., Moulton, S. E., and Wallace, G. G. (2014) Ink-on-Probe Hydrodynamics in Atomic Force Microscope Deposition of Liquid Inks. *Small,* 10: 3717.

81. Eichelsdoerfer, D. J., Brown, K. A., and Mirkin, C. A. (2014) Capillary bridge rupture in dip-pen nanolithography. *Soft Matter,* 10: 5603.

82. Liu, G. L., et al. (2013) The role of viscosity on polymer ink transport in dip-pen nanolithography. *Chem. Sci.,* 4: 2093.

83. Lim, J. H., and Mirkin, C. A. (2002) Electrostatically driven dip-pen nanolithography of conducting polymers. *Adv. Mater.,* 14: 1474.

84. Yu, M., Nyamjav, D., and Ivanisevic, A. (2005) Fabrication of positively and negatively charged polyelectrolyte structures by dip-pen nanolithography. *J. Mater. Chem.,* 15: 649.

85. Narui, Y., and Salaita, K. S. (2012) Dip-pen nanolithography of optically transparent cationic polymers to manipulate spatial organization of proteolipid

membranes. *Chem. Sci.,* 3: 794.

86. McKendry, R., Huck, W. T. S., Weeks, B., Florini, M., Abell, C., and Rayment, T. (2002) Creating nanoscale patterns of dendrimers on silicon surfaces with dip-pen nanolithography. *Nano Lett.,* 2: 713.

87. Salazar, R. B., Shovsky, A., Schonherr, H., and Vancso, G. J. (2006) Dip-pen nanolithography on (bio)reactive monolayer and block-copolymer platforms: Deposition of lines of single macromolecules. *Small,* 2: 1274.

88. Tang, Q., and Shi, S. Q. (2008) Preparation of gas sensors via dip-pen nanolithography. *Sensor. Actuat. B-Chem.,* 131: 379.

89. Shin, Y. S., Son, J. Y., Jo, M. H., Shin, Y. H., and Jang, H. M. (2011) High-Mobility Graphene Nanoribbons Prepared Using Polystyrene Dip-Pen Nanolithography. *J. Am. Chem. Soc.,* 133: 5623.

90. Noy, A., Miller, A. E., Klare, J. E., Weeks, B. L., Woods, B. W., and DeYoreo, J. J. (2002) Fabrication of luminescent nanostructures and polymer nanowires using dip-pen nanolithography. *Nano Lett.,* 2: 109.

91. Tang, Q., Shi, S. Q., Huang, H. T., and Zhou, L. M. (2004) Fabrication of highly oriented microstructures and nanostructures of ferroelectric P(VDF-TrFE) copolymer via dip-pen nanolithography. *Superlattices Microstruct.,* 36: 21.

92. Son, J. Y., Ryu, S., Park, Y. C., Lim, Y. T., Shin, Y. S., Shin, Y. H., and Jang, H. M. (2010) A Nonvolatile Memory Device Made of a Ferroelectric Polymer Gate Nanodot and a Single-Walled Carbon Nanotube. *ACS Nano,* 4: 7315.

93. Sanedrin, R. G., Huang, L., Jang, J. W., Kakkassety, J., and Mirkin, C. A. (2008) Polyethylene glycol as a novel resist and sacrificial material for generating positive and negative nanostructures. *Small,* 4: 920.

94. Jang, J. W., et al. (2009) Generation of Metal Photomasks by Dip-Pen Nanolithography. *Small,* 5: 1850.

95. Zheng, Z., Jang, J. W., Zheng, G., and Mirkin, C. A. (2008) Topographically Flat, Chemically Patterned PDMS Stamps Made by Dip-Pen Nanolithography. *Angew. Chem. Int. Ed.,* 47: 9951.

96. Jang, J. W., Zheng, Z. J., Lee, O. S., Shim, W., Zheng, G. F., Schatz, G. C., and Mirkin, C. A. (2010) Arrays of Nanoscale Lenses for Subwavelength Optical Lithography. *Nano Lett.,* 10: 4399.

97. Hernandez-Santana, A., Irvine, E., Faulds, K., and Graham, D. (2011) Rapid prototyping of poly(dimethoxysiloxane) dot arrays by dip-pen nanolithography. *Chem. Sci.,* 2: 211.

98. Huang, L., et al. (2010) Matrix-Assisted Dip-Pen Nanolithography and Polymer Pen Lithography. *Small,* 6: 1077.

99. Li, H., et al. (2011) Nanoscale-Controlled Enzymatic Degradation of Poly(L-lactic acid) Films Using Dip-Pen Nanolithography. *Small,* 7: 226.

100. Arrabito, G., Reisewitz, S., Dehmelt, L., Bastiaens, P. I., Pignataro, B., Schroeder, H., and Niemeyer, C. M. (2013) Biochips for Cell Biology by Combined Dip-Pen Nanolithography and DNA-Directed Protein Immobilization. *Small,* 9: 4243.

References

101. Su, M., Aslam, M., Fu, L., Wu, N. Q., and Dravid, V. P. (2004) Dip-pen nanopatterning of photosensitive conducting polymer using a monomer ink. *Appl. Phys. Lett.,* 84: 4200.

102. Qin, L. D., Park, S., Huang, L., and Mirkin, C. A. (2005) On-wire lithography. *Science,* 309: 113.

103. Lu, H. H., et al. (2009) Electrical properties of single and multiple poly(3,4- ethylenedioxythiophene) nanowires for sensing nitric oxide gas. *Anal. Chim. Acta,* 640: 68.

104. Nakashima, H., Higgins, M. J., O'Connell, C., Torimitsu, K., and Wallace, G. G. (2012) Liquid Deposition Patterning of Conducting Polymer Ink onto Hard and Soft Flexible Substrates via Dip-Pen Nano lithography. *Langmuir,* 28: 804.

105. Senesi, A. J., Rozkiewicz, D. I., Reinhoudt, D. N., and Mirkin, C. A. (2009) Agarose-Assisted Dip-Pen Nanolithography of Oligonucleotides and Proteins. *ACS Nano,* 3: 2394.

106. Lim, J. H., Ginger, D. S., Lee, K. B., Heo, J., Nam, J. M., and Mirkin, C. A. (2003) Direct-write dip-pen nanolithography of proteins on modified silicon oxide surfaces. *Angew. Chem. Int. Ed.,* 42: 2309.

107. Shin, Y. H., et al. (2010) Polymer-Coated Tips for Patterning of Viruses by Dip-Pen Nanolithography. *Angew. Chem. Int. Ed.,* 49: 9689.

108. Su, M., Liu, X. G., Li, S. Y., Dravid, V. P., and Mirkin, C. A. (2002) Moving beyond molecules: Patterning solid-state features via dip-pen nanolithography with sol-based inks. *J. Am. Chem. Soc.,* 124: 1560.

109. O'Connell, C. D., Higgins, M. J., Nakashima, H., Moulton, S. E., and Wallace, G. G. (2012) Vapor Phase Polymerization of EDOT from Submicrometer Scale Oxidant Patterned by Dip-Pen Nanolithography. *Langmuir,* 28: 9953.

110. Wang, W. C. M., Stoltenberg, R. M., Liu, S. H., and Bao, Z. N. (2008) Direct Patterning of Gold Nanoparticles Using Dip-Pen Nanolithography. *ACS Nano,* 2: 2135.

111. Wang, H. T., et al. (2008) Toward conductive traces: Dip Pen Nanolithography (R) of silver nanoparticle-based inks. *Appl. Phys. Lett.,* 93.

112. Chai, J., Huo, F. W., Zheng, Z. J., Giam, L. R., Shim, W., and Mirkin, C. A. (2010) Scanning probe block copolymer lithography. *PNAS,* 107: 20202.

113. Giam, L. R., et al. (2012) Positionally Defined, Binary Semiconductor Nanoparticles Synthesized by Scanning Probe Block Copolymer Lithography. *Nano Lett.,* 12: 1022.

114. Liu, G. L., Eichelsdoerfer, D. J., Rasin, B., Zhou, Y., Brown, K. A., Liao, X., and Mirkin, C. A. (2013) Delineating the pathways for the site-directed synthesis of individual nanoparticles on surfaces. *PNAS,* 110: 887.

115. Chai, J., Wong, L. S., Giam, L., and Mirkin, C. A. (2011) Single-molecule protein arrays enabled by scanning probe block copolymer lithography. *PNAS,* 108: 19521.

116. Hernandez-Santana, A., Mackintosh, A. R., Guilhabert, B.,

References

Kanibolotsky, A. L., Dawson, M. D., Skabara, P. J., and Graham, D. (2011) Dip-pen nanolithography of nanostructured oligofluorene truxenes in a photo-curable host matrix. *J. Mater. Chem.,* 21: 14209.

117. Lee, W. K., Robinson, J. T., Gunlycke, D., Stine, R. R., Tamanaha, C. R., King, W. P., and Sheehan, P. E. (2011) Chemically Isolated Graphene Nanoribbons Reversibly Formed in Fluorographene Using Polymer Nanowire Masks. *Nano Lett.,* 11: 5461.

118. Lee, W. K., Dai, Z. T., King, W. P., and Sheehan, P. E. (2010) Maskless Nanoscale Writing of Nanoparticle-Polymer Composites and Nanoparticle Assemblies using Thermal Nanoprobes. *Nano Lett.,* 10: 129.

119. Yang, M., Sheehan, P. E., King, W. P., and Whitman, L. J. (2006) Direct writing of a conducting polymer with molecular-level control of physical dimensions and orientation. *J. Am. Chem. Soc.,* 128: 6774.

120. Felts, J. R., Onses, M. S., Rogers, J. A., and King, W. P. (2014) Nanometer Scale Alignment of Block-Copolymer Domains by Means of a Scanning Probe Tip. *Adv. Mater.,* 26: 2999.

121. Laracuente, A. R., et al. (2010) Reversible electron-induced conductance in polymer nanostructures. *J. Appl. Phys.,* 107: 103723.

122. Felts, J. R., Kjoller, K., Lo, M., Prater, C. B., and King, W. P. (2012) Nanometer-Scale Infrared Spectroscopy of Heterogeneous Polymer Nanostructures Fabricated by Tip-Based Nanofabrication. *ACS Nano,* 6: 8015.

123. Woodson, M., and Liu, J. (2006) Guided growth of nanoscale conducting polymer structures on surface-functionalized nanopatterns. *J. Am. Chem. Soc.,* 128: 3760.

124. Chiang, C.-H., and Wu, C.-G. (2010) Fabrication of sub-100 nm conducting polyaniline wire on a polymer substrate based on friction nanolithography. *Chem. Commun.,* 46: 2763.

125. Rakickas, T., Ericsson, E. M., Ružělė, Ž., Liedberg, B., and Valiokas, R. (2011) Functional Hydrogel Density Patterns Fabricated by Dip-Pen Nanolithography and Photografting. *Small,* 7: 2153.

126. Barbey, R., Lavanant, L., Paripovic, D., Schuwer, N., Sugnaux, C., Tugulu, S., and Klok, H. A. (2009) Polymer Brushes via Surface-Initiated Controlled Radical Polymerization: Synthesis, Characterization, Properties, and Applications. *Chem. Rev.,* 109: 5437.

127. Chen, T., Amin, I., and Jordan, R. (2012) Patterned polymer brushes. *Chem. Soc. Rev.,* 41: 3280.

128. Olivier, A., Meyer, F., Raquez, J.-M., Damman, P., and Dubois, P. (2012) Surface-initiated controlled polymerization as a convenient method for designing functional polymer brushes: From self-assembled monolayers to patterned surfaces. *Prog. Polym. Sci.,* 37: 157.

129. Kaholek, M., Lee, W. K., LaMattina, B., Caster, K. C., and Zauscher, S. (2004) Fabrication of stimulus-responsive nanopatterned polymer brushes by scanning-probe lithography. *Nano Lett.,* 4: 373.

130. Lee, W. K., Caster, K. C., Kim, J., and Zauscher, S. (2006)

Nanopatterned polymer brushes by combining AFM anodization lithography with ring-opening metathesis polymerization in the liquid and vapor phase. *Small,* 2: 848.

131. Barczewski, M., Walheim, S., Heiler, T., Blaszczyk, A., Mayor, M., and Schimmel, T. (2010) High Aspect Ratio Constructive Nanolithography with a Photo-Dimerizable Molecule. *Langmuir,* 26: 3623.

132. Ma, H. W., Hyun, J. H., Stiller, P., and Chilkoti, A. (2004) "Non-fouling" oligo(ethylene glycol)-functionalized polymer brushes synthesized by surface-initiated atom transfer radical polymerization. *Adv. Mater.,* 16: 338.

133. Liu, X. G., Guo, S. W., and Mirkin, C. A. (2003) Surface and site-specific ring-opening metathesis polymerization initiated by dip-pen nanolithography. *Angew. Chem. Int. Ed.,* 42: 4785.

134. Zapotoczny, S., Benetti, E. M., and Vancso, G. J. (2007) Preparation and characterization of macromolecular "hedge" brushes grafted from Au nanowires. *J. Mater. Chem.,* 17: 3293.

135. Zhou, X. Z., Chen, Y. H., Li, B., Lu, G., Boey, F. Y. C., Ma, J., and Zhang, H. (2008) Controlled growth of peptide nanoarrays on Si/SiOx substrates. *Small,* 4: 1324.

136. Liu, X., Li, Y., and Zheng, Z. (2010) Programming nanostructures of polymer brushes by dip-pen nanodisplacement lithography (DNL). *Nanoscale,* 2: 2614.

137. Zhou, X. C., Wang, X. L., Shen, Y. D., Xie, Z., and Zheng, Z. J. (2011) Fabrication of Arbitrary Three-Dimensional Polymer Structures by Rational Control of the Spacing between Nanobrushes. *Angew. Chem., Int. Ed.,* 50: 6506.

138. Zhou, X. C., Liu, Z. L., Xie, Z., Liu, X. Q., and Zheng, Z. J. (2012) High-Resolution, Large-Area, Serial Fabrication of 3D Polymer Brush Structures by Parallel Dip-Pen Nanodisplacement Lithography. *Small,* 8: 3568.

139. Lee, S. W., Sanedrin, R. G., Oh, B. K., and Mirkin, C. A. (2005) Nanostructured polyelectrolyte multilayer organic thin films generated via parallel dip-pen nanolithography. *Adv. Mater.,* 17: 2749.

140. Lee, G., Shin, Y. H., and Son, J. Y. (2009) Formation of Self-Assembled Polyelectrolyte Multilayer Nanodots by Scanning Probe Microscopy. *J. Am. Chem. Soc.,* 131: 1634.

141. Coffey, D. C., and Ginger, D. S. (2005) Patterning phase separation in polymer films with dip-pen nanolithography. *J. Am. Chem. Soc.,* 127: 4564.

142. Wei, J. H., Coffey, D. C., and Ginger, D. S. (2006) Nucleating pattern formation in spin-coated polymer blend films with nanoscale surface templates. *J. Phys. Chem. B,* 110: 24324.

143. Park, L. Y., Munro, A. M., and Ginger, D. S. (2008) Controlling Film Morphology in Conjugated Polymer: Fullerene Blends with Surface Patterning. *J. Am. Chem. Soc.,* 130: 15916.

144. Chiota, J., Shearer, J., Wei, M., Barry, C., and Mead, J. (2009) Multiscale Directed Assembly of Polymer Blends Using Chemically

Functionalized Nanoscale-Patterned Templates. *Small,* 5: 2788.

145. Germack, D. S., Checco, A., and Ocko, B. M. (2013) Directed Assembly of P3HT:PCBM Blend Films Using A Chemical Template with Sub-300 nm Features. *ACS Nano,* 7: 1990.

146. Xu, J., Park, S., Wang, S. L., Russell, T. P., Ocko, B. M., and Checco, A. (2010) Directed Self-Assembly of Block Copolymers on Two-Dimensional Chemical Patterns Fabricated by Electro-Oxidation Nano lithography. *Adv. Mater.,* 22: 2268.

147. Wegscheider, S., Kirsch, A., Mlynek, J., and Krausch, G. (1995) Scanning near-field optical lithography. *Thin Solid Films,* 264: 264.

148. Naber, A., Kock, H., and Fuchs, H. (1996) High-Resolution Lithography with Near-Field Optical Microscopy. *Scanning*, 18: 567.

149. Leggett, G. J., Sun, S. Q., and Chong, K. S. L. (2002) Nanoscale molecular patterns fabricated by using scanning near-field optical lithography. *J. Am. Chem. Soc.,* 124: 2414.

150. Leggett, G. J. (2006) Scanning near-field photolithography-surface photochemistry with nanoscale spatial resolution. *Chem. Soc. Rev.,* 35: 1150.

151. Leggett, G. J. (2012) Light-directed nanosynthesis: near-field optical approaches to integration of the top-down and bottom-up fabrication paradigms. *Nanoscale,* 4: 1840.

152. Kingsley, J. W., Ray, S. K., Adawi, A. M., Leggett, G. J., and Lidzey, D. G. (2008) Optical nanolithography using a scanning near-field probe with an integrated light source. *Appl. Phys. Lett.,* 93: 213103.

153. Riehn, R., Charas, A., Morgado, J., and Cacialli, F. (2003) Near-field optical lithography of a conjugated polymer. *Appl. Phys. Lett.,* 82: 526.

154. Credgington, D., Fenwick, O., Charas, A., Morgado, J., Suhling, K., and Cacialli, F. (2010) High-Resolution Scanning Near-Field Optical Lithography of Conjugated Polymers. *Adv. Funct. Mater.*, 20: 2842.

155. Reynolds, N. P., Tucker, J. D., Davison, P. A., Timney, J. A., Hunter, C. N., and Leggett, G. J. (2009) Site-Specific Immobilization and Micrometer and Nanometer Scale Photopatterning of Yellow Fluorescent Protein on Glass Surfaces. *J. Am. Chem. Soc.*, 131: 896.

156. Sun, S. Q., Thompson, D. G., Graham, D., and Leggett, G. J. (2011) DNA nanofabrication by scanning near-field photolithography of oligo (ethylene glycol) terminated SAMs: Controlled scan-rate dependent switching between head group oxidation and tail group degradation. *J. Mater. Chem.,* 21: 14173.

157. Sohn, L., and Willett, R. (1995) Fabrication of nanostructures using atomic-force-microscope -based lithography. *Appl. Phys. Lett.,* 67: 1552.

158. Kunze, U., and Klehn, B. (1999) Plowing on the sub-50 nm scale: Nanolithography using scanning force microscopy. *Adv. Mater.,* 11: 1473.

159. Heyde, M., Rademann, K., Cappella, B., Geuss, M., Sturm, H., Spangenberg, T., and Niehus, H. (2001) Dynamic plowing nanolithography on polymethylmethacrylate using an atomic force microscope. *Rev. Sci. Instrum.,* 72: 136.

References

160. Hirtz, M., Brinks, M. K., Miele, S., Studer, A., Fuchs, H., and Chi, L. (2009) Structured Polymer Brushes by AFM Lithography. *Small,* 5: 919.

161. Li, L., Hirtz, M., Wang, W., Du, C., Fuchs, H., and Chi, L. (2010) Patterning of Polymer Electrodes by Nanoscratching. *Adv. Mater.,* 22: 1374.

162. Shim, W., Brown, K. A., Zhou, X. Z., Rasin, B., Liao, X., Schmucker, A. L., and Mirkin, C. A. (2013) Plow and Ridge Nanofabrication. *Small,* 9: 3058.

163. Gan, T., Zhou, X., Ma, C., Liu, X., Xie, Z., Zhang, G., and Zheng, Z. (2013) Liquid-Mediated Three-Dimensional Scanning Probe Nanosculpting. *Small,* 9: 2851.

164. Pantazi, A., et al. (2008) Probe-based ultrahigh-density storage technology. *IBM J. Res. Dev.,* 52: 493.

165. Ma, Y., Wen, Y. Q., and Song, Y. L. (2011) Ultrahigh density data storage based on organic materials with SPM techniques. *J. Mater. Chem.,* 21: 3522.

166. Gotsmann, B., Duerig, U., Frommer, J., and Hawker, C. J. (2006) Exploiting chemical switching in a Diels-Alder polymer for nanoscale probe lithography and data storage. *Adv. Funct. Mater.,* 16: 1499.

167. Altebaeumer, T., Gotsmann, B., Pozidis, H., Knoll, A., and Duerig, U. (2008) Nanoscale shape-memory function in highly cross-linked polymers. *Nano Lett.,* 8: 4398.

168. Wiesmann, D., et al. (2009) Multi Tbit/in(2) Storage Densities with Thermomechanical Probes. *Nano Lett.,* 9: 3171.

169. Gotsmann, B., Knoll, A. W., Pratt, R., Frommer, J., Hedrick, J. L., and Duerig, U. (2010) Designing Polymers to Enable Nanoscale Thermomechanical Data Storage. *Adv. Funct. Mater.,* 20: 1276.

170. Wang, Y., Hong, X., Zeng, J., Liu, B., Guo, B., and Yan, H. (2009) AFM Tip Hammering Nanolithography. *Small,* 5: 477.

171. Jo, A., Joo, W., Jin, W. H., Nam, H., and Kim, J. K. (2009) Ultrahigh-density phase-change data storage without the use of heating. *Nat. Nanotech.,* 4: 727.

172. Szoszkiewicz, R., Okada, T., Jones, S. C., Li, T. D., King, W. P., Marder, S. R., and Riedo, E. (2007) High-speed, sub-15 nm feature size thermochemical nanolithography. *Nano Lett.,* 7: 1064.

173. Wang, D. B., et al. (2007) Local wettability modification by thermochemical nanolithography with write-read-overwrite capability. *Appl. Phys. Lett.,* 91.

174. Wang, D. B., et al. (2009) Thermochernical Nanolithography of Multifunctional Nanotemplates for Assembling Nano-objects. *Adv. Funct. Mater.,* 19: 3696.

175. Carroll, K. M., et al. (2013) Fabricating Nanoscale Chemical Gradients with ThermoChemical NanoLithography. *Langmuir,* 29: 8675.

176. Coulembier, O., et al. (2010) Probe-Based Nanolithography: Self-Amplified Depolymerization Media for Dry Lithography. *Macromolecules,*

43: 572.

177. Holzner, F., et al. (2011) Directed Placement of Gold Nanorods Using a Removable for Guided Assembly. *Nano Lett.,* 11: 3957.

178. Cheong, L. L., et al. (2013) Thermal Probe Maskless Lithography for 27.5 nm Half-Pitch Si Technology. *Nano Lett.,* 13: 4485.

179. Knoll, A. W., Pires, D., Coulembier, O., Dubois, P., Hedrick, J. L., Frommer, J., and Duerig, U. (2010) Probe-Based 3-D Nanolithography Using Self-Amplified Depolymerization Polymers. *Adv. Mater.,* 22: 3361.

180. Pires, D., et al. (2010) Nanoscale Three-Dimensional Patterning of Molecular Resists by Scanning Probes. *Science,* 328: 732.

181. Yan, Y. D., Hu, Z. J., Zhao, X. S., Sun, T., Dong, S., and Li, X. D. (2010) Top-Down Nanomechanical Machining of Three-Dimensional Nanostructures by Atomic Force Microscopy. *Small,* 6: 724.

182. Fenwick, O., Bozec, L., Credgington, D., Hammiche, A., Lazzerini, G. M., Silberberg, Y. R., and Cacialli, F. (2009) Thermochemical nanopatterning of organic semiconductors. *Nat. Nanotech.,* 4: 664.

183. Wang, D. B., et al. (2009) Direct writing and characterization of poly(p-phenylene vinylene) nanostructures. *Appl. Phys. Lett.,* 95: 233108.

184. Shaw, J. E., Stavrinou, P. N., and Anthopoulos, T. D. (2013) On-Demand Patterning of Nanostructured Pentacene Transistors by Scanning Thermal Lithography. *Adv. Mater.,* 25: 552.

185. Shaw, J. E., Stavrinou, P. N., and Anthopoulos, T. D. (2014) High-speed scanning thermal lithography for nanostructuring of electronic devices. *Nanoscale,* 6: 5813.

186. Liu, C. (2008) Parallel scanning probe arrays: their applications. *Mater. Today,* 11: 22.

187. Mirkin, C. A. (2007) The power of the pen: Development of massively parallel dip-pen nanolithography. *ACS Nano,* 1: 79.

188. Vettiger, P., et al. (2000) The "Millipede" - More than one thousand tips for future AFM data storage. *IBM J. Res. Dev.,* 44: 323.

189. Hong, S., and Mirkin, C. A. (2000) A nanoplotter with both parallel and serial writing capabilities. *Science,* 288: 1808.

190. Salaita, K., Lee, S. W., Wang, X. F., Huang, L., Dellinger, T. M., Liu, C., and Mirkin, C. A. (2005) Sub-100 nm, centimeter-scale, parallel dip-pen nanolithography. *Small,* 1: 940.

191. Kramer, M. A., Jaganathan, H., and Ivanisevic, A. (2010) Serial and Parallel Dip-Pen Nano lithography Using a Colloidal Probe Tip. *J. Am. Chem. Soc.,* 132: 4532.

192. Kramer, M. A., and Ivanisevic, A. (2012) Parallel Dip-Pen Nanolithography using Spore- and Colloid-Terminated Cantilevers. *Small,* 8: 3791.

193. Salaita, K., Wang, Y. H., Fragala, J., Vega, R. A., Liu, C., and Mirkin, C. A. (2006) Massively parallel dip-pen nanolithography with 55000-pen two-dimensional arrays. *Angew. Chem. Int. Ed.,* 45: 7220.

References

194. Lenhert, S., Sun, P., Wang, Y., Fuchs, H., and Mirkin, C. A. (2007) Massively Parallel Dip Pen Nanolithography of Heterogeneous Supported Phospholipid Multilayer Patterns. *Small,* 3: 71.

195. Lenhert, S., et al. (2010) Lipid multilayer gratings. *Nat. Nanotech.,* 5: 275.

196. Jang, J.-W., Park, B., and Nettikadan, S. (2014) Generation of plasmonic Au nanostructures in the visible wavelength using two-dimensional parallel dip-pen nanolithography. *Nanoscale,* 6: 7912.

197. Bullen, D., Chung, S. W., Wang, X. F., Zou, J., Mirkin, C. A., and Liu, C. (2004) Parallel dip-pen nanolithography with arrays of individually addressable cantilevers. *Appl. Phys. Lett.,* 84: 789.

198. Wang, X. F., and Liu, C. (2005) Multifunctional probe array for nano patterning and imaging. *Nano Lett.,* 5: 1867.

199. Bullen, D., and Liu, C. (2006) Electrostatically actuated dip pen nanolithography probe arrays. *Sensor Actuat. A-Phys.,* 125: 504.

200. Haq, E. u., et al. (2010) Parallel Scanning Near-Field Photolithography: The Snomipede. *Nano Lett.,* 10: 4375.

201. Carroll, K. M., et al. (2014) Parallelization of thermochemical nanolithography. *Nanoscale,* 6: 1299.

202. Giam, L. R., and Mirkin, C. A. (2011) Cantilever-Free Scanning Probe Molecular Printing. *Angew. Chem. Int. Ed.,* 50: 7482.

203. Eichelsdoerfer, D. J., et al. (2013) Large-area molecular patterning with polymer pen lithography. *Nat. Protoc.,* 8: 2548.

204. Liao, X., Braunschweig, A. B., Zheng, Z. J., and Mirkin, C. A. (2010) Force- and Time-Dependent Feature Size and Shape Control in Molecular Printing via Polymer-Pen Lithography. *Small,* 6: 1082.

205. Giam, L. R., Massich, M. D., Hao, L., Wong, L. S., Mader, C. C., and Mirkin, C. A. (2012) Scanning probe-enabled nanocombinatorics define the relationship between fibronectin feature size and stem cell fate. *PNAS,* 109: 4377.

206. Liao, X., Braunschweig, A. B., and Mirkin, C. A. (2010) "Force-Feedback" Leveling of Massively Parallel Arrays in Polymer Pen Lithography. *Nano Lett.,* 10: 1335.

207. Zheng, Z. J., Daniel, W. L., Giam, L. R., Huo, F. W., Senesi, A. J., Zheng, G. F., and Mirkin, C. A. (2009) Multiplexed Protein Arrays Enabled by Polymer Pen Lithography: Addressing the Inking Challenge. *Angew. Chem. Int. Ed.,* 48: 7626.

208. Brinkmann, F., Hirtz, M., Greiner, A. M., Weschenfelder, M., Waterkotte, B., Bastmeyer, M., and Fuchs, H. (2013) Interdigitated Multicolored Bioink Micropatterns by Multiplexed Polymer Pen Lithography. *Small,* 9: 3266.

209. Arrabito, G., et al. (2014) Configurable Low-Cost Plotter Device for Fabrication of Multi-Color Sub-Cellular Scale Microarrays. *Small,* 10: 2870.

210. Han, Y., and Liu, C. (2011) Pneumatically actuated active polymer pen lithography. *Sensor Actuat. A-Phys.,* 167: 433.

References

211.Brown, K. A., et al. (2013) A cantilever-free approach to dot-matrix nanoprinting. *PNAS,* 110: 12921.

212. Wong, L. S., Karthikeyan, C. V., Eichelsdoerfer, D. J., Micklefield, J., and Mirkin, C. A. (2012) A methodology for preparing nanostructured biomolecular interfaces with high enzymatic activity. *Nanoscale,* 4: 659.

213. Bian, S. D., He, J. J., Schesing, K. B., and Braunschweig, A. B. (2012) Polymer Pen Lithography (PPL)-Induced Site-Specific Click Chemistry for the Formation of Functional Glycan Arrays. *Small,* 8: 2000.

214. Bian, S. D., Schesing, K. B., and Braunschweig, A. B. (2012) Matrix-assisted polymer pen lithography induced Staudinger Ligation. *Chem. Commun.,* 48: 4995.

215. Bian, S. D., Scott, A. M., Cao, Y., Liang, Y., Osuna, S., Houk, K. N., and Braunschweig, A. B. (2013) Covalently Patterned Graphene Surfaces by a Force-Accelerated Diels-Alder Reaction. *J. Am. Chem. Soc.,* 135: 9240.

216. Han, X., Bian, S., Liang, Y., Houk, K. N., and Braunschweig, A. B. (2014) Reactions in Elastomeric Nanoreactors Reveal the Role of Force on the Kinetics of the Huisgen Reaction on Surfaces. *J. Am. Chem. Soc.* 136: 10553.

217. Shim, W., Braunschweig, A. B., Liao, X., Chai, J., Lim, J. K., Zheng, G., and Mirkin, C. A. (2011) Hard-tip, soft-spring lithography. *Nature,* 469: 516.

218. Shim, W., Brown, K. A., Zhou, X. Z., Rasin, B., Liao, X., and Mirkin, C. A. (2012) Multifunctional cantilever-free scanning probe arrays coated with multilayer graphene. *PNAS,* 109: 18312.

219. Liao, X., Brown, K. A., Schmucker, A. L., Liu, G. L., He, S., Shim, W., and Mirkin, C. A. (2013) Desktop nanofabrication with massively multiplexed beam pen lithography. *Nat. Commun.,* 4: 2103.

220. Xing, C. F., Liu, L. B., Tang, H. W., Feng, X. L., Yang, Q., Wang, S., and Bazan, G. C. (2011) Design Guidelines For Conjugated Polymers With Light-Activated Anticancer Activity. *Adv. Funct. Mater.,* 21: 4058.

221. Jung, H., Dalal, C. K., Kuntz, S., Shah, R., and Collier, C. P. (2004) Surfactant activated dip-pen nanolithography. *Nano Lett.,* 4: 2171.

222. Azzaroni, O., Moya, S. E., Brown, A. A., Zheng, Z., Donath, E., and Huck, W. T. S. (2006) Polyelectrolyte brushes as ink nanoreservoirs for microcontact printing of ionic species with poly(dimethyl siloxane) stamps. *Adv. Funct. Mater.,* 16: 1037.

223. Azzaroni, O., Zheng, Z. J., Yang, Z. Q., and Huck, W. T. S. (2006) Polyelectrolyte brushes as efficient ultrathin platforms for site-selective copper electroless deposition. *Langmuir,* 22: 6730.

224. Zhou, X. C., Liu, X. Q., Xie, Z., and Zheng, Z. J. (2011) 3D-patterned polymer brush surfaces. *Nanoscale,* 3: 4929.

225. Lin, X., He, Q., and Li, J. (2012) Complex polymer brush gradients based on nanolithography and surface-initiated polymerization. *Chem. Soc. Rev.,* 41: 3584.

226. He, Q., Kueller, A., Schilp, S., Leisten, F., Kolb, H.-A., Grunze, M., and Li, J. (2007) Fabrication of Controlled Thermosensitive Polymer Nanopatterns

with One-Pot Polymerization Through Chemical Lithography. *Small,* 3: 1860.

227. Schilp, S., Ballav, N., and Zharnikov, M. (2008) Fabrication of a full-coverage polymer nanobrush on an electron-beam-activated template. *Angew. Chem. Int. Ed.,* 47: 6786.

228. Steenackers, M., Jordan, R., Kuller, A., and Grunze, M. (2009) Engineered Polymer Brushes by Carbon Templating. *Adv. Mater.,* 21: 2921.

229. Steenackers, M., Kueller, A., Ballav, N., Zharnikov, M., Grunze, M., and Jordan, R. (2007) Morphology control of structured polymer brushes. *Small,* 3: 1764.

230. Poelma, J. E., Fors, B. P., Meyers, G. F., Kramer, J. W., and Hawker, C. J. (2013) Fabrication of Complex Three-Dimensional Polymer Brush Nanostructures through Light-Mediated Living Radical Polymerization. *Angew. Chem. Int. Ed.,* 52: 6844.

231. Fors, B. P., et al. (2013) Fabrication of Unique Chemical Patterns and Concentration Gradients with Visible Light. *J. Am. Chem. Soc.,* 135: 14106.

232. Benetti, E. M., Acikgoz, C., Sui, X., Vratzov, B., Hempenius, M. A., Huskens, J., and Vancso, G. J. (2011) Nanostructured Polymer Brushes by UV-Assisted Imprint Lithography and Surface-Initiated Polymerization for Biological Functions. *Adv. Funct. Mater.,* 21: 2088.

233. Moran, I. W., Ell, J. R., and Carter, K. R. (2011) Functionally Decoupled Soft Lithography for Patterning Polymer Brushes. *Small,* 7: 2669.

234. Li, Y. F., et al. (2012) Polymer brush nanopatterns with controllable features for protein pattern applications. *J. Mater. Chem.,* 22: 25116.

235. Wang, M., Comrie, J. E., Bai, Y. P., He, X. M., Guo, S. Y., and Huck, W. T. S. (2009) Formation of Hierarchically Structured Thin Films. *Adv. Funct. Mater.,* 19: 2236.

236. Chen, T., Zhong, J. M., Chang, D. P., Carcia, A., and Zauscher, S. (2009) Fabrication of Micropatterned Stimulus-Responsive Polymer-Brush 'Anemone'. *Adv. Mater.,* 21: 1825.

237. Chen, T., Jordan, R., and Zauscher, S. (2011) Dynamic Microcontact Printing for Patterning Polymer-Brush Microstructures. *Small,* 7: 2148.

238. Gao, T. T., Wang, X. L., Yu, B., Wei, Q. B., Xia, Y. Q., and Zhou, F. (2013) Noncovalent Microcontact Printing for Grafting Patterned Polymer Brushes on Graphene Films. *Langmuir,* 29: 1054.

239. Shah, R. R., Merreceyes, D., Husemann, M., Rees, I., Abbott, N. L., Hawker, C. J., and Hedrick, J. L. (2000) Using atom transfer radical polymerization to amplify monolayers of initiators patterned by microcontact printing into polymer brushes for pattern transfer. *Macromolecules,* 33: 597.

240. Jiang, H., and Xu, F. J. (2013) Biomolecule-functionalized polymer brushes. *Chem. Soc. Rev.,* 42: 3394.

241. Jang, J.-W., Collins, J. M., and Nettikadan, S. (2013) User-Friendly Universal and Durable Subcellular-Scaled Template for Protein Binding: Application to Single-Cell Patterning. *Adv. Funct. Mater.,* 23: 5840.

242. Yea, K. H., Lee, S., Choo, J., Oh, C. H., and Lee, S. (2006) Fast and

sensitive analysis of DNA hybridization in a PDMS micro-fluidic channel using fluorescence resonance energy transfer. *Chem. Commun.,*1509.

243. Bian, S., et al. (2014) Beam pen lithography as a new tool for spatially controlled photochemistry, and its utilization in the synthesis of multivalent glycan arrays. *Chem. Sci.,* 5: 2023.

244. Hu, H., Yeom, J., Mensing, G., Chen, Y. F., Shannon, M. A., and King, W. P. (2012) Nano-fabrication with a flexible array of nano-apertures. *Nanotechnology,* 23: 175303.

245. Chen, Y.-Z., Wu, C.-Y., and Lee, Y.-C. (2014) Beam pen lithography based on arrayed polydimethylsiloxane (PDMS) micro-pyramids spin-coated with carbon black photo-resist. *J. Micromech. Microeng.,* 24: 045007.

246. Wu, C.-Y., and Lee, Y.-C. (2014) Apertureless beam pen lithography based on fully metal-coated polyurethane-acrylate (PUA) pyramidal microstructure array. *Opt. Express,* 22: 10593.

247. Eichelsdoerfer, D. J., Brown, K. A., Wang, M. X., and Mirkin, C. A. (2013) Role of Absorbed Solvent in Polymer Pen Lithography. *J. Phys. Chem. B,* 117: 16363.

248. Hong, J. M., Ozkeskin, F. M., and Zou, J. (2008) A micromachined elastomeric tip array for contact printing with variable dot size and density. *J. Micromech. Microeng.,* 18: 015003.

249. Qin, D., Xia, Y. N., Black, A. J., and Whitesides, G. M. (1998) Photolithography with transparent reflective photomasks. *J. Vac. Sci. Technol. B,* 16: 98.

250. Qin, D., Xia, Y. N., and Whitesides, G. M. (1997) Elastomeric light valves. *Adv. Mater.,* 9: 407.

251. Wendeln, C., Rinnen, S., Schulz, C., Arlinghaus, H. F., and Ravoo, B. J. (2010) Photochemical Microcontact Printing by Thiol-Ene and Thiol-Yne Click Chemistry. *Langmuir,* 26: 15966.

252. Jackman, R. J., Duffy, D. C., Ostuni, E., Willmore, N. D., and Whitesides, G. M. (1998) Fabricating large arrays of microwells with arbitrary dimensions and filling them using discontinuous dewetting. *Anal. Chem.,* 70: 2280.

253. Cheng, Y.-T., and Cheng, C.-M. (2004) Scaling, dimensional analysis, and indentation measurements. *Mater. Sci. Eng. R-Rep.,* 44: 91.

254. Schmid, H., and Michel, B. (2000) Siloxane polymers for high-resolution, high-accuracy soft lithography. *Macromolecules,* 33: 3042.

255. Odom, T. W., Love, J. C., Wolfe, D. B., Paul, K. E., and Whitesides, G. M. (2002) Improved pattern transfer in soft lithography using composite stamps. *Langmuir,* 18: 5314.